Measurements and modelling of reflection and transmission from smooth and rough surfaces at 62 GHz
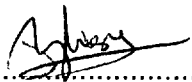
Jean-Pierre Pugliese

A submission presented in partial fulfilment of the requirements of the University of Glamorgan/Prifysgol Morgannwg for the degree of Master of Philosophy

University of Glamorgan

November 1999

Declaration

This to certify that, except where specific reference is made, the work described in this thesis is the result of the candidate. Neither this thesis, nor any part of it, has been presented, or is currently submitted, in candidature for any degree at any University.

Signed: ....

Jean-Pierre Pugliese

Acknowledgements

Abstract

Mobile communication often suffers from interference caused mostly by multipath propagation mode. This latter is associated with signal delays and signal level fades due to reflections, scatters, transmissions and diffractions by obstacles surrounding the environment. Indoor and outdoor building layout often influence the signal. In order to understand and mitigate the signal decay, knowing the internal properties as well as the surface characteristics of building materials could improve the deterioration of the signal.

This thesis presents a study on the characterisation of the internal properties and the surface of various building materials at 62.4 GHz. Models have been applied to help in the interpretation of the reflectivity, scatter and transmissivity measurements performed on different materials.

Reflectivity and transmissivity measurements at 62.4 GHz have been made inside the anechoic chamber on eight different building materials, and results are expressed as functions of observation and incident angles. It has been shown that the well-known Fresnel coefficients fail to predict reflectivity and transmissivity values when the thickness of the material is not too large compared to a wavelength. A model based on multiple successive internal reflection has been developed and successfully used to explain experimental results. The effects of this reflection mechanism on changing the statistics of an indoor mobile radio channel has also been demonstrated using ray-tracing. The model has also been utilised to provide estimates of the dielectric parameters of building materials.

Measurements of the scattered field from rough surfaces have also been presented. Purpose made rough surfaces have been constructed by impregnating concrete slabs by 10, 20 and 40 mm angular stones. Two building façades one made from big stone and the other being pebble-dash have also been measured. The parameters describing the surface roughness have been measured and used to calculate, using the Kirchhoff approximation, the scatter level. It has been shown that the

scattered field is of, a diffuse and random nature. Predictions have been found to under-estimate the scatter level.

Further measurements have been made to quantify the amount of depolarisation by rough surfaces and examine any possible correlation with the values of the parameters describing the rough surface. It has not been possible to relate depolarisation and roughness.

In order to understand the reflection off rough and smooth surfaces, co and cross-polarisation measurements were made inside the anechoic chamber on surfaces made from smooth and rough parts. The semi-specular level has been found to vary with the percentage of rough surface area within the intersection area made from the transmit and receive antennas. This level has been successfully predicted by combining experimental results made on all smooth and all rough slabs by the percentage of their area within the total cross-intersection area.

List of Symbols

Δ_{field}	Far field distance (m)
Γ_0	General reflection coefficient at an angle of incidence of 0°
Γ_g	General reflection coefficient
Γ_{rs}	Scatter coefficient
I_0	Modified Bessel function of the first kind and zeroth order
T_g	General transmission coefficient
T_s	General transmission coefficient from 2 identical materials spaced by an air gap
α	Attenuation proper to the material (Np/m)
ε_0	Permittivity of the free space (F/m)
ε_r	Relative permittivity of the medium
ε_{rb}	Permittivity best estimate
ε_{rm}	Error margin on the permittivity best estimate
η_1	Refractive index free space
η_2	Refractive index medium
λ	Wavelength (m)
μ_0	Permeability of the free space (H/m)
μ_r	Relative permeability of the medium
γ^2	Propagation constant
θ_b	3dB beamwidth of an antenna (rad)
θ_i	Angle of incidence(rad)
θ_t	Refraction angle (rad)
ρ	Reflected experimental data points
ρ'	Reflected theoretical data points

ρ_H	Reflection coefficient for horizontal polarization
ρ_s	Scattering factor
ρ_v	Reflection coefficient for vertical polarization
σ	Conductivity (s/m)
σ_h	Standard deviation function of rough surfaces (m)
σ_{rb}	Conductivity best estimate
σ_{rm}	Error margin on the conductivity best estimate
τ	Transmitted experimental data points
τ'	Transmitted theoretical data points
τ_v	Transmission coefficient for vertical polarization
τ_H	Transmission coefficient for horizontal polarization
ω	Pulsation (rad/s
ξ	Random rough surface
A	Cross illumination area made between the transmitter and receiver (m^2)
CW	Carrier Wave
D	Biggest physical aperture of a horn antenna (m)
DAB	Data Acquisition Board
GO	Geometrical optics
HH	Horizontal-Horizontal polarization
HV	Horizontal-Vertical polarisation
IF	Intermediate Frequency, in Hertz
K	K-parameter of the Rician distribution
L	Length of a random rough surface (m)
LNA	Low Noise Amplifier
LOS	Line-Of-Sight
LSF	Least Square Fit
Pr	Reflected power (W)
P_{Rician}	Rician distribution function
P_s	Scattered power (W)
Pt	Transmitted power (W)
RMS	Root Mean Square
T_d	Correlation distance of a rough surface (m)

VH	Vertical-Horizontal polarisation
VV	Vertical-Vertical polarization
Z_0	Impedance of free space (Ω)
Z_1	Intrinsic impedance of medium (Ω)
b	Mean received power
d	Path length difference between two out-going rays (m)
d_1	Distance from the antenna to the material (m)
f	Frequency (Hz)
i	Integer
k	Propagation constant (rad/m)
k_0	Propagation in free space (rad/m)
l'	Thickness of the material (m)
l_1	Length of the material (m)
l_2	Width of the material (m)
l_t	Illuminated horizontal axis (m)
r_i	Difference between theoretical and experimental points
r_s	Line-of-sigtht peak value
s	Path length inside a slab (m)

Table of Contents

List of Figures

List of Tables

40 mm stones and smooth stripe

1 Introduction

1.1 Background

Radio-communication technology has developed immensely since the proposal of equations to describe electromagnetic waves by James Clerk Maxwell that opened the new era of wireless communications. However, the invention of wireless telegraphy by Gugliemo Marconi during the 1890s was really the beginning of communication between users not connected by wires. Nowadays wireless communication is well used and constitutes one of the major ways of exchanging data.

Demand for digital cellular communications continues to grow at a phenomenal rate. Certain networks are already showing signs of capacity saturation in major urban centres, even with relatively modest subscriber penetration rates. It has become evident in numerous networks around the world that as the coverage and capacity are increased, the subscriber occupancy of the available traffic channels also increases. This is brought about to instil greater confidence in the subscriber of the ability to originate and maintain a call due to the improved performance of the system. Clearly, as this trend continues, major capacity increases will be required to meet future demand. Therefore, millimetre waves have been proposed to liberate the frequency spectrum below 1.8 GHz and to establish also a higher data rate communications [Steele, 1985].

The frequency band around 60 GHz is especially advantageous because of the specific attenuation characteristics of about 15 dB/km due to atmospheric oxygen absorption. This specific characteristic has a potential to reduce interference among different systems operating at the same frequency band, and does not cause significant transmission loss in short distance propagation systems. In this manner those frequencies can be re-used in indoor and outdoor environments without introducing significant interference in the received signal. The successful utilisation of this frequency band both indoors and outdoors requires the full understanding of the types of propagation mechanisms which occur. There is much research work undertaken to characterise the line-of-sight (LOS) indoor and outdoor millimetre wave channels [Tarek, 1988], [Cole, 1988] and [Violette, 1983]. For both scenarios the received signal consists

of a LOS, when there is no direct obstruction between the two antennas, and contributions of interferences caused by the abundant presence of obstacles such as vegetation, buildings, materials, etc. This multipath propagation on millimetre radiowave links is associated with signal delays and signal level fades which adversely influence the system performance [Parsons, 1992]. The knowledge of how a signal will be modified according to the obstacles encountered could enable to reduce the multipath propagation and thus enhance the quality of the information. Research studies have been undertaken on characterising the effects of specific obstacles, such as vegetation [Stephens, 1998] and buildings [Ding, July 1994], upon the electromagnetic waves. Such results may be introduced in a general radio mobile environment model, e.g. Hata [Hata, August 1980]. This kind of model is suitable for signals propagating in large environments called macro-cells.

At millimetre wave frequencies, models have to accurately describe the received signal in indoors. In such environments it is necessary to accurately describe the type of surfaces of the enclosed environment. Most of time some idealised mathematical representations of the characteristics of the channel are made on the basis of the geometrical optics (GO) by using ray-tracing theories [Kermoal, April 1998] [Allen, Sept. 1990] and [Kloch, March 1998]. Models based on ray-tracing algorithms were applied for both indoor and outdoor scenarios where the propagation depends primarily on reflection, scattering and transmission from obstacles. Diffraction at millimetre waves has been found to be negligible [Hammoudeh, April 1995].

1.2   The Mobile Radio Channel

Propagation media are very complex and cannot be represented accurately by any model. The propagation mechanisms are often quantified by simplifying the obstacles. This is done by assuming that the electrical properties of reflecting surfaces are known at frequencies around 60 GHz, the obstacle dimensions are infinitely large, and that their surfaces are smooth.

Fresnel coefficients are therefore often used to calculate the transmission and reflection from surfaces of defined dimensions such as building materials with known dielectric parameters [Balanis, 1989] for different frequencies. At the frequency band around 60 GHz little work has so far been devoted to the dielectric parameters of building materials. Reflection and transmission mechanisms by materials of defined dimensions

and specific surface irregularities have to be investigated in order to establish whether they follow results obtained using the Fresnel coefficients.

1.3 Objectives of Research

In order to understand some of the problems mentioned in the previous section, reflection and transmission mechanisms of different building materials with various sizes and surface irregularities have been investigated at 62.4 GHz.

Reflectivity and transmissivity measurements have been performed inside an anechoic chamber on eight different smooth building materials using vertical and horizontal polarisations. A model based on multiple successive internal reflection inside the material has been developed to characterise the transmission and reflection mechanisms when smooth materials have defined dimensions. Comparisons between measured and predicted results have been employed to establish the electrical properties of various materials. Values obtained in this thesis are compared with those reported in the literature. The model developed here has been introduced in a ray-tracing tool in order to compare the indoor radio channel characteristics with those obtained using the Fresnel coefficients.

Scatter from seven rough surfaces have then been explored and measured using co and cross-polarisations and results are presented as a function of incident and observation angles. Measurements have taken place inside an anechoic chamber and outside on two different sites. The surface irregularities of each material have been measured and the parameters defining the roughness of a surface have been obtained. These parameters have been inserted in a model based on the Kirchhoff approximation in order to obtain a theoretical representation of the scatter coefficient as a function of incident and observation angles. Materials containing smooth and rough surfaces have also been measured and results are compared with those obtained from theoretical predictions. The dependence of the signal level on the parameters describing the rough surface has been investigated using vertical and horizontal polarisations. Effects of depolarisation have also been explored for vertical-horizontal (VH) and horizontal-vertical (HV) polarisations.

1.4   Outline of the Thesis

Chapter 2 summarizes the relevant work for this research project, which includes published material in books and articles on a range of subjects. The importance in characterising the reflection, transmission and scatter mechanisms of rough and smooth materials is highlighted. It is seen that those types of mechanisms are strictly governed by the electrical properties and surface irregularities of materials and often calculated by theoretical approximations. A need to characterise the materials by their dielectric parameters and surface roughness at 62.4 GHz is therefore demonstrated together with their effects on the radio channel characteristics. Different methods for estimating the electrical properties of smooth materials are discussed and results are compared.

The surface roughness of materials can be modelled by different theoretical representations accounting for more or less accurate details of the surface. Those different theoretical approaches are explored and the differences between them are highlighted.

The effects of the reflection, transmission and scatter mechanisms on indoor or outdoor radio channel are described and illustrated.

Chapter 3 describes in details the 62.4 GHz measuring system hardware employed together with various experimental geometries. Different set-ups have been devised and developed to undertake indoor and outdoor measurements on a range of building materials and building façades. Measurements inside the anechoic chamber involved bi-static measurements providing simultaneously the reflection and transmission coefficients of smooth and rough building materials as a function of incident and observation angles. As the outdoor measurements are concerned, two building façades have been measured. For this purpose a mobile radio set-up has been devised and developed.

Chapter 4 presents experimental and theoretical reflection and transmission coefficients as a function of incident angles for various building materials. Measurements are compared with theoretical predictions obtained from a model yielding general reflection and transmission coefficients as a function of the thickness of the material, and the angle of incidence. Dielectric parameters are estimated for vertical and horizontal polarisations by comparing experimental and theoretical results using the root mean square (RMS) error and the Bootstrap techniques. Results obtained are then compared with those reported in the literature.

The general coefficients have been introduced in a ray-tracing tool in order to compare results with those obtained when the Fresnel coefficients are accounted for. In order to help in interpreting the results, the Rice distribution and the power exponential factors have been calculated.

In Chapter 5, the study is concentrated on materials with different surface irregularities. Scatter measurements have been performed on five different purpose made concrete slabs and two building façades. The scatter coefficients have been measured as a function of incident and observation angles for co and cross-polarisations. The parameters defining the roughness of each surface have been calculated and introduced in a theoretical model based on Kirchhoff approximation. The signal level dependence on the roughness of the materials has been investigated and compared with various models. The amount of depolarisation in terms of the material roughness has also been investigated.

Chapter 6 summarizes the work undertaken and outlines the overall conclusion on the results presented in this thesis. A list of further work relevant to the research conducted here is also given.

2 Wireless Mobile Radio Channel

2.1 Introduction

The development of efficient wireless transmission systems has been the object of numerous studies [Molkdar, Feb. 1991] [Andersen, Jan. 1995] for a long time and is still nowadays in progress in order to offer greater and quicker access to all kinds of information services at any place and time [COST 231]. A profound knowledge of the radio propagation phenomena or the radio channel characteristics is a prerequisite to achieving an optimum system design. The illustration in Figure 2-1 shows the multipath mechanisms that take place when signals travel from the source to the receiver via different propagation paths. The received signal is then not only made of the direct line-of-sight (LOS) but also of other contributions due to reflection, refraction, scatter and/or diffraction. The arrival of various components from different directions with different time delays causes amplitude variations in the received signal envelope. The troughs of signal variations are known as fading. The term fast and slow fading are used to express the short and the much longer-term variations respectively [Parsons, 1992]. Multipath causes deep fading and pulse spreading of the signal and hence intersymbol interference is likely in digital radio systems. Fades with a depth less than 20 dB are frequent, with deeper fades in excess of 40 dB being less frequent but not uncommon [Duffy, 1988]. Two major cases of multipath exist: "static" and "dynamic" ones. When a communication takes place between two fixed antennas, static multipath occurs while dynamic multipath is present when a relative motion between the terminals exists. In the case of dynamic multipath the received signal experiences an apparent shift in its frequency defined as the Doppler effect [Howard, Jan. 1990]. The concepts of dynamic multipath and frequency shift are related to each other [Bello, Dec. 1963].

Fading can usually be described by two statistical distributions: Rician and Rayleigh [Linnartz, 1993]. Rician fading is exhibited when a LOS is predominant. Rayleigh fading is a special case of Rician when there is no direct ray which will reach the receiver. This is typical in an urban environment.
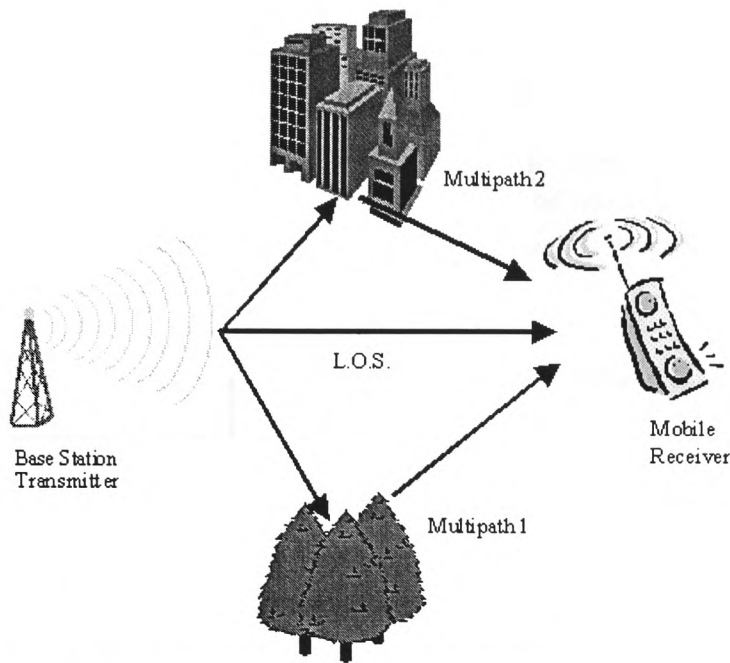
Figure 2-1: Multipath mechanisms in a radio link

2.2 Mobile Radio Propagation Characteristics

Although multipath mechanism seriously degrades the quality of the information, diversity and equalisation techniques may be used to reduce the effects of multipath propagation. Mathematical representations of the radio channel have been of interest removing the large cost and time consumptions linked to radio propagation measurements. Models for millimetre wave cellular mobile radio systems are well documented in the literature [Kermoal, April 1998] [McKnown, Nov. 1991] [Dersch, Sept. 1994] [Hammoudeh, March 1999] [Bailey, 1994] [Amitay, Nov. 1992] [Seidel, 1994] and [Sánchez, March 1996]. Propagation models can be classified into two major classes: statistical models and site-specific (deterministic) propagation models. The statistical models are based on the statistics in the environment, describing the distribution of the scatterers [Turin, 1956] [Rappaport, May 1990]. Although statistical models are useful for understanding the propagation of radio waves in specific environments, exhaustive measurements are required to obtain the data to determine the appropriate parameters necessary to model a particular environment.

In contrast, the site-specific propagation models are based on the use of geometrical optics (GO) to characterise the propagation medium. Unlike the statistical models, those ones do not need data from exhaustive campaigns of measurements, however a detailed definition of the environment is required to obtain accurate prediction

results. Ray-tracing techniques have been developed to model the mobile radio channel characteristics by considering that the electromagnetic waves behave in a ray-like fashion. Two types of ray-tracing are reported in the literature: the image method [Kermoal, April 1998] [Hammoudeh, Aug. 1995] and the ray launching method [McKnown, Nov. 1991]. Both methods may be combined where the multiple-image and ray launching concepts were used to provide a three-dimensional model [Tan, Aug. 1995].

The ray launching method called "brute force" [Suzuki, Aug. 1997] considers all the possible angles of departure and arrival at the transmitter and receiver that a ray can experience. For this algorithm to be successfully used for complex environments it requires large number of rays and reception tests. By increasing the angular separation between neighbouring rays some propagation paths can be missed, whereas reducing the separation has the consequences that some paths will be represented by more than one ray.

Unlike the ray launching method, the image method considers the transmitter or the receiver to be mirrored by the different surfaces present in the environment. The single-reflection propagation path can then be obtained by connecting for example the source point obtained by mirroring the transmitter, reflection point and receiver point. A double-reflection propagation path is obtained and is illustrated in Figure 2-2. The order of reflection calculated determines the accuracy of the ray-tracing tool to represent the mobile radio channel. The image theory is very useful to model environments with low complexity. When images of the transmitter are calculated the method, is referred as forward ray-tracing whereas the method is called backward ray-tracing method when images are calculated from the receiver. Figure 2-2 shows the forward ray-tracing method accounting for second reflections in a two-dimensional environment.

The order of reflection taking into account by the ray-tracing methods provides more or less accurate approximation of the mobile radio channel. It has been demonstrated that good approximations to model indoor and outdoor environments can be achieved by calculation of the eighth [Dersch, Sept. 1994] and second [Hammoudeh, March 1999] order reflections respectively.
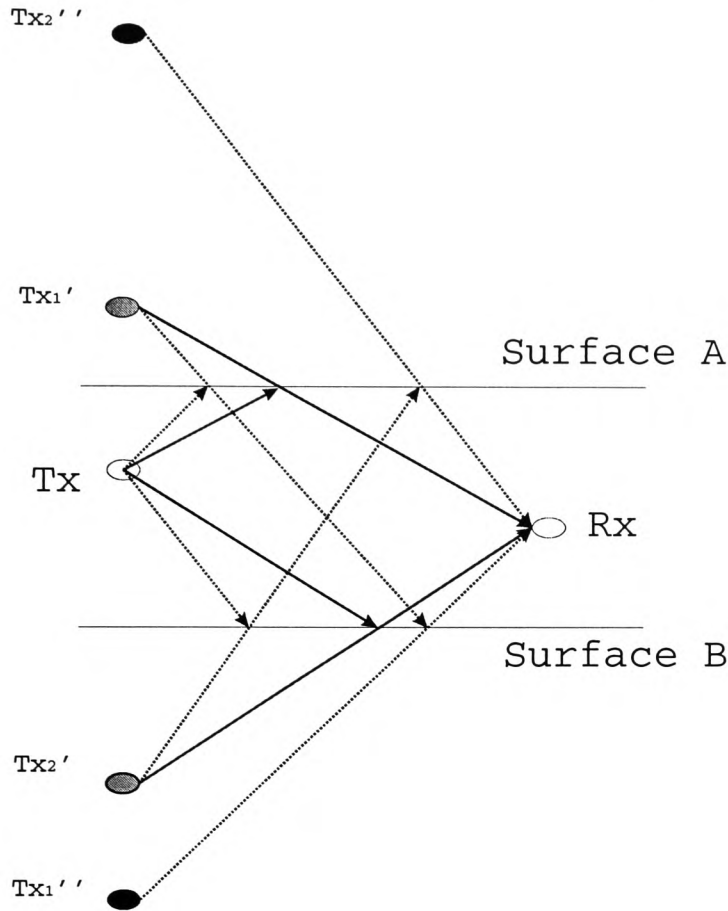
Figure 2-2: Image theory principle, where the transmitter Tx is mirrored by the surfaces A and B giving source images Tx_1' and Tx_2' respectively. The images Tx_1" and Tx_2" of the source images have also been calculated

The accuracy of a model can not only be evaluated by the order of reflection taken into account. The detailed description of the environment in terms of the geometry and the electrical properties of the different surfaces, and the accurate quantification of different phenomena such as scatter, reflection, transmission and refraction is necessary for accurate representation of the mobile radio channel. Numerous ray-tracing algorithms incorporate simplified form expressions to quantify the different phenomena occurring and simplify the description of the environment. Contributions of diffraction in an indoor environment have been investigated at a frequency of 60 GHz [Hammoudeh, April 1995] and were found to be negligible.

Fresnel coefficients are used most of the time to quantify reflection and transmission by materials with a given thickness where the values of the dielectric parameters are obtained from the literature [Balanis, 1989] [Kraus, 1991]. However Fresnel coefficients have been established to quantify reflection and transmission by

infinite smooth media. In indoors it is then important to model the reflection and transmission mechanisms when smooth reflecting surfaces are of definite dimensions [Heavens, 1955]. In outdoors however, reflections from building surfaces with irregularities are the main contributors to the received signal strength and hence show the need to model such mechanisms.

2.3 Estimation of the Electrical Properties of Materials using Various Measuring Set-Ups

An important issue in microwave and millimetre wave theory concerns the determination of the values of the dielectric parameters called also the complex permittivity of a material. The knowledge of the dielectric parameters of a material has major impacts in diverse areas such as radar imaging, biological tissue analysis and radar absorbing material (RAM). Radar imaging of terrain (desert and forest) [Evans, Oct. 1999] has been used to provide detailed information about vegetation for assessing changes in land cover, biomass and forest regrowth [Pope, 1994]. Surface-penetrating radar has been used to search for non-conductive buried objects [Daniels, Aug. 1996]. Biological tissue analysis is also of interest since detection of specific substance can be achieved [Steel, Nov. 1986], and a mathematical representation of the human head for instance could bring solutions for the mobile communications. A perfect understanding of the dielectric parameters provide to develop materials non-detectable by radar [Smith, Sept. 1992].

Different techniques have been devised and developed in order to calculate the complex permittivity of different materials. The selection of those techniques depends on the feasibility to accurately place and cut in very specific dimensions, and the type of the specimen. Measurements of materials using waveguides are often used for small solid specimens cut in extremely accurate dimension sizes [Harrington, 1961] [Steel, 1987] [Alison, 1991] [Richards, 1991] [Wu, April 1992]. Liquids and gazes are measured using special infrared devices [Birch, June 1994]. Both microwave techniques such as the waveguide method and infrared techniques such as the Fourier transform spectroscopy fail in precise dielectric measurement in the millimetre wave band around 60 GHz.

Another most popular method determines the dielectric parameters of a specimen by measuring its reflection and transmission coefficients in a free space [Knott, 1993] [Varadan, Aug. 1991] [Ghodaonkar, June 1989] [Correia, Sept. 1994]. This method has established that reflection and transmission mechanisms by materials with a given

thickness do not follow the Fresnel coefficients. The development of models accounting for the thickness of the material has provided to determine the dielectric parameters of a majority of materials, vegetation, etc. The reflection and transmission mechanisms for materials with a given thickness are detailed in Chapter 4. This model assumes that multiple successive reflections inside the material occur. The model has also been extended for a dielectric multilayer [Heavens, 1955]. [Sato, Dec. 1997] compared reflection measurements performed inside a building at 57.5 GHz with those predicted by the multilayer model.

Reflections measurements from a soda-lime glass (1x1 m^2) have been reported by [Manabe, July 1992] using a vector network analyser (VNA). Measurements of amplitude and phase, for frequencies ranging from 57 to 58 GHz, have provided the estimation of the soda-lime glass complex permittivity by comparing measured results with predictions obtained using the model accounting for the material thickness.

Transmission and reflection measurements of concrete plates (600x500x30 mm^3) have also been reported by [Sato, Jan. 1996] at 57.5 GHz. Measurements were done for different periods of time, when the concrete was still fresh, and after 14 days. Reflectivity and transmissivity measurements were taken for 16 different incident angles ranging from 6 to 75° using a VNA. It was established that the attenuation is depending of the concrete curing time. Different dielectric parameters were obtained at different times due to the water contents still present in the concrete. It was also demonstrated that, although the concrete is actually a mixture of several materials, the concrete can equivalently be treated as a homogeneous dielectric plate.

Reflection and transmission measurements using only carrier wave (CW) have also been investigated and developed, reducing in that way the cost of the instrumentation devices. Reflectivity measurements of 8 different materials have been performed every 1° for a range of incident angle ranging from 0 to 50° at 93.788 GHz [Shimabukuro, July 1984]. The dielectric parameters were inferred from those measurements using two techniques, the RMS error and the Bootstrap [Efron, 1982]. [Correia, Sept. 1994] demonstrated that different estimates of the dielectric parameters can be obtained from the same material using either reflectivity or transmissivity measurement. The calculation of the complex permittivity was different from the same material when different polarisations were used. Reflection and transmission measurements were performed at 60.2 GHz using 4 different incident angles [Correia, Jan. 1994], and dielectric parameters of 10 different materials have been given. From those values estimates of the isolation for each material have been calculated [Correia, Sept. 1995]. Transmissivity measurements on 2 identical materials, where the air gap between them was varied, were performed at 59.5 GHz by [Lähteenmäki, Aug. 1996].

Measured results done over 10 different air gap distances were compared with those predicted by (2-1). The dielectric parameters obtained were slightly different from those calculated by [Correia, Sept. 1994]. This model has been based on the geometrical optics (GO) where the electromagnetic waves are assumed to behave in ray-like fashion. The transmission coefficient, T_s, in this case is given by [Lähteenmäki, Aug. 1996]: -

$$T_s = \frac{\left(1 - \Gamma_0^2\right)e^{\left(jk_sd_s - \alpha d_s\right)}}{1 - \Gamma_0^2 e^{\left(j2k_sd_s - 2\alpha d_s\right)}}$$

(2-1)

Where Γ_0 is the Fresnel reflection coefficient; k_s is the wavenumber in the wall material, d_s is the thickness of one slab and α is the attenuation constant.

2.4 Theoretical Treatment of Random Rough Surfaces

The scattering of electromagnetic waves from, and their transmission through, randomly rough surfaces has been an active research area for many years, and remains one today because of the technological uses of such scattering as for example the interpretation of measurements from land and sea surfaces [Beckmann, 1987] [Bass, 1979] [Medwin, 1997].

Different theories have been applied under certain assumptions for analyzing the effect of the surface roughness. Some of them are based on deterministic description [Beckmann, 1987] [Ogilvy, 1991] [Hviid, Jan. 1995], and some of them on a statistical description of the surface roughness [Bahar, Sept. 1991] [Landron, March 1996]. However, it is not yet clear when the various approximations hold or which theory would be better to explain the results of some experiments. No theory covers all degrees of the surface variation, as far as the author is concerned. Most theories [Rice, 1951] [Ashdown, 1994] separate solutions for the coherent (present in the specular direction only) and the non-coherent powers.

The surface characteristics can either be expressed deterministically by measuring the surface protuberance or statistically considering that the scattered power is Lambertian which means that the intensity of the scattered power in any direction can be described by a simple cosine relation.

The Rayleigh criterion [Beckmann, 1987] is often used to determine whether, at a given frequency, the surface is considered to be smooth or rough. A surface is then said to be smooth when: -

$$h < \frac{\lambda}{8\cos(\theta_i)} \qquad (2\text{-}2)$$

Where: λ is the wavelength (m), θ_i is the incident angle (rad) and h is the height of the surface irregularities (m).

Different theories propose solutions to model the scattered field by rough surfaces. The major theories applied at present are briefly summarised here: -

- **The Perturbation method** – The solution here is the sum of rays propagated from the transmitter to the receiver, scattered in one way or another by the surface [Rice, 1951]. The accuracy of this method totally fails for deterministic surfaces with large slopes made by taking the plane tangent of a point on the surface. [Kloch, March 1998] applied both the coherent and non-coherent perturbation theories on results obtained from an outdoor environment at 900 and 1800 MHz where the surface irregularities are much larger than the wavelength. It was concluded that the most significant scattering contributions occur close to the mobile station since for large distances the surface acts like a smooth one.

- **The Integral Equation Method (IEM)** – This method avoids the finding of separate solutions for the coherent (present in the specular direction only) and non-coherent power [Hviid, January 1995]. Although good estimations of the scattered power can be obtained, inaccuracies are introduced since approximations must be made in order to get a reasonable computation time. This method is applicable when the surface irregularities are larger than the wavelength. [Kloch, March 1998] used this method on a rural environment at 900 and 1800 MHz in order to determine the relationship between the statistical parameters describing the variation of the surface and the propagation exponent, but no obvious dependency could be shown.

- **The Radiosity** – This method, used by computer scientists in order to generate photorealistic images, calculates the scattered signal from each surfaces that are ideal diffuse (or Lambertian) reflectors [Ashdown, 1994]. This method is successfully used for heights of surface irregularities larger than the wavelength. [Kloch, July 1997] shows the contributions of the roughness in an indoor corridor at 900 and

1800 MHz. The corridor (30 m long x 10 m wide and 3 m high) has a number of irregularities due to windows, doors and protuberances in the side-walls. Results of the mean delay and RMS delay spread obtained by Radiosity were in good agreement with values obtained from the impulse response measurements.

• **The Kirchhoff approximation** – In this method the total field and its normal derivative are approximated by the values that would exist on a plane tangent to each point of the surface [Beckmann, 1987]. A general solution is given for a surface normally distributed. However other distributions can be treated quite analogically. Unlike the other theories, the solution is obtained by a relatively straightforward calculation and will break down totally if the correlation distance is smaller than the wavelength. The Kirchhoff approximation has also been simplified to express the scatter coefficient in the specular direction from a rough surface. This simplified expression is a function of the reflection coefficient, the standard deviation of the surface irregularities and the angle of incidence. This simplified expression has been deduced from slightly rough surfaces.

When the surface is not explicitly defined, its roughness may then represented by two functions which are the standard deviation and the correlation distance of the surface. The correlation distance describes whether the peaks and troughs of the surface roughness are crowded together or whether they are far apart. [Beckmann, 1987] proposes a simplified expression, as given in (2-3), of the Kirchhoff approximation applicable in the specular region in order to characterise the scatter coefficient from a rough surface. This expression assumes a Gaussian distributed surface roughness with standard deviation σ_h.

$$\Gamma_{rs} = |\Gamma_g| \cdot e^{-\frac{g}{2}} \qquad (2\text{-}3)$$

With: $\qquad g = \left(\frac{4 \cdot \pi \cdot \sigma_h \cdot \cos\theta_i}{\lambda}\right)^2 \qquad (2\text{-}4)$

Where: Γ_g is a general expression of the Fresnel reflection coefficient (equation (4-15) Chapter 4), σ_h is the standard deviation of the surface protuberance (m), θ_i is the angle of incidence (rad) and λ is the wavelength (m).

This simplified scatter coefficient is valid for values of $g<1$.

[Langen, Sept. 1994] uses the expression (2-3) to characterise the reflection and transmission behaviour of 10 rough building materials at 60.2 GHz. It was concluded that the results obtained using the expression (2-3) were in a reasonable good agreement with those measured using a bi-static measuring system. [Landron, March 1996] measured the reflection of two rough exterior building walls at 1.9 and 4 GHz. Measured results obtained at 4 different incident angles were compared with solutions calculated from the expression (2-3) altered by inserting the modified Bessel function of the zeroth order. This modified solution has been found to adequately predict the measured results.

[Hammoudeh, March 1999] incorporated the expression (2-3) in a three-dimensional ray-tracing algorithm to characterise the outdoor radio propagation urban street 230 m long at 62.4 GHz. Predicted results gave good qualitative agreements with the measurements. However it has been demonstrated that, when a scanning of the receive antenna was done in the azimuthal plane, measured and predicted reflected levels differ significantly.

3 *Experimental Hardware and Geometry*

3.1 *Introduction*

Indoor and outdoor measurements were made in order to characterise the reflection and transmission coefficients as functions of the angle of incidence. Measurements have been performed inside an anechoic chamber on smooth building materials and purpose made rough surfaces using vertical-vertical (VV) and horizontal-horizontal (HH) polarisations. Furthermore, measurements have been made on rough building façades in order to examine the scatter coefficient. The building materials tested are those mostly widely used for interior and exterior constructions. The materials used are described and discussed in this chapter.

3.2 *The 62.4GHz System*

The transmitter, Figure 3-1, is composed of a cavity stabilised 62.4 GHz Gunn oscillator delivering a power of 57.2 mW. In order to protect the source from any back reflections, an isolator is inserted between the antenna and the oscillator. At the receiver, Figure 3-2, the received signal is converted down, via a phase locked oscillator operating at 61.8 GHz, to an intermediate frequency (IF) of 600 MHz. The signal is then amplified by a low noise amplifier (LNA), with a gain of 32 dB. Then a bandpass filter with a 3 dB bandwidth of 5 MHz, which brings down the noise floor to −74 dBm, is inserted. The output of the filter is then connected to a logarithmic amplifier to measure the signal strength. The signal is then sampled by a data acquisition board (DAB). Other channels of the DAB can be used to record terminal locations with the help of markers. Those points of reference are used for outdoor measurements.
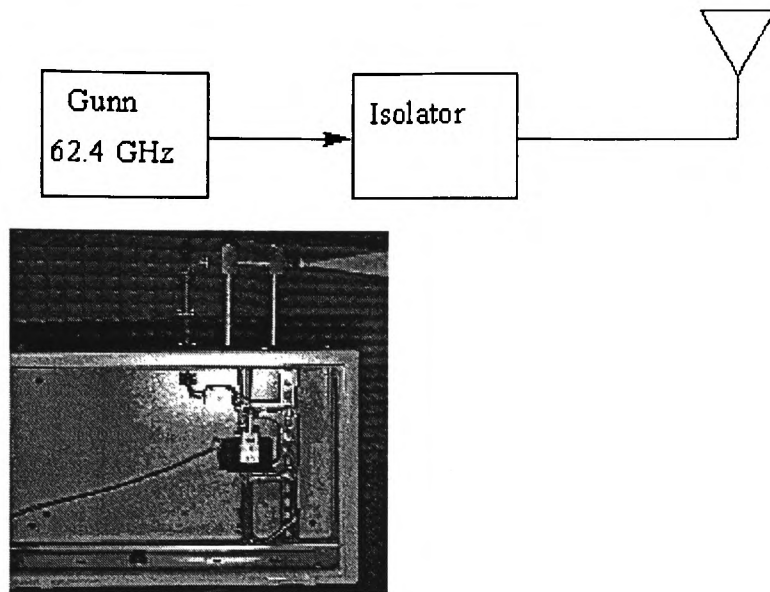
Figure 3-1: Block diagram and photograph of the 62.4 GHz transmitter
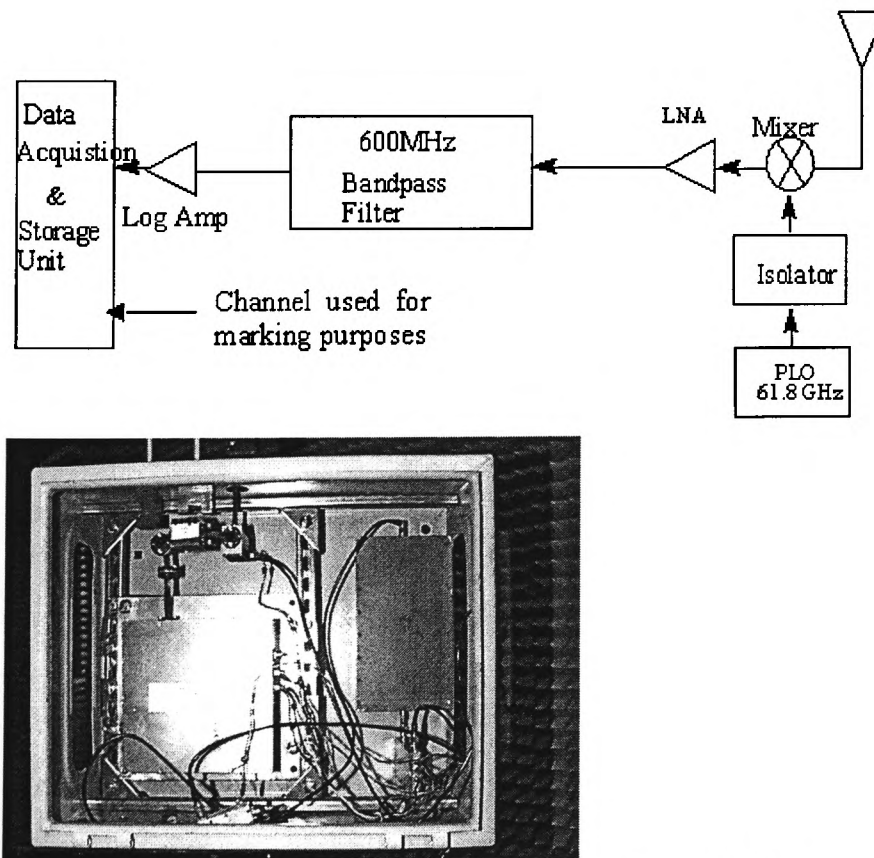
Figure 3-2: Block diagram and photograph of the 62.4 GHz receiver

3.3 Antennas

Three different antennas were employed for the different set-up involved in the measurements. The 25 dBi horn antenna was used for the indoor measurements whereas the 10 dBi and the restricted beamwidth omnidirectional antenna were used for outdoor measurements. The choice of the antennas was made in such a way that the surface of the material was illuminated at all the times.

3.3.1 The 25 dBi Horn

The 25 dBi horn antenna has a 3 dB beamwidth of 9.4° and 9° in elevation and horizontal planes respectively. Furthermore its physical aperture dimensions are 33 mm high and 40 mm long. The far field distance of this antenna, Δ_{field}, is: -

$$\Delta_{field} = \frac{2 \cdot D^2}{\lambda} \tag{3-1}$$

Where: D is the biggest physical aperture of a horn antenna, in meters;

λ is the wavelength, in meters.
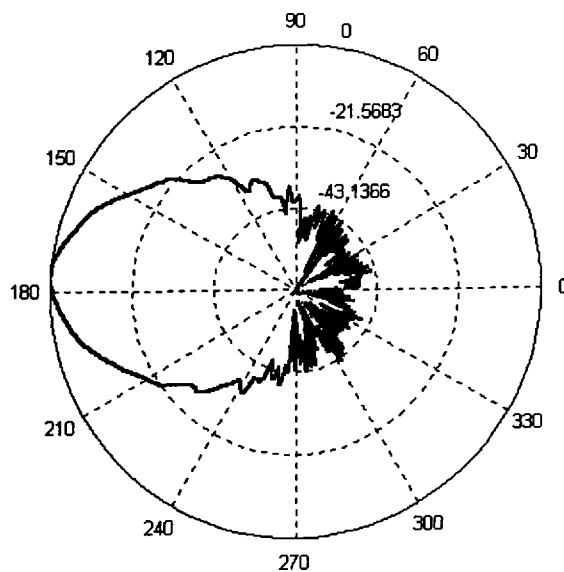
Figure 3-3: E-plane radiation pattern measured for the 25 dBi horn antenna

Thus the far field distance at 62.4 GHz is found to be 66.56 cm. The radiation pattern of this antenna was measured in the anechoic chamber for both E and H planes as shown in Figure 3-3 and Figure 3-4 respectively.
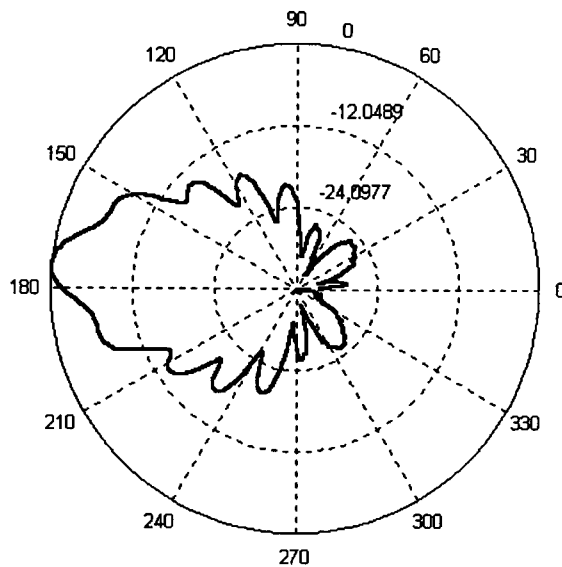
Figure 3-4: H-plane radiation pattern measured for the 25 dBi horn antenna

3.3.2   The 10 dBi Horn
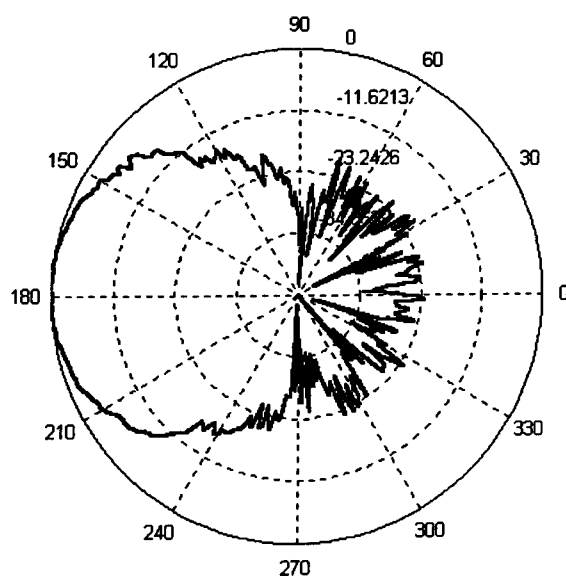
Figure 3-5: E-plane radiation pattern measured for the 10 dBi horn

The 10 dBi horn antenna is a much smaller one with its physical aperture 4 mm high and 8 mm wide. As regard its illumination, the 3 dB beamwidths are 69° and 55° for E and H planes respectively as shown in Figure 3-5 and Figure 3-6. At 62.4 GHz the far field distance is 26.6 cm.
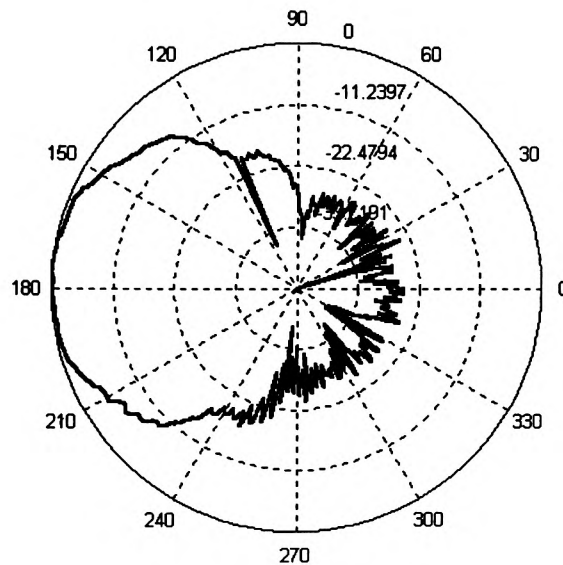
Figure 3-6: H-plane radiation pattern measured for the 10 dBi horn

3.3.3 The Omnidirectional Antenna
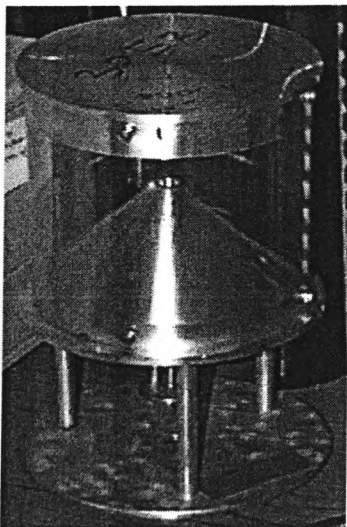
Figure 3-7: Omnidirectional antenna used at 62.4 GHz

The omnidirectional antenna, Figure 3-7, consists of two plates supported by a plastic sheet around their circumference. The bottom plate, which is connected to a circular waveguide, has the shape of a cone, while the top one is a parabola. This antenna has 9 dBi gain and an elevation 3 dB beamwidth of 6.5°, as shown in Figure 3-8.
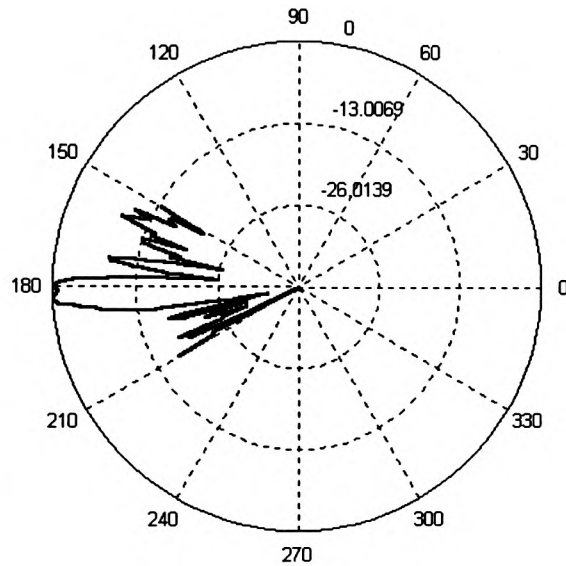
Figure 3-8: Vertical plane radiation pattern measured for the omnidirectional antenna

3.3.4 The Restricted Omnidirectional Antenna Coverage
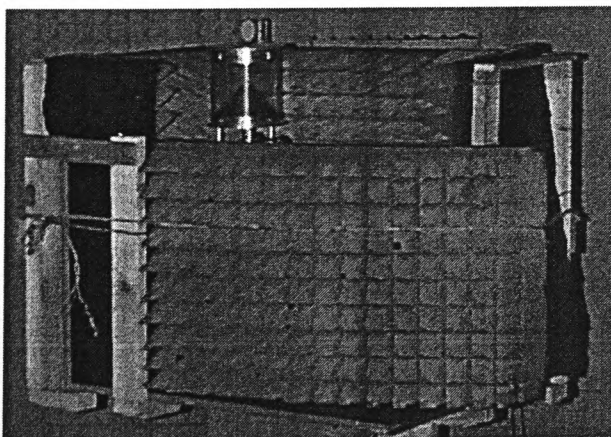
Figure 3-9: Omnidirectional antenna shielded with absorbing materials

When the omnidirectional antenna was used for outdoor measurements, it needed to have a restricted azimuthal coverage as will be described later in this chapter. Absorbing materials were used to shield the antenna so that the 90° aperture could be achieved as can be seen in Figure 3-9.The radiation pattern in the azimuth plane was measured inside the anechoic chamber and the result is given in Figure 3-10.
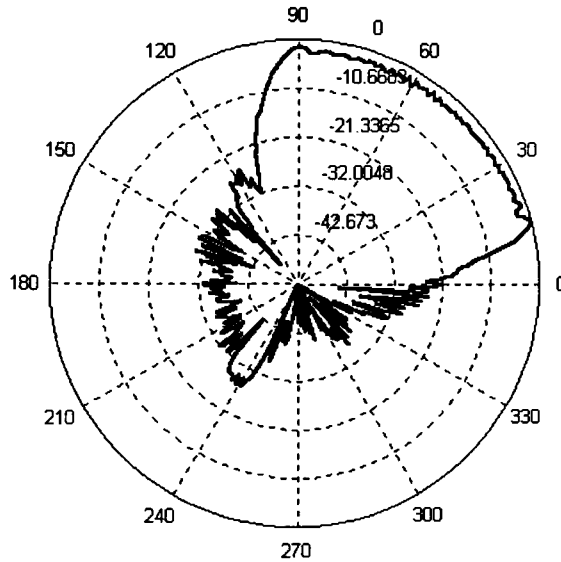
Figure 3-10: Radiation pattern of the restricted omnidirectional antenna in the azimuthal plane

3.4 Indoor Set-Up

A diagram of the measurement set-up used inside the anechoic chamber to simultaneously measure reflectivity and transmissivity is shown in Figure 3-11. The material under test was fixed upright on top of a high precision computer controlled rotary table. Underneath this rotary table, and centered on the same axis, a second rotary table was used to move an L-shape bracket along the perimeter of a circle by the assistance of 4 wheels. The receiver was mounted on the bracket at a distance of 87 cm away from the material. The transmitter was set at the same height as the receiver, and was placed 2 m away from the material, and thus outside the movement of the receiver. Two identical 25 dBi horn antennas were used at the transmitter and receiver.

a)

b)
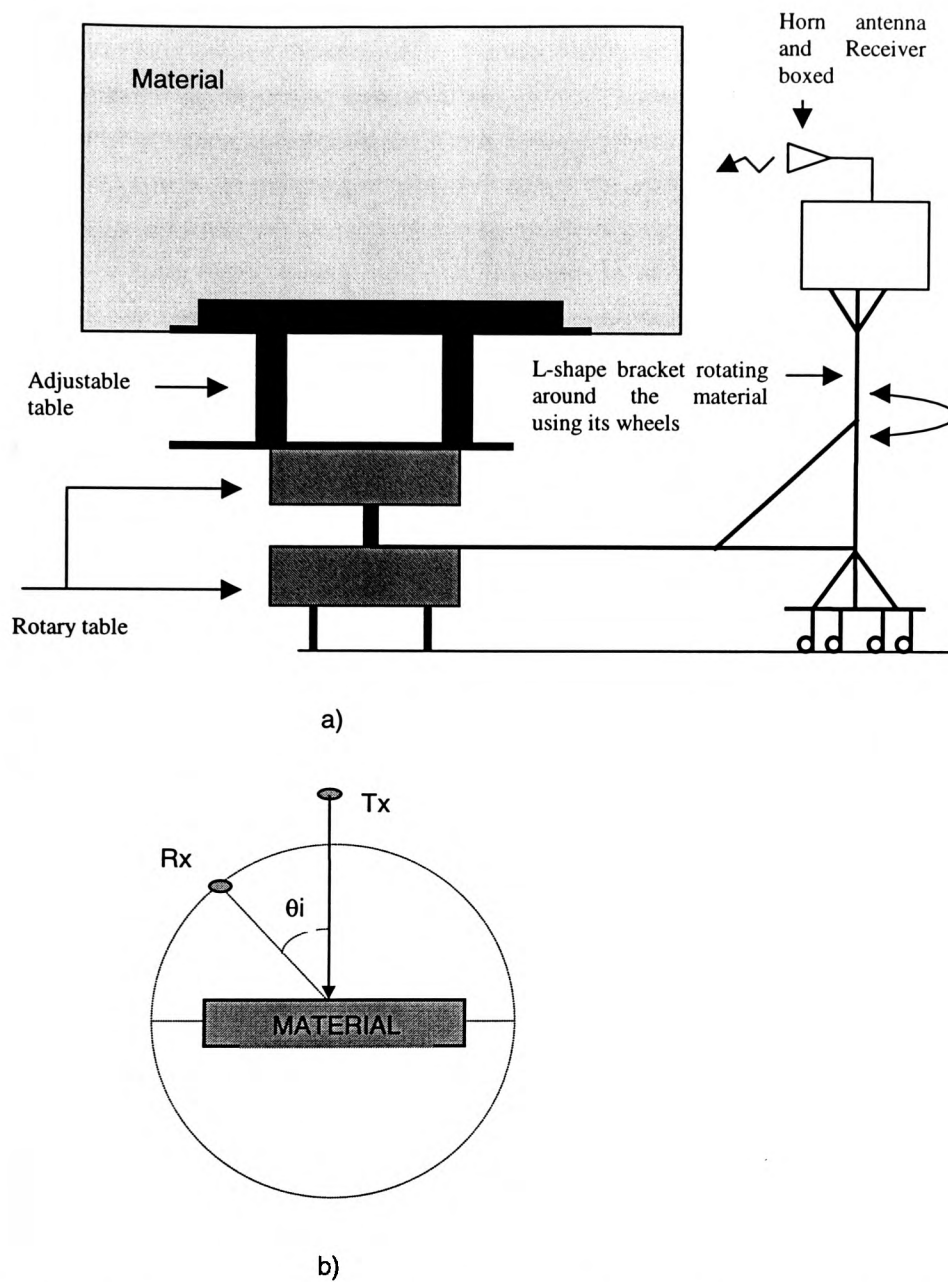
Figure 3-11: Bi-static measuring system used inside the anechoic chamber to record the reflectivity and transmissivity of building materials, a) side view b) top view

A computer located outside the chamber was used to control both rotary tables. The angle of incidence with respect to the normal to the material was varied by turning the material in 4° increments. This increment was chosen in order to record a large population of reflectivity and transmissivity points as functions of the angle of incidence. Measurements were made for angles of incidence between 10° to 70°. The angles of incidence were limited to this range in order to exclude any other contributions which

might come from either the two antennas mutual coupling or diffraction. The receiver was made to rotate around the material in discrete increment of 1°. At each receiver position, the received signal power was obtained from its sampled values taken at a rate of 1,000,000 samples per second and these were averaged over 12,500 samples. The set-up used to measure the transmissivity and reflectivity simultaneously is depicted in Figure 3-11. The antennas and the material were positioned so that measurements were made in the far field region of the antennas. Photographs of the set-up inside the anechoic chamber for smooth and rough building materials are given in Figure 3-12 and 3-13.
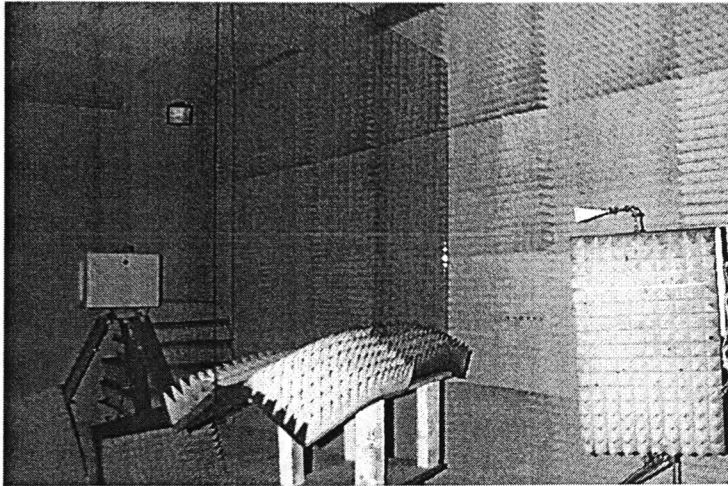
Figure 3-12: Reflectivity and transmissivity measurements of a glass inside the anechoic chamber
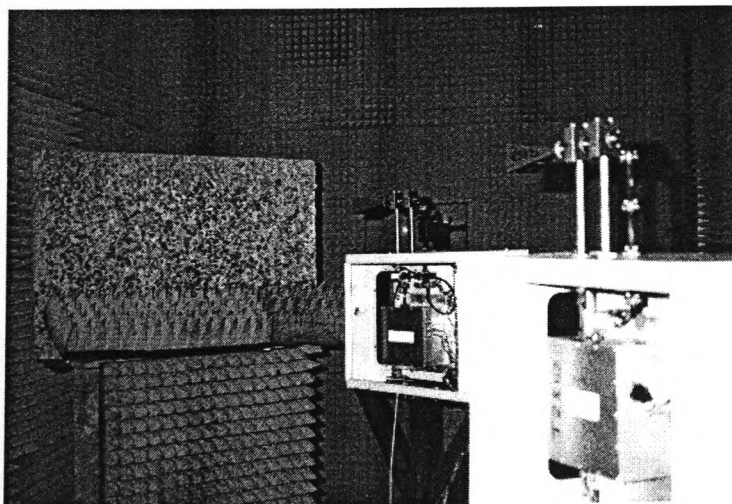
Figure 3-13: Reflectivity and transmissivity measurements of a rough building material inside the anechoic chamber

3.5 Receiver and Transmitter Illuminations on the Materials

Using the set-up described, the illumination area of the receiver and the transmitter changes with the angle of incidence. Indeed as the angle of incidence increases the illumination area increases as well. In Figure 3-14 it can be seen that when the material rotates thus making a defined incident angle, the illumination caused by the antenna will expand according to the horizontal plane. When θ_i is 0° the illumination area on the material is circular. At other angles the area makes an ellipse.

As the material rotates, the transmitter and receiver illumination areas increase. The range of incident angles is calculated in such a way that the intersection of the illumination areas made between the transmitter and the receiver stays within the material's dimension. For this reason the illumination area made by the transmitter and the receiver is calculated here.
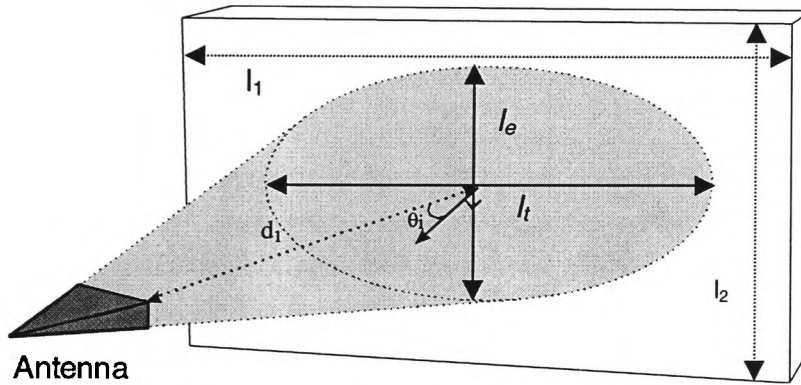
Figure 3-14: Illuminated area formed by an antenna on a material

For the above geometry and at a given angle of incidence the distance l_t, major axis of the ellipse, must be smaller than l_1. l_t may be expressed as:

$$l_t = \left(\frac{1}{\cos(\theta_i + \theta_b)} + \frac{1}{\cos(\theta_i - \theta_b)} \right) \cdot d_1 \cdot \sin(\theta_b) \qquad (3\text{-}3)$$

Where: d_1 is the distance from the antenna to the material, in metres;

$2 \cdot \theta_b$ is the beamwidth of the antenna, in radians;

θ_i is the incident angle, in radians;

l_t is the illuminated horizontal axis given in metres.

In the same manner the distance l_e, minor axis of the ellipse, must be smaller than l_2. l_e may be expressed as:

$$l_e = \frac{2 \cdot d_1 \cdot \sin\theta_b}{\cos\theta_b}$$

(3-4)

Where: d_1 is the distance from the antenna to the material, in metres;

$2 \cdot \theta_b$ is the beamwidth of the antenna in radians.

By calculating the illumination area for each terminal, it has been noticed that no correction in the received power is necessary as each experiment is normalised by a free space measurement done by replacing the material by a metal sheet.

3.6 Outdoor Set-Up

Outdoor measurements have also been made on two building facades. For this purpose a 12 m long track bench was designed to have at its centre a rail track [Kermoal, April 1998]. Along one side of the track bench a number of markers were spaced. On top of this track a trolley holding the transmitter along with a battery and an inverter was moved along the rail with the help of a pilot wood bar placed inside the rail track and attached underneath the trolley. The trolley was moved by the traction of a motor, placed at one end of the track bench, which wound a rope attached to the trolley and going through a pulley at the other end of the bench. The set-up is represented in Figure 3-15.
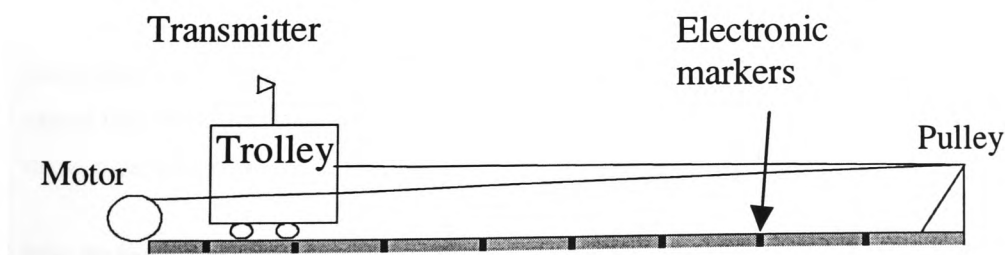
Figure 3-15: Outdoor measuring system used to move the transmitter along the bench in order to illuminate the surface studied
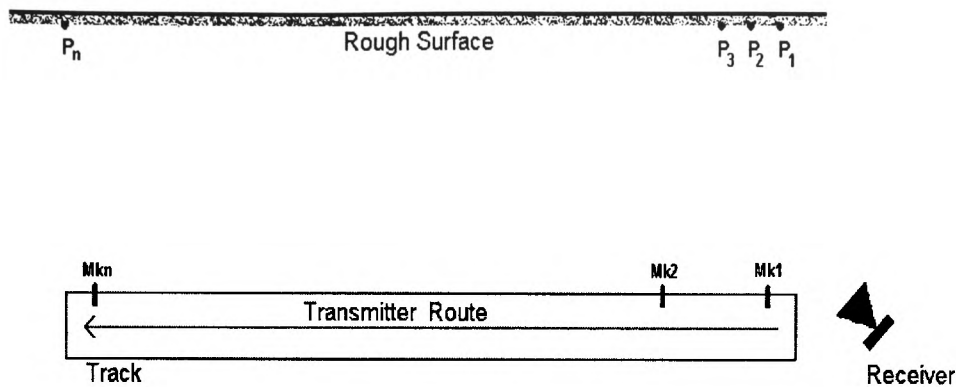
Figure 3-16: Overall outdoor set-up used to measure the scatter from a surface as a function of the incident angle

The motor was pulling the trolley at a constant speed of 1 m/s. The receiver was mounted on a tripod and located at the same distance from the wall as the transmit antenna. The receive antenna was a 25 dBi horn, whereas the transmitter had the restricted beamwidth omnidirectional antenna illuminating the façade. Both antennas were set at the same height.

The receive antenna was located 2 m away from the wall and was tilted in the horizontal plane to make an angle of incidence with respect to the normal of the wall. For each angle of incidence the transmitter positioned at the same distance from the wall was moved along the bench track in order to measure the scatter coefficient. To measure accurately the angles of incidence a laser pointer was placed on top of the receiver and pointing in the same direction as the receive antenna. This was done in order to determine the point at which the antenna is pointing at the wall. Furthermore the angle of incidence as well as the observation angle at each position along the track were calculated from the geometry of the set-up which was obtained using electronic distance markers. This was facilitated by the assistance of colleagues in the School of Built Environment (University of Glamorgan). The set-up is shown in Figure 3-16.

For each tilt of the receive antenna, the angle of incidence was measured. Then the transmitter was moved along the bench so that the receiver could collect the reflected signal from the wall. The reflected signal was normalised with respect to the free space using a calibrated curve measured inside the anechoic chamber.

The received data was stored in a laptop via a data acquisition board. This latter was providing the information of the received signal as well as the position of the transmitter on the bench. In this manner a software called Testpoint^{TM} enabled to visualise the stored

data after each measurement so that any erroneous results could be corrected by repeating the measurement. The sampling rate of the data acquisition was 500 Hz.

3.6.1 Pontypridd Car Park

A stone wall in Pontypridd, in Figure 3-17, was used to perform scatter measurements. The track bench used was 12 m long and both the transmit and receive antennas were located 2 m away from the wall. Both terminals height was set at 1.87 m. The track bench was leveled and fixed such that the transmit antenna is parallel to the wall.
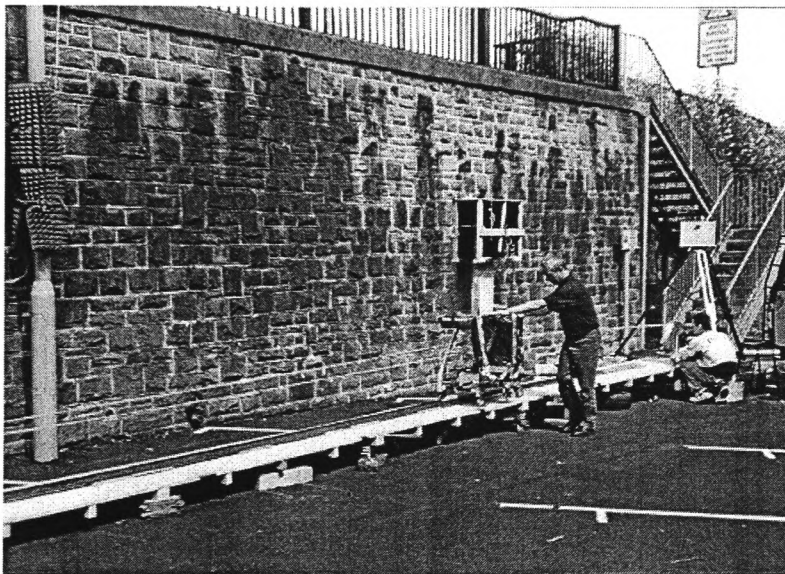
Figure 3-17: Scatter measurement of the wall in Pontypridd car park

3.6.2 J-Block at the University of Glamorgan
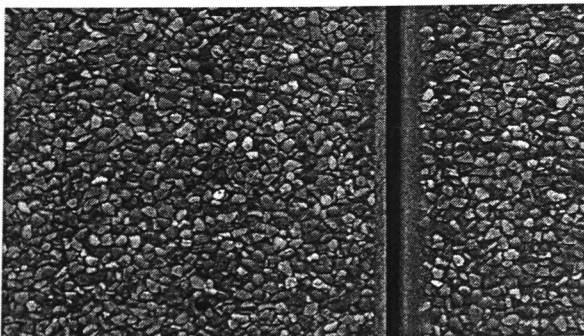
Figure 3-18: Pebble-dash surface inside the University of Glamorgan

Measurements on a pebble-dash surfaces, Figure 3-18, inside the University were also made using exactly the same set-up as the previous one.

4 Reflection and Transmission Functions for Building Materials at Millimetre Waves and their Effects on the Radio Channel

4.1 Introduction

At millimeter wave frequencies the internal layout of a building largely influences the radio paths over which both the wanted signal and interference arrive at an intended receiver location. The mode of propagation in indoor picocells is mainly by a direct ray and reflections off walls and those off ceiling and floor when the antenna radiation pattern does not exclude them. When the line-of-sight is obstructed transmission through partitions, ceiling and floor needs to be accounted for. Therefore it is necessary to understand and model the reflection and transmission mechanisms at millimetre waves when the thickness of the partition is not too large compared to a wavelength. With the knowledge of the reflectivity and transmissivity characteristics of building materials, the type of materials used for partitioning may then be chosen for the planning of microcellular radio links.

This chapter presents a theoretical model, based on multiple successive internal reflections, to characterize the reflection and transmission mechanisms at millimetre waves. Results of experiments made inside an anechoic chamber on various smooth building materials are presented together with theoretical predictions. Values for dielectric parameters have been obtained from theoretical and measured results using the Root Mean Square (RMS) and the Bootstrap techniques. Measurements and predictions have been made for both Vertical-Vertical (VV) and Horizontal-Horizontal (HH) polarisations.

The change in the mobile radio channel characteristics that may occur when reflections off surfaces follow the multiple successive internal reflection phenomenon and not the well-known Fresnel coefficients has been investigated using a ray-tracing algorithm. This algorithm allows a direct ray, single reflections off walls, ceiling and floor,

double reflections off opposite walls and those off adjacent walls. In total 15 rays may be calculated.

4.1.1   Fresnel Reflection and Transmission Coefficients

Let an incident electromagnetic wave, E_i, impinging on an infinite material vertically orientated and defined by medium 2. The electric field of E_i is parallel to medium 2 and perpendicular to the plane of incidence. E_i strikes the material at an incident angle θ_i which is partially reflected, E_r, from and partially refracted, E_t, through the material. Due to the characterization of the material the refracted electromagnetic wave, E_t, propagates though medium 2 at a refracted angle, θ_t. Both media are defined by the dielectric parameters, i.e. ε_1, μ_1 and σ_1 for medium 1 (where medium 1 is the free space), and ε_2, μ_2 and σ_2 for medium 2.
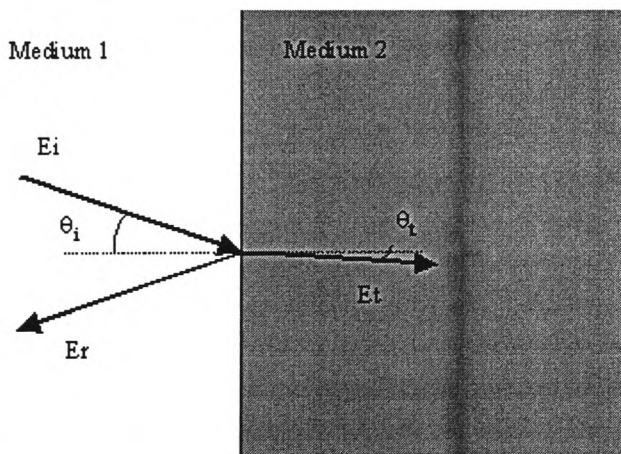
Figure 4-1: Responses of an incident electromagnetic wave, in medium 1, impinging on an infinite material, in medium 2

Ideally, waves impinge upon smooth surfaces where the reflected and refracted powers are expressed from the Fresnel coefficients [Balanis, 1989]. The general Fresnel reflection and transmission coefficients of a linearly polarised wave incident in the boundary between two infinite media, as shown in Figure 4-1, are given by:

Reflection and transmission coefficients for vertical polarisation.

$$\rho_V(\theta_i, f, \varepsilon_r, \mu, \sigma) = \frac{Z_2 \cos\theta_i - Z_1 \cos\theta_t}{Z_2 \cos\theta_i + Z_1 \cos\theta_t} \qquad (4\text{-}1)$$

$$\tau_V = 1 + \rho_V \tag{4-2}$$

Reflection and transmission coefficients for horizontal polarization.

$$\rho_H(\theta_i, f, \varepsilon_r, \mu, \sigma) = \frac{Z_2 \cos\theta_t - Z_1 \cos\theta_i}{Z_2 \cos\theta_t + Z_1 \cos\theta_i} \tag{4-3}$$

$$\tau_H = \left(\frac{\cos(\theta_i)}{\cos(\theta_t)} \right) \cdot (1 + \rho_H) \tag{4-4}$$

Where: -

$$Z_1 = \sqrt{\frac{\mu_0}{\varepsilon_0}} \tag{4-5}$$

$$Z_2 = \frac{j\omega\mu}{v} \tag{4-6}$$

$$\omega = 2\pi f \tag{4-7}$$

$$\cos\theta_t = \sqrt{1 - \left(\frac{\eta_1}{\eta_2}\right)^2 \sin^2\theta_i} \tag{4-8}$$

$$\left(\frac{\eta_1}{\eta_2}\right)^2 = \left(\frac{j\omega\sqrt{\varepsilon_0\mu_0}}{v}\right)^2 \tag{4-9}$$

$$v^2 = \omega^2\mu\varepsilon\left(j\frac{\sigma}{\omega\varepsilon} - 1\right) \tag{4-10}$$

And Z_1 is the free space impedance, in Ohms;

Z_2 is medium 2 intrinsic impedance, in Ohms;

θ_t is the refraction angle (radian);

$\left(\dfrac{\eta_1}{\eta_2}\right)^2$ are the refraction indices of free space and medium respectively;

v^2 is the propagation constant;

θ_i is the incident angle, in radians;

ω is the angular frequency, in radians per second;

ε_r, ε_0, μ_r, μ_0 and σ representing the dielectric parameters.
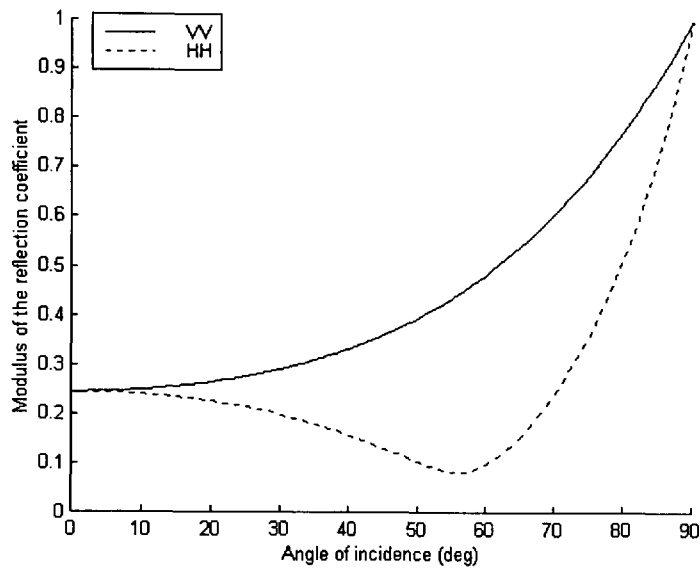
Figure 4-2: Theoretical Fresnel reflection coefficient plotted for $\varepsilon_r=2$ and $\sigma=4$ using vertical and horizontal polarisations

For the case when media are non-magnetic (i.e. $\mu_r=1$) and lossless (i.e. $\sigma=0$) the Fresnel coefficients become as follow: -

Fresnel reflection and transmission coefficients for vertical polarisation: -

$$\rho_V\left(\theta_i,f,\varepsilon_r,\mu_r=1,\sigma=0\right)=\frac{\cos(\theta_i)-\sqrt{\varepsilon_r-\sin^2(\theta_i)}}{\cos(\theta_i)+\sqrt{\varepsilon_r-\sin^2(\theta_i)}} \qquad (4\text{-}11)$$

$$\tau_V=1+\rho_V \qquad (4\text{-}12)$$

Fresnel reflection and transmission coefficients for horizontal polarisation: -

$$\rho_H\left(\theta_i,f,\varepsilon_r,\mu_r=1,\sigma=0\right)=\frac{-\varepsilon_r\cos(\theta_i)+\sqrt{\varepsilon_r-\sin^2(\theta_i)}}{\varepsilon_r\cos(\theta_i)+\sqrt{\varepsilon_r-\sin^2(\theta_i)}} \qquad (4\text{-}13)$$

$$\tau_H=\left(\frac{\cos(\theta_i)}{\cos(\theta_t)}\right)\left(1+\rho_H\right) \qquad (4\text{-}14)$$
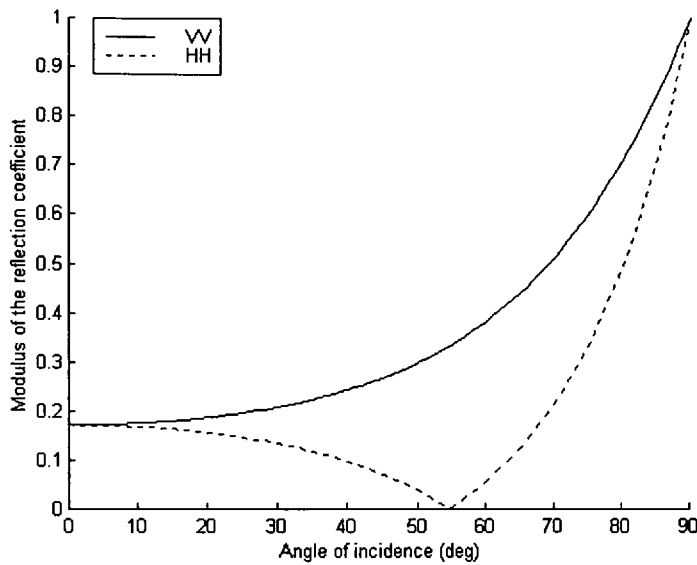
Figure 4-3: Theoretical Fresnel reflection coefficient plotted for $\varepsilon_r=2$ and $\sigma=0$ using vertical and horizontal polarisations

Where: ε_r is the relative permittivity of the medium.

4.1.2 General Reflection and Transmission Coefficients

When the dielectric parameters of a material are known, the Fresnel coefficients give a good representation of the quantity of the power reflected from or refracted through the material. However when the thickness, compared to a wavelength, of a material tends to be relatively small, the Fresnel coefficients lead to significant errors [Heavens, 1955] [Correia, Sept. 1994]. The inaccuracy of the Fresnel coefficients can be explained by the presence of a third medium giving additional contributions. Indeed when medium 2, being the material, is too thin (compared to the wavelength), medium 3 appears as shown on Figure 4-4.

To ease the understanding of the phenomenon encountered, Geometrical Optics (GO) has been used. The electromagnetic wave striking the material is assumed to be ray like. The incident ray is then reflected from the surface and experiences multiple internal reflection as is shown in Figure 4-4. The number of internal reflections is determined by the attenuation specific to the material.
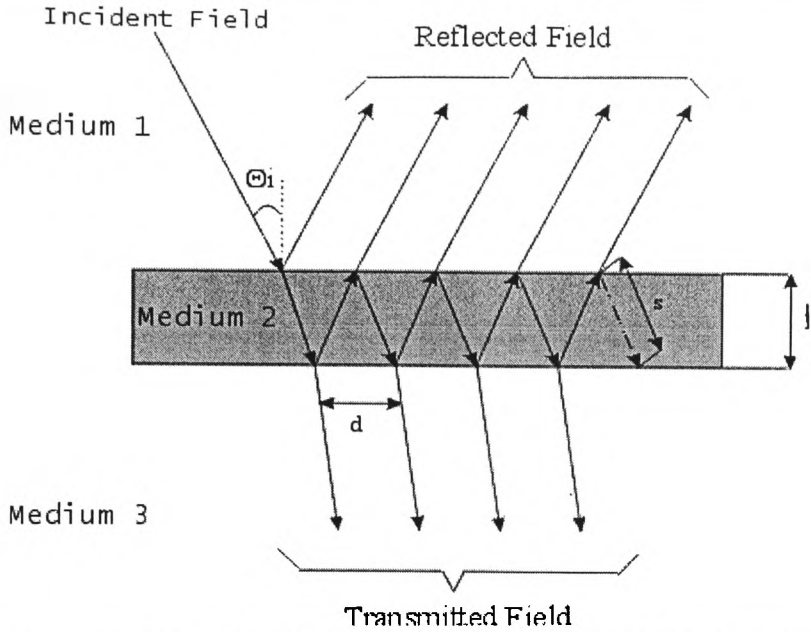
Figure 4-4: Reflection and transmission model based on multiple successive reflection

All rays reflected back to medium 1 and those reaching to medium 3 will add up to form the overall reflected and transmitted power signal respectively. Using this concept it is then possible to formulate a general reflection and transmission coefficient taking into consideration the thickness, the dielectric parameters of the material and the angle of incidence. The summation of all those rays forms a geometrical series which in its convergent form yield general reflection and transmission coefficients given by (4-15) and (4-16). Detailed derivation of these coefficients is given in Appendix 1.

The general reflection coefficient: -

$$\Gamma_g = \frac{\rho - \rho \cdot e^{-j \cdot 2 \cdot k \cdot s} e^{-2 \cdot \alpha \cdot s} e^{j \cdot ko \cdot d \cdot \sin\theta_i}}{1 - \rho^2 e^{-j \cdot 2 \cdot k \cdot s} e^{-2 \cdot \alpha \cdot s} e^{j \cdot ko \cdot d \cdot \sin\theta_i}} \qquad (4\text{-}15)$$

The general transmission coefficient: -

$$T_g = \frac{(1 - \rho^2) e^{-j \cdot k \cdot s} e^{-\alpha \cdot s}}{1 - \rho^2 e^{-j \cdot 2 \cdot k \cdot s} e^{-2 \cdot \alpha \cdot s} e^{j \cdot ko \cdot d \cdot \sin\theta_i}} \qquad (4\text{-}16)$$

Where: -

$$k = \frac{2\pi}{\lambda} \sqrt{\varepsilon_r} \qquad (4\text{-}17)$$

$$\alpha = \frac{60\pi\sigma}{\sqrt{\varepsilon_r}}$$ (4-18)

$$k_o = \frac{2\pi}{\lambda}$$ (4-19)

$$s = \frac{l'}{\sqrt{1 - \dfrac{\sin^2\theta}{\varepsilon_r}}}$$ (4-20)

$$d = \frac{2l'}{\sqrt{\dfrac{\varepsilon_r}{\sin^2\theta} - 1}}$$ (4-21)

And k is the propagation constant (rad/m);

α is the attenuation proper to the material (Np/m);

k_o is the propagation in free space (rad/m);

s is the path length inside the slab (m);

l' is the thickness of the material (m);

d being the path length difference between two out-going rays, see Figure 4-7.

ρ is either the vertical or horizontal Fresnel reflection coefficient. The reflected and transmitted powers are defined as follow:

$$P_r = |\Gamma_g|^2.Pi$$ (4-22)

$$P_t = |T_g|^2.Pi$$ (4-23)

Where P_r is the reflected power (Watt);

P_t the transmitted power (Watt);

Γ_g the general reflection coefficient;

T_g the general transmission coefficient.

4.1.3   Fresnel Reflection Coefficients Versus the General Reflection Coefficients

Figure 4-5 shows theoretical predictions of the reflection coefficient obtained from the model developed here as a function of angle of incidence for a smooth material with $\varepsilon_r=2$ and $\sigma=0.14$ and various thickness values together with the Fresnel coefficients.
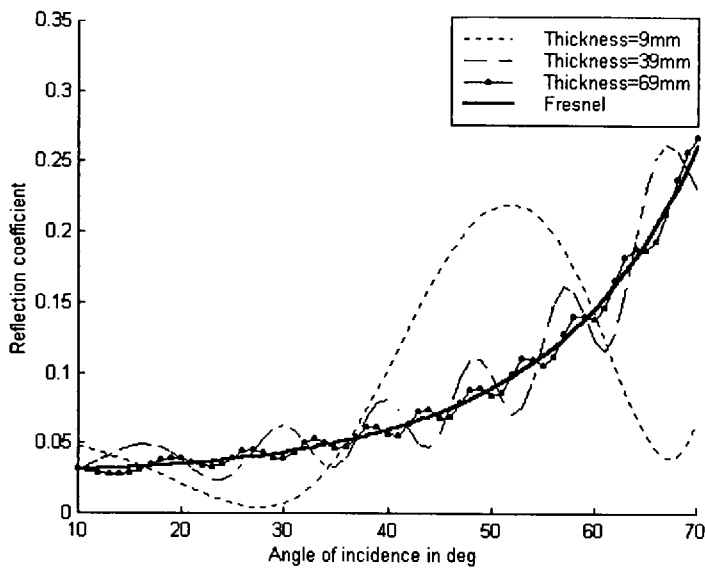
Figure 4-5: Fresnel and multiple successive reflection coefficients calculated for a smooth material with $\varepsilon_r=2$ and $\sigma=0.14$ and various thickness values
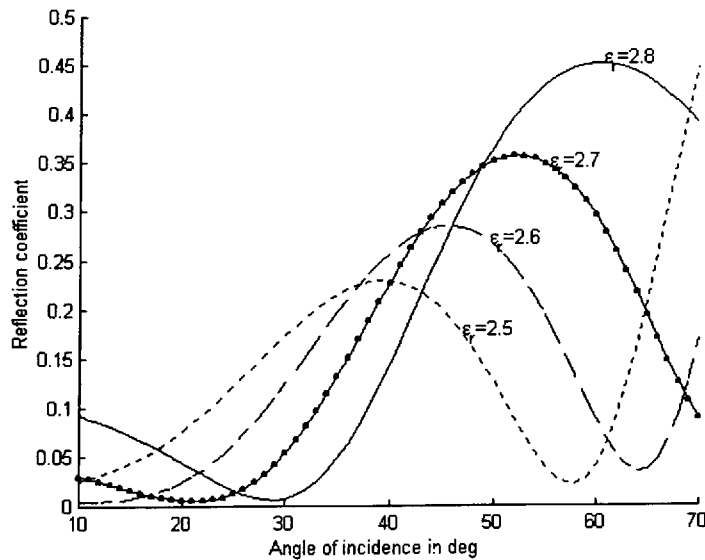
Figure 4-6: Theoretical reflection coefficient computed for a 9mm thick material with $\sigma=0.14$ and various values of ε_r

These results show that the reflection coefficient obtained using the multiple successive reflection model becomes comparable to that obtained from Fresnel when the thickness of the material increases. This can be easily explained as when the thickness of the material increases, reflections inside the material, see Figure 4-4, become weaker

and the first reflected ray would be the most significant contributor to the reflected signal power.

The sensitivity of the theoretical model developed here to small changes of ε_r and σ has been investigated. Figure 4-6 shows the reflection coefficient computed for a 9mm thick material with $\sigma=0.14$ and various values of ε_r.

It can be clearly seen that a small increase in the value of ε_r results in altering the position and amplitude of the peaks and troughs of the reflection function. In a similar way the effect of small changes in the value of σ has been examined by fixing the permittivity ($\varepsilon_r=2$) as shown in Figure 4-7.
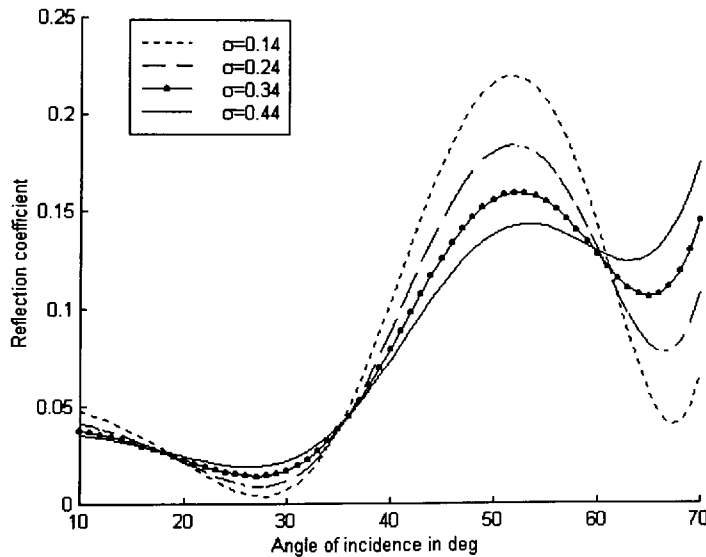
Figure 4-7: Reflection coefficients computed for a 9mm thick material with $\varepsilon_r=2$ and various values of σ

It is evident that the peaks and troughs remain to occur at the same angle. The permittivity and the conductivity affect the values of the reflection coefficients differently. As the permittivity increases the material is more able to store energy and thus the transfer of energy takes longer. This explains the shift in the reflectivity function and the change in the amplitude level in Figure 4-6. On the other hand if the conductivity increases the material will warm up quicker and thus attenuates more the received signal. In this manner the reflectivity function will be attenuated and if the attenuation is important the material's response will lead to the Fresnel coefficients.

Any shift in a material's response can be quantified by calculating its derivative function at the incident angle chosen as in [Shimabukuro (July 1984)].

4.2 Extracting the Dielectric Parameters

As described in chapter 3 the reflectivity and transmissivity functions were measured as function of the angle of incidence. The measured functions have been compared with theoretical predictions obtained from the multiple successive reflection model. The estimated values of ε_r and σ were obtained by finding the "best" fit. Two techniques were employed to extract the dielectric parameters from the measured functions. Those techniques are the Root Mean Square error (RMS) and the Bootstrap.

Due to fluctuations in the reflectivity and transmissivity functions the coefficients for angles of incidence ranging were between 10° and 70° in 4° increment.

4.2.1 Root Mean Square (RMS)

The Root Mean Square (RMS) error between the measured reflection coefficient, E_n, at the nth angle of incidence and the predicted one, T_n, is given by: -

$$RMS = \sqrt{\sum_{n=1}^{N} \frac{(T_n(\varepsilon_r, \sigma) - E_n)^2}{n}}$$

(4-24)

Where: T is the coefficient calculated using either (4-15) or (4-16);

E is the measured coefficient.

When both the reflectivity and transmissivity measurements were used the overall RMS error is: -

$$RMS_{RT} = \sqrt{\sum_{n=1}^{N} \frac{(\tau_n(\varepsilon_r, \sigma) - \tau_n')^2}{n} + \sum_{n=1}^{N} \frac{(\rho_n(\varepsilon_r, \sigma) - \rho_n')^2}{n}}$$

(4-25)

Where: τ is the computed transmission coefficient;

ρ is the computed reflection coefficient;

τ' is the measured transmission coefficient;

ρ' is the measured reflection coefficient.

The values of the dielectric parameters that give the least RMS error were held and assigned for the material. This was done by varying the permittivity between 1 and 30 and 0 and 2 for the conductivity.

4.2.2 Bootstrap

On the contrary to the RMS, this technique uses the Least Square Fit (LSF) function to compare theoretical and experimental data points and then employs the bootstrap procedure [Efron, 1993] and [Lähteenmäki, August 1996] to evaluate the possible error margin of the estimates.

The LSF is given by: -

$$LSF = \sum_{n=1}^{N} \frac{\left((T_n(\varepsilon_r, \sigma) - E_n)^2 \right)}{n}$$

(4-26)

Where: T expresses the theoretical data points by either (4-15) or (4-16);

E is the experimental data points;

N is the total number of samples.

The formula (4-26) is generalized to include both the reflectivity and transmissivity measurements.

$$LSF_{RT} = \sum_{n=1}^{N} \frac{\left(\tau_n(\varepsilon_r, \sigma) - \tau'_n \right)^2}{n} + \sum_{n=1}^{N} \frac{\left(\rho_n(\varepsilon_r, \sigma) - \rho'_n \right)^2}{n}$$

(4-27)

Once a theoretical fit has been found, the difference between each experimental and theoretical point is calculated. Those differences are then added randomly to the theoretical points. The resulting curve is then considered as being a new measured set of points and the process is repeated a number of times. The values of the dielectric parameters are then found by averaging the results obtained each time. This technique assumes that errors existing between theoretical and experimental values are

independent from one another and are identically distributed. Using this procedure the measured coefficient may be expressed as: -

$$E_i = T_i(\varepsilon_r, \sigma) + r_i \qquad (4-28)$$

i=1, 2, ..., N

Where: E_i is the measured coefficient;

T_i, is the coefficient calculated using either (4-15) or (4-16) for a given ε_r and σ;

r_i the error between measured and calculated coefficients.

Once the parameters are estimated differences between theoretical and experimental points are calculated using:

$$r_i = E_i - T_i(\varepsilon_r, \sigma) \qquad (4-29)$$

Those residuals are then added to the computed coefficient to obtain a new measured point as given by: -

$$E_{bi} = T_i(\varepsilon_r, \sigma) + r_{bi} \qquad (4-30)$$

Where: r_{bi} is any difference calculated from (4-29) and randomly chosen with a probability of $\dfrac{1}{N}$.

Using this procedure, the LSF is then used to obtain new estimates of the material dielectric parameters. This process is repeated k times to finally extract the dielectric parameters. In the simulation used the process was repeated 20 times. The average of the dielectric parameters is given by: -

$$\varepsilon_{rb} = \frac{1}{k}\sum_1^k \varepsilon_m \qquad (4-31)$$

$$\sigma_{rb} = \frac{1}{k}\sum_1^k \sigma_m \qquad (4-32)$$

Where: ε_{rb} is the average permittivity;

σ_{rb} is the average conductivity.

Hence the covariance matrix of each estimated value of ε_r and σ provides the error margin of the estimates. The error margin of the permittivity, ε_r, and the conductivity, σ, are given by: -

$$\varepsilon_{rm} = \frac{1}{k-1} \sum_{1}^{k} (\varepsilon_m - \varepsilon_{rb})(\varepsilon_m - \varepsilon_{rb})^t \qquad (4\text{-}33)$$

$$\sigma_{rm} = \frac{1}{k-1} \sum_{1}^{k} (\sigma_m - \sigma_{rb})(\sigma_m - \sigma_{rb})^t \qquad (4\text{-}34)$$

Where: $(\ )^t$ represents the transpose of the matrix.

4.3 Building materials

Measurements inside the anechoic chamber were made to characterize the reflectivity and transmissivity as functions of the angle of incidence. The measurements were made using vertical-vertical and horizontal-horizontal polarizations on various building materials. The materials used are given in Table 1.

Each material was standing upright on a top of a high precision computed controlled rotary table. The measurement on each material was repeated four times under identical conditions in order to ensure repeatability of results and minimise errors that may occur in the set-up.

Table 4-1: Building materials tested

Materials	Thickness		Size (LengthxWidth) in cm
	mm	λ	
Plasterboard	9	1.872	120 x 90
Plasterboard	13	2.704	120 x 90
Polystyrene	49	10.192	120 x 90
Fireboard	12.7	2.6416	120 x 90
Glass	4.2	0.874	120 x 90
Pattern Glass	3	0.624	120 x 90
Concrete slab	25.4	5.283	90 x 70
Plywood	5	1.04	120 x 90

4.3.1 Experimental and Theoretical Reflectivity and Transmissivity Functions

The first set of measurement was made using vertically polarized 25 dBi horn antennas at both the transmitter and the receiver ends. Results of reflection measurements made on a 9 mm thick plasterboard exhibit specular behavior and are shown in Figure 4-8.
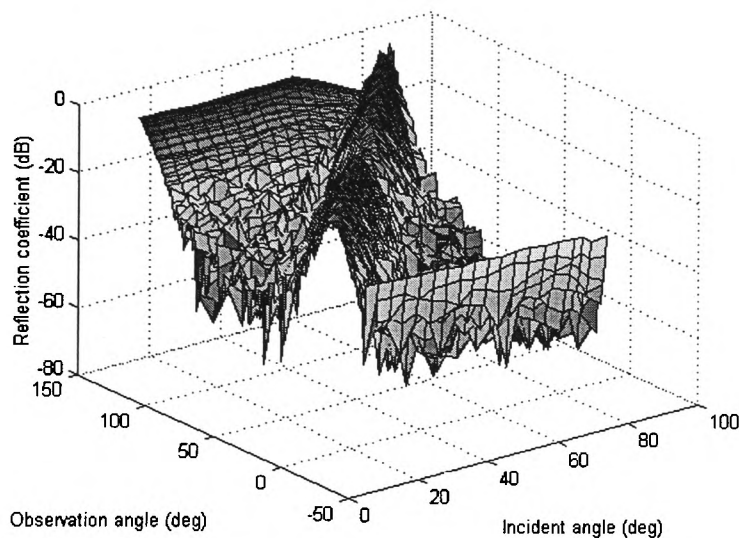
Figure 4-8: Reflection coefficient measured for a 9 mm thick plasterboard as function of the observation and incident angles

This 3-D plot shows the measured reflection coefficient, obtained by normalizing the signal to the level obtained for a smooth metal surface, as a function of the observation and incident angles. The maximum values obtained during the reflectivity and transmissivity measurements are then detected and plotted against the angle of incidence as shown in Figure 4-9. These results show that while the reflection coefficient increases the transmission coefficient decreases.

The theoretical model developed here has been used to predict the behaviour of both functions and, at the same time, provides estimates of the dielectric parameters for the material under test. It has been noted that both reflection and transmission functions have to be considered when estimating the values of the dielectric parameters. This is also necessary to achieve a good qualitative and quantitative agreement between measured and computed values. It has been noted that using one function only (either

reflectivity or transmissivity) may yield to inaccurate results.
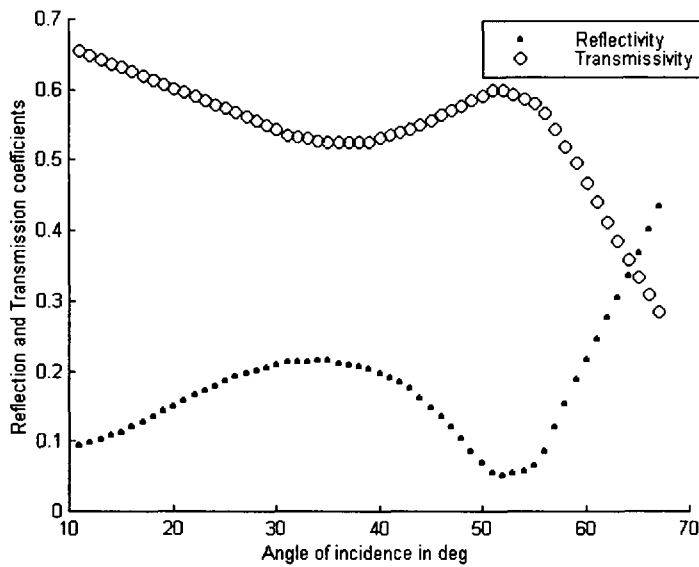
Figure 4-9: Reflectivity and transmissivity functions measured for a 9 mm thick plasterboard as function of the angle of incidence
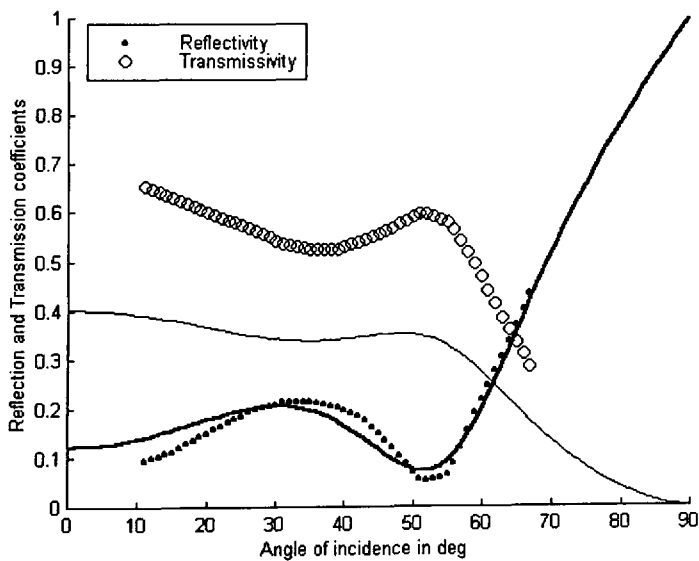
Figure 4-10: Measured reflection and transmission coefficients, in dotted line, for the 9 mm plasterboard together with theoretical predictions (solid line) for ε_r=3.2 and σ=0.38

The values of the dielectric parameters estimated, using the RMS technique for the 9 mm thick plasterboard and reflection measurements only were ε_r=3.2 and σ=0.38. Using these values, the reflection and transmission coefficients were computed and

plotted as in Figure 4-10, together with measured values. Results clearly show that although measured and computed reflectivity values are in a reasonably good agreement (RMS error=0.025), the calculated transmission values are significantly lower than the measured ones. The RMS error between measured and computed transmissivity values is 0.215.
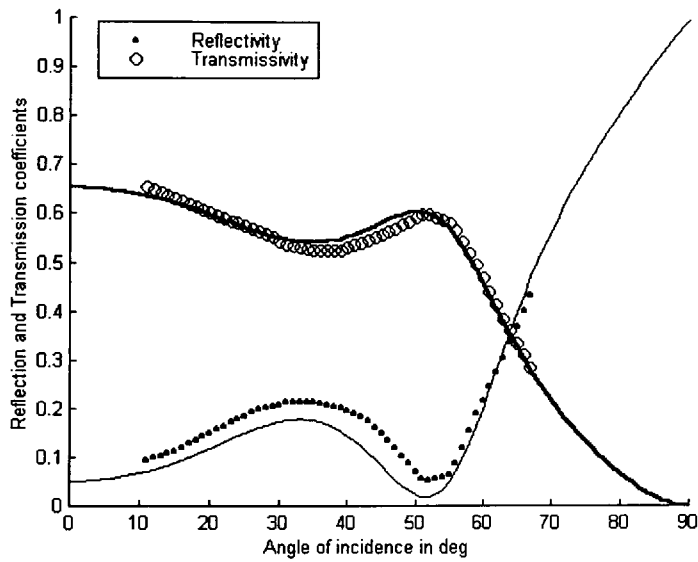
Figure 4-11: Measured reflection and transmission coefficients (dotted line) for the 9 mm plasterboard together with theoretical predictions for $\varepsilon_r=2.4$ and $\sigma=0.16$

On the other hand, using transmissivity measurements only, yields an estimated values of $\varepsilon_r=2.4$ and $\sigma=0.16$. Using these values a good fit has been achieved for both transmissivity and reflectivity results with RMS errors of 0.039 (transmissivity) and 0.04 (reflectivity) as is shown in Figure 4-11.

The values of the dielectric parameters estimated by considering either transmissivity or reflectivity coefficient differ considerably, and therefore taking into account only one function may yield to inaccurate extraction of the dielectric parameters. For this reason, both reflectivity and transmissivity measurements have been considered when estimating the values of the dielectric parameters.

It is difficult to conclude whether fitting to either reflectivity or transmissivity will always yield accurate estimates. Investigations carried out on the materials tested here have shown that estimates obtained by fitting to both measured results are somewhat different to those obtained when either transmissivity or reflectivity is used. The results

obtained for a 9mm thick plasterboard by fitting to both reflectivity and transmissivity results are similar to those obtained by fitting to transmissivity only and shown in Figure 4-11.

4.3.1.1   9 mm Thick Plasterboard

For each material tested measurements were repeated four times under identical conditions in order to ensure the repeatability of the measurements and minimise experimental errors. Results obtained for the 9 mm thick plasterboard are given in Figure 4-12. The solid line represents the average of the four measurements.

Table 4-2: Dielectric parameters estimated for a 9 mm plasterboard using four different reflectivity and transmissivity measurements

Materials	ε_r	σ	RMS error
Pb9_r1	2.4	0.15	0.044
Pb9_r2	2.4	0.15	0.040
Pb9_r3	2.4	0.17	0.047
Pb9_r4	2.4	0.17	0.038

For each measurement the reflectivity and transmissivity functions have been processed using the RMS and Bootstrap techniques to estimate the values of the dielectric parameters, and to predict the theoretical functions. Results obtained for each of the four measurements, using the RMS technique, are shown in Table 4-2.
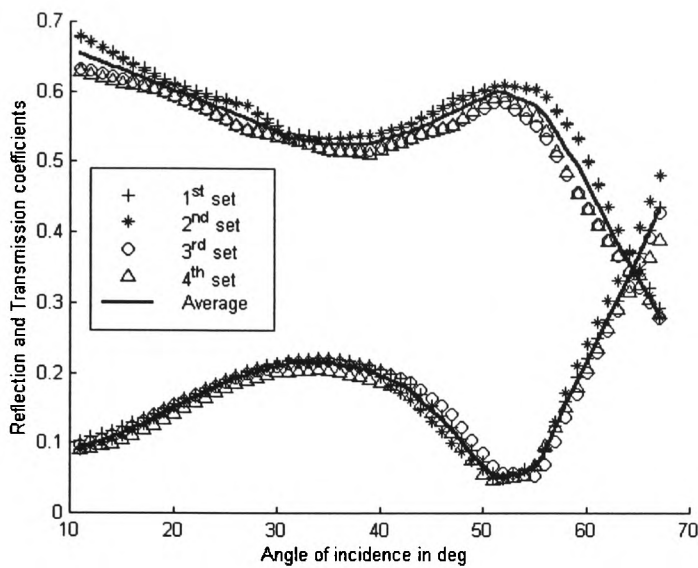
Figure 4-12: Measured reflection and transmission coefficients repeated on the 9 mm thick plasterboard together with the average curve
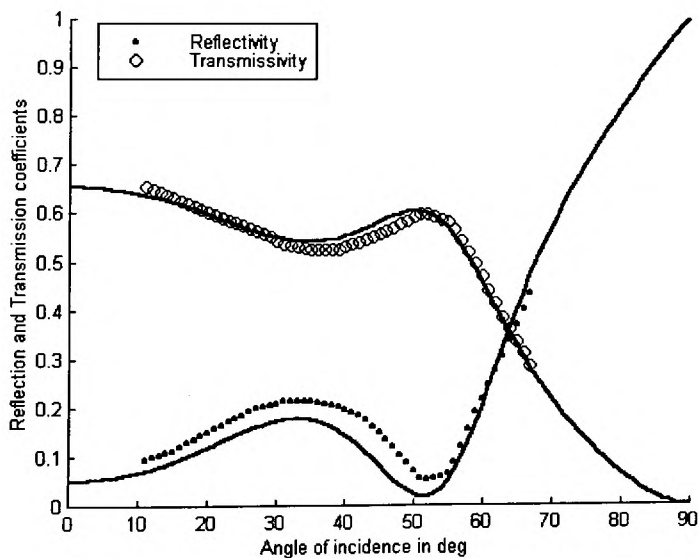
Figure 4-13: Measured and predicted transmissivity and reflectivity functions for a 9 mm thick plasterboard with ε_r=2.4 and σ=0.16

In order to reduce experimental errors and provide accurate estimates, the average of the reflection and transmission coefficients has been calculated. The dielectric parameters estimated from these averaged values were found to be ε_r=2.4 and σ=0.16 with a general RMS_{RT} error of 0.04. Figure 4-13 shows a comparison between theoretical and experimental results.

The averaged measured values have also been processed, using the Bootstrap technique, and results are given in Figure 4-14. In this case the estimated values are $\varepsilon_r=2.33\pm2\cdot10^{-3}$ and $\sigma=0.11\pm8\cdot10^{-5}$. These values differ from those estimated using the RMS technique. The discrepancies present between theoretical and measured values of Figure 4-14 are explained by the fact that the Bootstrap technique accounts for all possible fluctuations in each measured point as explained earlier. Therefore, the Bootstrap technique looks for all possible fluctuations in the collected points until the best theoretical fit, that is included in all those fluctuations, is found.
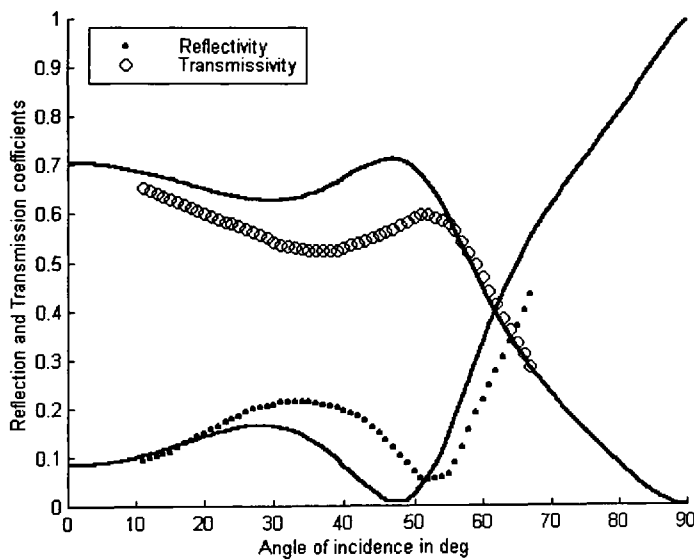
Figure 4-14: Measured and predicted functions for a 9 mm thick plasterboard with $\varepsilon_r=2.33$ and $\sigma=0.11$ as obtained from the Bootstrap technique

4.3.1.2 13 mm Thick Plasterboard

Results of the four experimental measurements together with the average function obtained for the 13 mm plasterboard are shown in Figure 4-15. The average transmission and reflection coefficients have been processed using the RMS and Bootstrap techniques, and results are shown in Figure 4-16 and Figure 4-17 respectively. The estimated values of the dielectric parameters are given in table 4-3.

Table 4-3: Dielectric parameters computed for a 13 mm thick plasterboard using the RMS and Bootstrap techniques

	RMS technique RMS error=0.063	Bootstrap technique
ε_r	2.6	2.6±0
σ	0.05	0.035±0
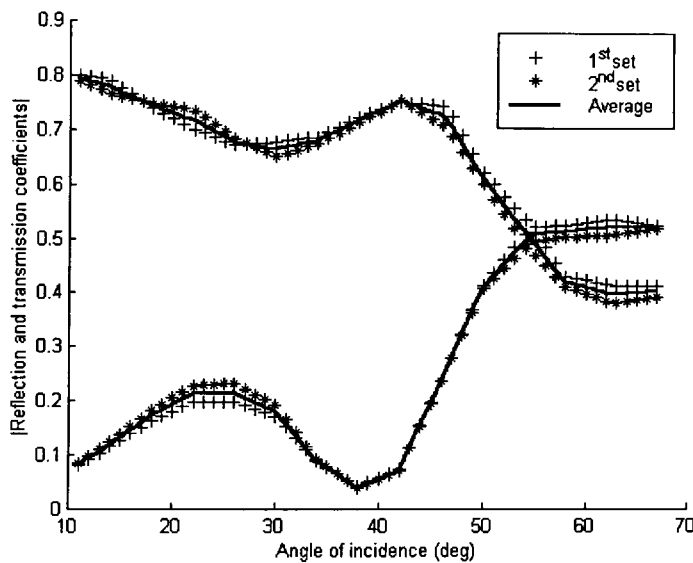
Figure 4-15: Measured reflection and transmission coefficients repeated for a 13 mm thick plasterboard together with the average curve

The solutions obtained using both techniques are in good agreement with a higher value of σ obtained using the RMS method which has the effect of lowering the value of the coefficients.

It can be remarked that the solutions calculated for the 13mm thick plasterboard are slightly different from those obtained for the 9 mm thick plasterboard. Indeed estimates show an increase in the permittivity and a decrease in the conductivity values. Furthermore from Figure 4-12 and Figure 4-15 it is noticed that the level of the transmissivity is higher for the 13 mm plasterboard than for the 9 mm plasterboard.
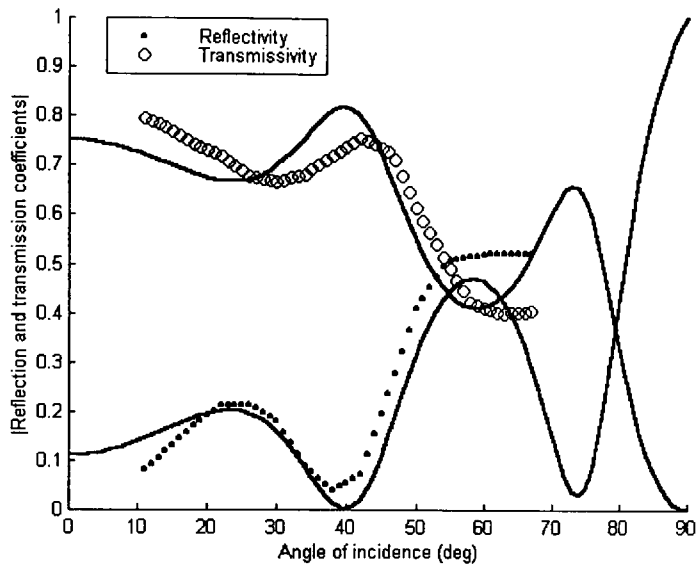
Figure 4-16: Measured and predicted functions for a 13 mm thick plasterboard with ε_r=2.6 and σ=0.05 as obtained from the RMS technique
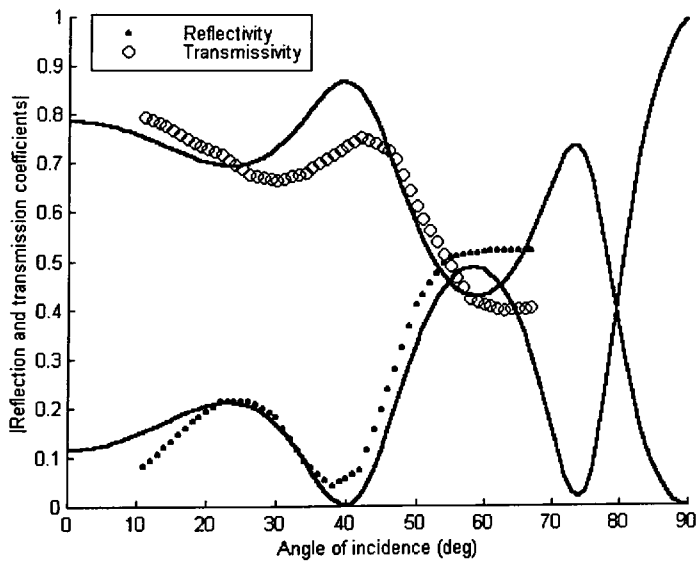
Figure 4-17: Measured and predicted functions for a 13 mm thick plasterboard with ε_r=2.6 and σ=0.035 as obtained from the Bootstrap technique

4.3.1.3   49 mm Thick Polystyrene

Results obtained for the polystyrene are shown in Figure 4-18 together with the best RMS fit. The values of the dielectric parameters obtained using the RMS and Bootstrap techniques are given by table 4-4.

The polystyrene material behaves like the medium air, giving a total transmission without any reflection. However the transmissivity is not exactly equal to 1 which means that part of the incident field was absorbed by the material.

Table 4-4: Dielectric parameters estimated for a 49 mm thick polystyrene using the RMS and Bootstrap techniques

	RMS technique RMS error=0.066	Bootstrap technique
ε_r	1.2	1 ± 0
σ	0	0 ± 0
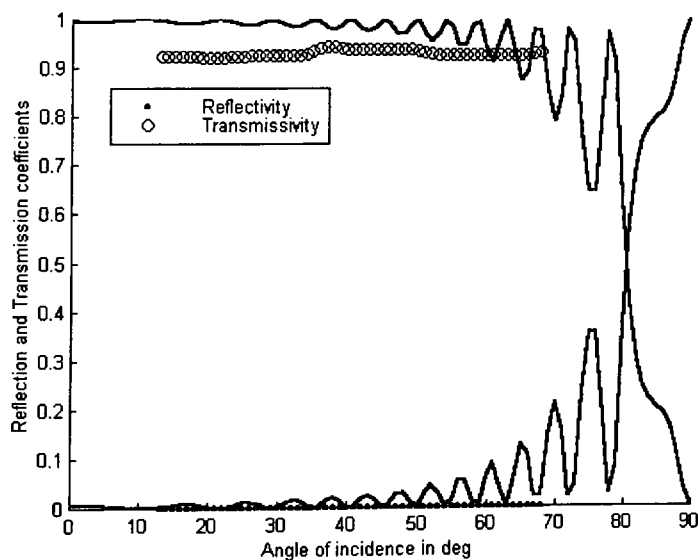
Figure 4-18: Measured and predicted functions for a 49 mm thick polystyrene with ε_r=1.2 and σ=0 as obtained from the RMS technique

4.3.1.4   12.7 mm Thick Fireboard

Fireboards replace plasterboards to prevent against fire. In comparison with plasterboards, fireboards have a denser composition which render them heavier. Fireboards contain glass fibre and additives in the core to improve their fire protection performance.

Figure 4-19 shows the average measured transmission and reflection functions together with the best fit obtained using the RMS technique. The dielectric parameters have been estimated as $\varepsilon_r=2.9$ and $\sigma=0.05$ with an RMS_{RT} error of 0.088. However the values obtained using the Bootstrap technique have been found to be $\varepsilon_r=2.82\pm0.012$ and $\sigma=0.014\pm10^{-4}$.
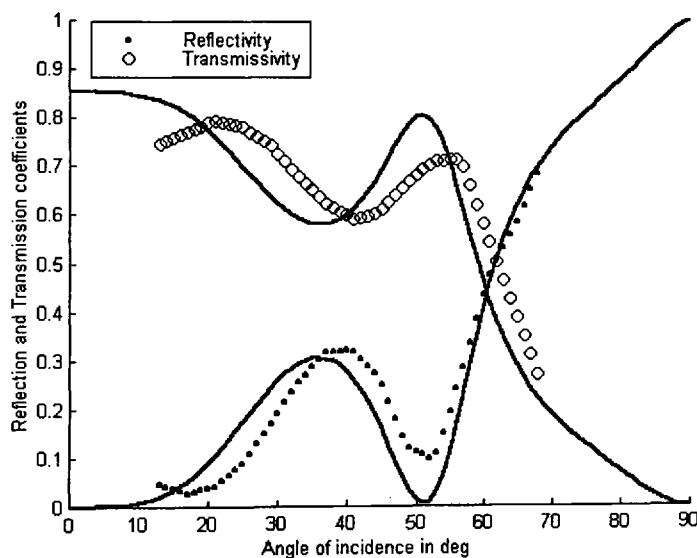
Figure 4-19: Measured and predicted functions for a 12.7 mm thick fireboard with $\varepsilon_r=2.9$ and $\sigma=0.05$ as obtained from the RMS technique

4.3.1.5   1 inch Thick Concrete slab

A smooth 1 inch thick man-made concrete slab manufactured in the School of Built Environment (University of Glamorgan) has been measured. Reflections of the concrete slab have been observed to be specular and the reflection coefficient measured as function of angle of incidence is given in Figure 4-20 together with the best RMS fit.

Because of the high attenuation inside the slab and the limited noise flour of the

receiving system no transmission through the slab has been measured. The dielectric parameters estimated using the RMS technique are $\varepsilon_r=4$ and $\sigma=0.92$ with 0.01 RMS_{RT} error compared to $\varepsilon_r=4\pm0$ and $\sigma=1.308\pm10^{-1}$ for the bootstrap technique.
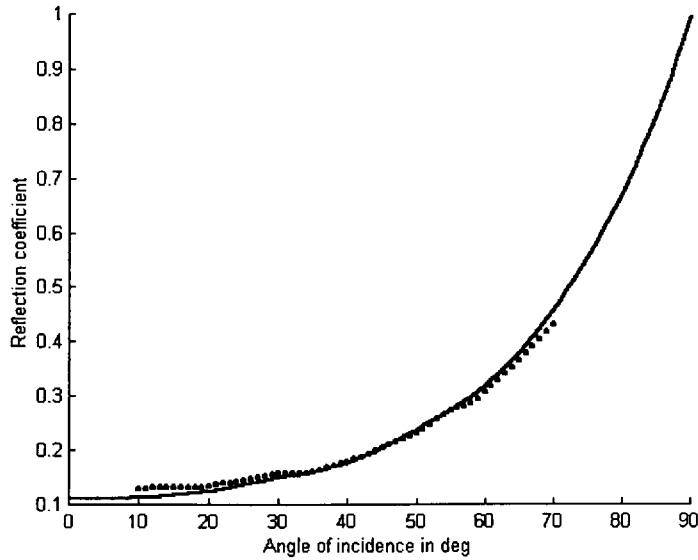
Figure 4-20: Measured and predicted reflection coefficient for a 1 inch thick concrete with $\varepsilon_r=4$ and $\sigma=0.92$ as obtained from the RMS technique

4.3.1.6   5 mm Thick Plywood

Plywood panels are also commonly used in offices. These materials are made of layers of woods glued together by some resins.

Results obtained from this material are given in Figure 4-21 with the estimate values for the dielectric parameters as follow: -

$\varepsilon_r=2.4$ and $\sigma=0.27$ with 0.041 RMS error.

$\varepsilon_r=2.3\pm0$ and $\sigma=0.232\pm3\cdot10^{-4}$, estimated for the Bootstrap technique.
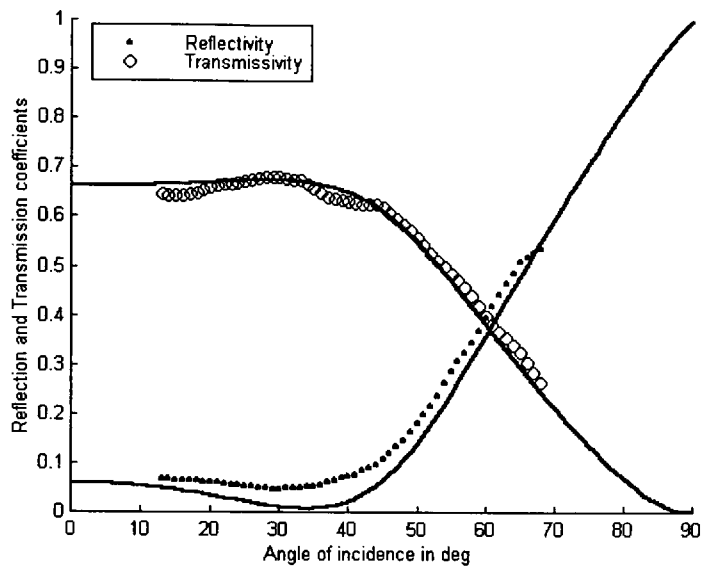
Figure 4-21: Measured and predicted functions obtained for a 5 mm thick plywood with
ε_r=2.4 and σ=0.27 as obtained from the RMS technique

4.3.1.7   3 mm Thick Pattern Glass
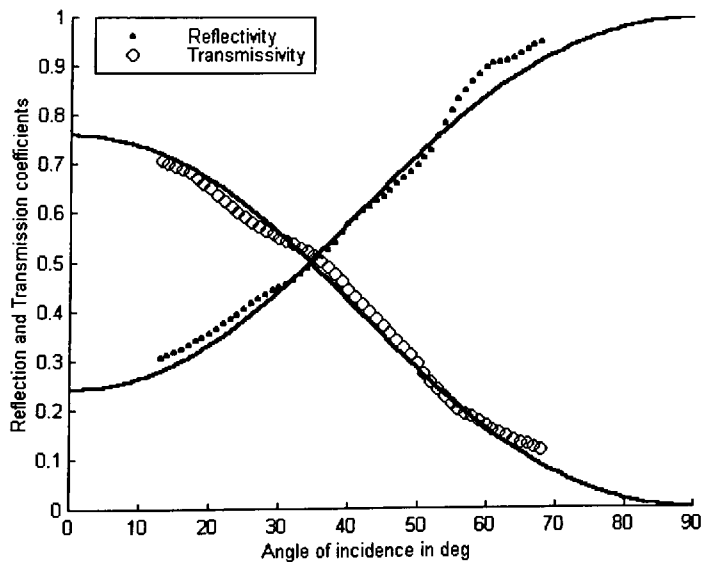
Figure 4-22: Measured and predicted transmission and reflection functions for a 3 mm
thick pattern glass with ε_r=9.6 and σ=0 as obtained from the RMS technique

The pattern glass is most commonly used in bathrooms as its rough surface does not enable to see through. The RMS technique estimates ε_r=9.6 and σ=0 for the pattern glass with an RMS$_{RT}$ error of 0.032, see Figure 4-22.

In Figure 4-23, the bootstrap estimates ε_r=9.86±0.168 and σ=0±0. Both theoretical and experimental curves exhibit good qualitative agreement. The high value of the permittivity measured for this type of glass could be explained by the presence of impurity in the glass making it slightly opaque.
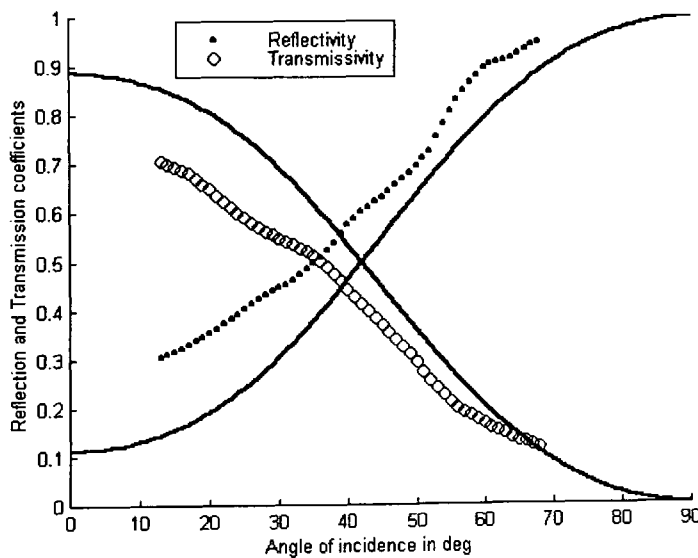
Figure 4-23: Measured and predicted transmission and reflection functions for a 3 mm thick pattern glass with ε_r=9.86 and σ=0 as obtained from the Bootstrap technique

4.3.1.8   4.2 mm Thick Crystal Glass

A thin sheet of glass was tested under similar condition to other materials. When the RMS error technique has been employed to the measured reflectivity and transmissivity functions estimated values of ε_r=8.9 and σ=0.44 with 0.028 RMS$_{RT}$ error have been obtained as can be seen in Figure 4-24. Values of ε_r=11.42±2.86 and σ=0.411±3·10^{-4} have been measured using the bootstrap technique as in Figure 4-25. The bootstrap estimates did not give good agreements between theoretical and experimental results.
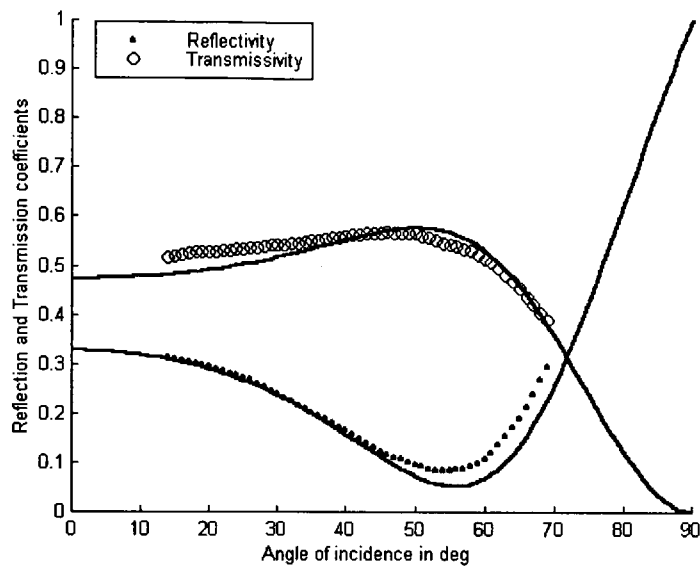
Figure 4-24: Measured and predicted transmission and reflection functions for a 4.2 mm thick glass with ε_r=8.9 and σ=0.44 as obtained from the RMS technique
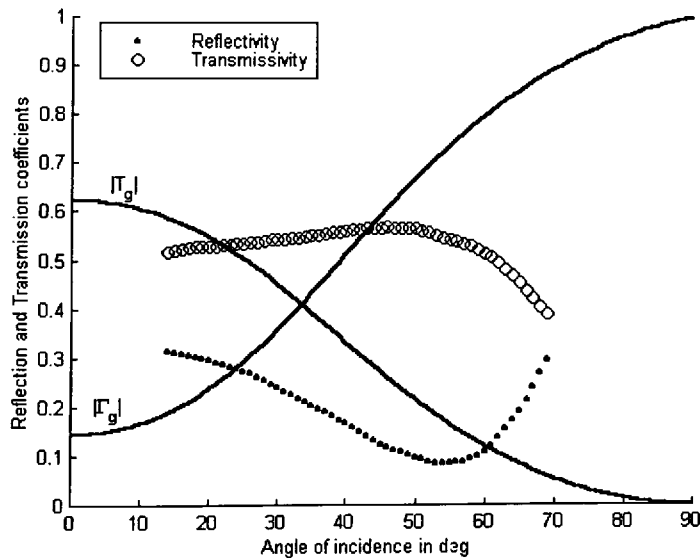
Figure 4-25: Measured and predicted transmission and reflection functions for a 4.2 mm thick glass with ε_r=11.42 and σ=0.411 as obtained from the bootstrap technique

The dielectric parameters obtained for the glass particularly that for the permittivity, are relatively large when comparing with those measured by [Correia, Sept. 1994] and [Manabe, July 1992]. This could be due to the measurement set-up, frequency and the type of material used.

Furthermore as the measured reflectivity and transmissivity do not have pronounced peaks and troughs, both techniques loose their sensitivity to estimate the dielectric parameters. Figure 4-26 shows two different couple of solutions plotted together with the measured reflectivity and transmissivity functions. It can be noted that a change in the permittivity for a fixed conductivity gives similar qualitative agreements with the measurements. In that way it can be concluded that any small errors in the measurements may lead to the selection of another couple of solutions.
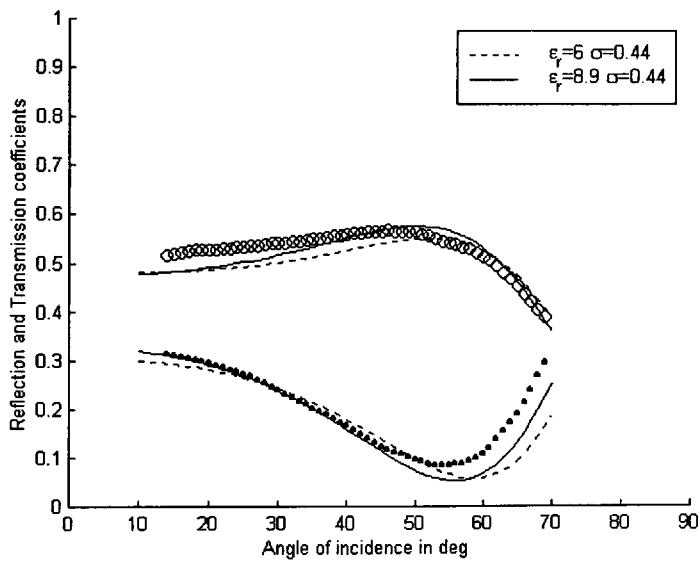
Figure 4-26: Theoretical reflection coefficient represented for a 4.2 mm thick glass using different values of combinations for ε_r and σ

4.3.2 Composite materials

Measurements have been made on a 28 mm thick thermalboard which consists of a 9 mm thick plasterboard glued to a 19 mm thick polystyrene. The measured reflection and transmission coefficients of this composite material are plotted in Figure 4-27. This figure also shows the results obtained for the 9 mm thick plasterboard. It can be seen that the measured reflection and transmission coefficients for the thermalboard are not significantly different to those obtained for the 9 mm plasterboard.

It may be concluded that the polystyrene hardly reflects anything, and the transmission through the plasterboard would be passed on totally through the polystyrene with slight attenuation.

As for the single layer material, [Heavens, 1955] and [Sato, Dec.1997] have studied composite materials. In this case the refracted ray interacts with the different layers, and therefore the modeling process requires a longer computation time. This is only possible if each layer characteristics, ε_r and σ, are known.
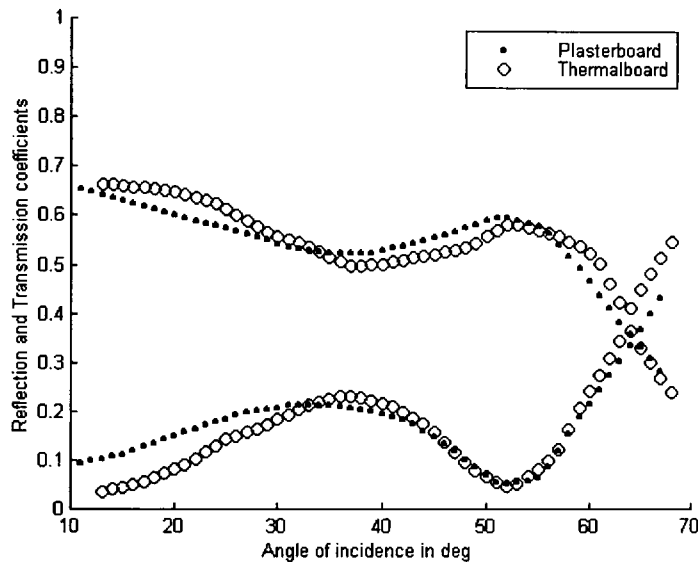
Figure 4-27: Measured reflection and transmission coefficients for a 28 mm thick thermalboard together with those obtained for a 9 mm thick plasterboard

4.3.3 Summary of Experimental Results and Comparison with Published Results

Estimates of the values of the dielectric parameters have been obtained by fitting to both transmissivity and reflectivity measurements. It has been demonstrated that fitting to either reflectivity or transmissivity may yield to inaccurate estimates of the dielectric parameters. Theoretical predictions obtained using the RMS and Bootstrap techniques have shown good qualitative agreements with the experimental results. The dielectric parameters obtained for all materials tested are summarized in Table 4-5.

Some work in this field has been reported by [Correia, Sept. 1994], [Sato, Dec. 1997], [Manabe, July 1992] and [Lähteenmäki, August 1996] and results are given in Table 4-6. Results presented in this thesis are generally in good agreement with reported values. However larger values have been measured for the glass.

It can be observed from Table 4-6 that the values reported for glass exhibit large fluctuations with the permittivity estimated at 5.29 [Correia, Sept. 1994] and 7.51 [Sato, Dec. 1997].

Table 4-5: Estimated dielectric parameters

Materials	RMS Technique		Bootstrap Technique	
	ε_r	σ	ε_r	σ
Plasterboard 9 mm	2.4	0.16	2.33±0.002	0.107±8·10⁻⁵
Plasterboard 13 mm	2.6	0.05	2.6±0	0.035±2·10⁻⁵
Polystyrene 49 mm	1.2	0	1±0	0±0
Fireboard 12.7 mm	2.9	0.05	2.82±0.012	0.014±10⁻⁴
Glass 4.2 mm	8.9	0.44	11.42±2.86	0.411±3·10⁻⁴
Pattern Glass 3 mm	9.6	0	9.86±0.17	0±0
Concrete Slab 1 inch	4.4	1.08	4±0	1.308±10⁻¹
Plywood 5 mm	2.4	0.27	2.3±0	0.232±3·10⁻⁴

Table 4-6: Reported values for dielectric parameters

Materials	[Correia, Sept. 1994] f=60.2GHz		[Sato, Dec. 1997] f=57.5GHz		[Manabe, July 1992] f=57-58GHz		[Lähteenmäki, August 1996] f=59.5GHz	
	ε_r	σ	ε_r	σ	ε_r	σ	ε_r	σ
Plasterboard	2.81	0.15	2.25	0.096	-	-	2.58	0.021
Thickness			12 mm					
Glass	5.29	0.85	7.51	0.62	6.81	0.575	-	-
Thickness			6.8 mm		8-80 mm			
Concrete	6.14	1.01	-	-	-	-	-	-
Chipboard	2.86	0.53	-	-	-	-	2.95	0.19
Wood	1.57	0.32	-	-	-	-	-	-

4.3.4 Effects of Polarisation on Dielectric Parameters

Measurements have also been repeated under identical conditions for all the materials but with horizontally polarized antennas. Both RMS error and Bootstrap techniques were employed to estimate the values of the dielectric parameters. Figure 4-

28 shows results obtained for the 9mm thick plasterboard together with results measured
using HH polarisation.
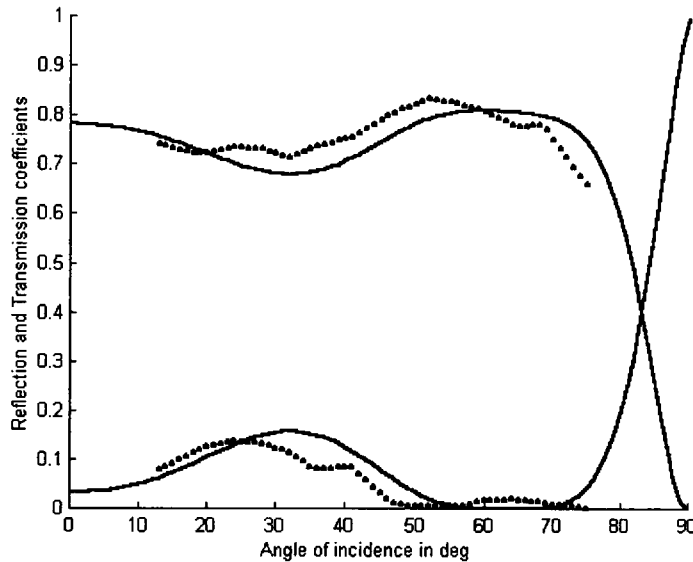
Figure 4-28: Measured and computed reflection and transmission coefficients for a 9 mm
thick Plasterboard using HH polarization for ε_r=3.4 and σ=0.1

Using the RMS technique values of ε_r=3.4 and σ=0.1 have been estimated. The
bootstrap estimates ε_r=3.4±0 with σ=0.0925±0. These values are close to those obtained
from the RMS error one, but different from the ones measured using VV polarisation, see
Table 4-5.

Results give good qualitative agreement with measured values. The estimated
values for the dielectric parameters obtained for the different materials are summarized in
Table 4-7.

The estimated values of the parameters obtained using HH polarisation are
expected to be similar to those found using VV polarization. By fixing ε_r to 2.4 and σ to
0.16, the reflection and transmission coefficients computed for both polarisations are
plotted as shown in Figure 4-29. It can be observed that while the transmissivity using HH
polarisation is higher the reflectivity is lower than that using VV polarisation functions.
Furthermore it can be noticed that the VV polarization has more pronounced peaks and
troughs compared to HH polarisation. In that way due to the flatter behaviour of the
reflectivity and transmissivity functions both techniques loose their sensitivity to detect the
dielectric parameters.

Table 4-7: Dielectric parameters estimated using HH polarization

Materials	RMS Technique ε_r	RMS Technique σ	RMS error	Bootstrap Technique ε_r	Bootstrap Technique σ
Plasterboard 9 mm	3.4	0.1	0.222	3.4	0.0925 ± 0
Plasterboard 13 mm	2.2	0.04	0.047	2.7	0.043 ± 0
Polystyrene 49 mm	1.4	0	0.059	1	0
Fireboard 12.7 mm	3.1	0.11	0.023	3.1	0.002 ± 0
Glass 4.2 mm	6	0.46	0.011	5.31 ± 1.17	$0.3205 \pm 5 \cdot 10^{-2}$
Pattern Glass 3 mm	9.6	0.84	0.028	$9.56 \pm 2 \cdot 10^{-3}$	$0.694 \pm 8 \cdot 10^{-3}$
Concrete Slab 1 inch	6	0.48	0.016	5.28 ± 0.136	$0.3785 \pm 8 \cdot 10^{-3}$
Plywood 5 mm	1.9	0.37	0.017	1.9	0.235 ± 10^{-2}
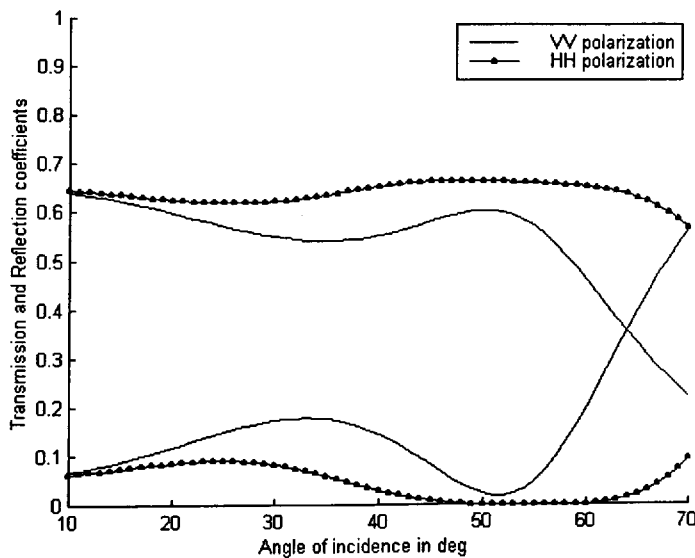
Figure 4-29: Computed coefficients for a 9 mm thick Plasterboard using both VV and HH polarizations with ε_r=2.4 and σ=0.16

In this case, the population of measured points needs to be very accurate in order to estimate the complex permittivity that gives the least RMS error for instance. For this reason the VV polarisation was preferred to characterize materials property as [Shimabukuro, July 1984] who stated: *"From the theoretical model the contrast, the ratio of an adjacent transmission maximum and minimum, increases with the reflectivity and so the use of a perpendicularly polarized wave gives a more accurate measure of the angular position of the transmission peaks and valleys, and thereby that of the real part of the permittivity"*.

4.4 Investigation of the Effect of the General Reflection Coefficient on the Indoor Channel Characteristics using Ray-Tracing

A 2D ray-tracing algorithm [Hammoudeh, August 1995], considering up to second order reflections has been used to investigate the changes of the received signal statistics when the thickness of the walls of the enclosed environment is compared to a wavelength. In this case the general reflection coefficient (4-15) has been used to predict the received signal statistics and results are compared with those calculated under identical conditions but using the well-known Fresnel reflection coefficient.

Simulations have been performed for a long narrow corridor environment as shown in Figure 4-30. The corridor is assumed to be 27.5 m long, 1.6 m wide and 2.7 m high. Both terminals are set in the center line of the corridor at a height of 1.7 m. The transmitter, equipped with an omnidirectional antenna, was placed at 1.5 m away from wall D. The receiver, employed a similar omnidirectional antenna and moved away from the transmitter along the center line of the corridor. The omnidirectional antenna, 6 dBi gain and 8° 3 dB beamwidth in the elevation plane, precluded reflections from ceiling and floor. In this way walls were characterized such as the 9 mm thick plasterboard by ε_r=2.4 and σ=0.16.

wall A

wall B

RX   TX

wall D

wall C
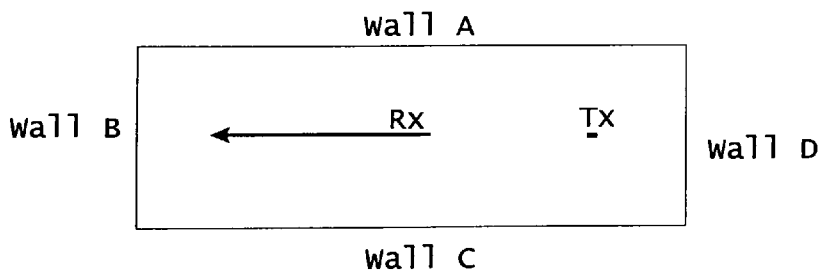
Figure 4-30: Long narrow corridor

The received signal power computed using the Fresnel and the general reflection coefficients are shown in Figure 4-31 a) and b). These envelopes are normalised to their maximum calculated signal level.

It is clearly seen that both envelopes exhibit similar frequency of their amplitude variations. However the depth of fading experienced in both cases is different. The relative amplitude for each ray with respect to the line-of-sight (LOS) has been computed and plotted as a function of distance between terminals. The results obtained by considering the Fresnel and general reflection coefficients are given in Figure 4-32 a) and

b) respectively.
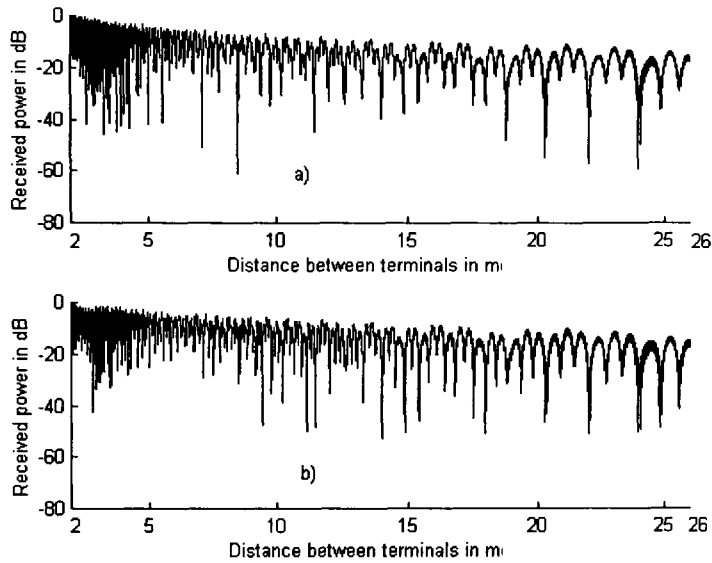
Figure 4-31: Signal envelopes calculated when the receiver moved away from the base station in a long narrow corridor when assuming a) Fresnel and b) general reflection coefficients

It can be seen that, in both cases, the most significant reflections are those from side-walls (wall A and B) and double reflections from opposite side-walls. However the relative amplitudes computed when the thickness of the walls is taken into account are different. In that case, it is also evident that at small distances between terminals the relative amplitudes of double reflected rays off opposite side-walls are not monotonously increasing with distance. This is because of the reflection coefficient computed using the general form has similar behaviour.

In order to quantify the difference in the signal statistics computed by considering both reflection mechanisms, the cumulative distribution function (CDF) of the received signal envelope has been computed and fitted to Rice [Parsons, 1992]. The Rician distribution function is defined as: -

$$P_{Rician}(r) = \frac{r}{b} \cdot e^{\left(-\frac{r_s^2 + r^2}{2 \cdot b}\right)} \cdot I_0\left(\frac{r \cdot r_s}{b}\right) \qquad (4\text{-}37)$$

Where: I_0 is the modified Bessel function of the first kind and zeroth order;

r_s is the LOS peak value, in Watts;

b is the mean received power, in Watts.

The power ratio of the line-of-sight to the total reflected power, K, is given by: -

$$K = \frac{r_s^2}{2 \cdot b}$$

(4-38)

Where: r_s is the LOS peak value in Watts;

b is the mean received power in Watts.
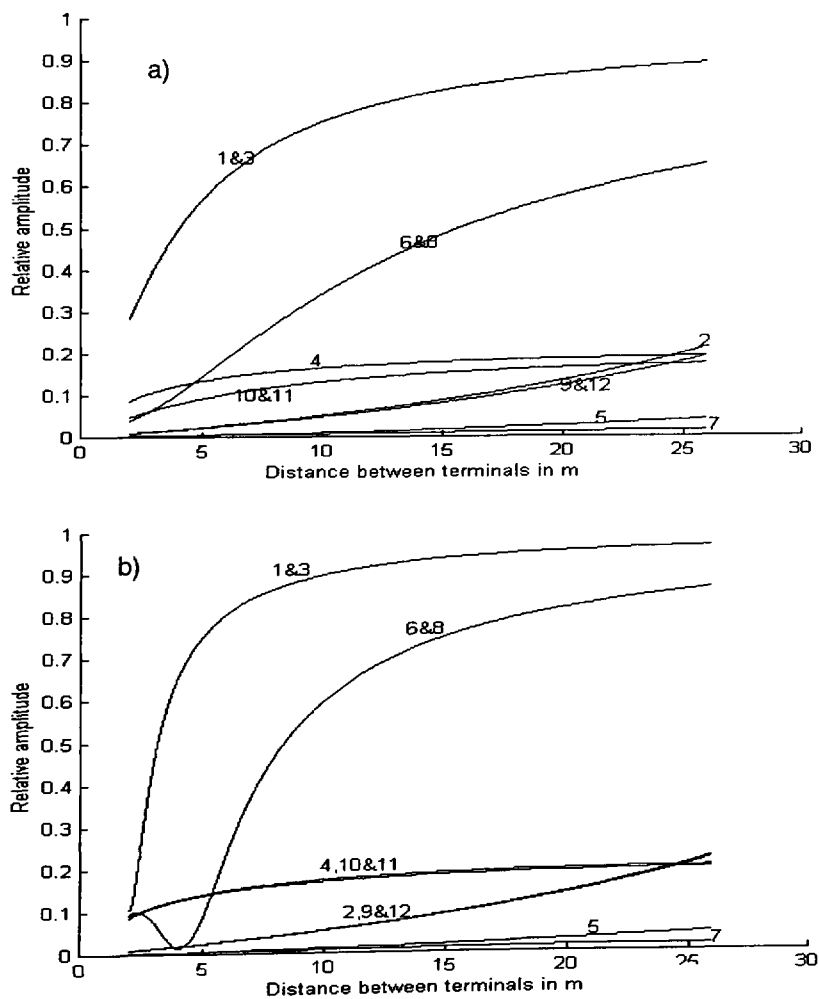
Figure 4-32: Relative amplitudes of reflected rays computed as a function of distance between terminals using the Fresnel reflection coefficient a), using the general reflection coefficient b); 1, 2, 3 and 4 represent single reflections from wall A, B, C and D respectively; 5, 6, 7 and 8 are double reflections from opposite walls BD, CA, DB and AC respectively; 9, 10, 11 and 12 are double reflections from adjacent walls DA, BA, CB and CD respectively
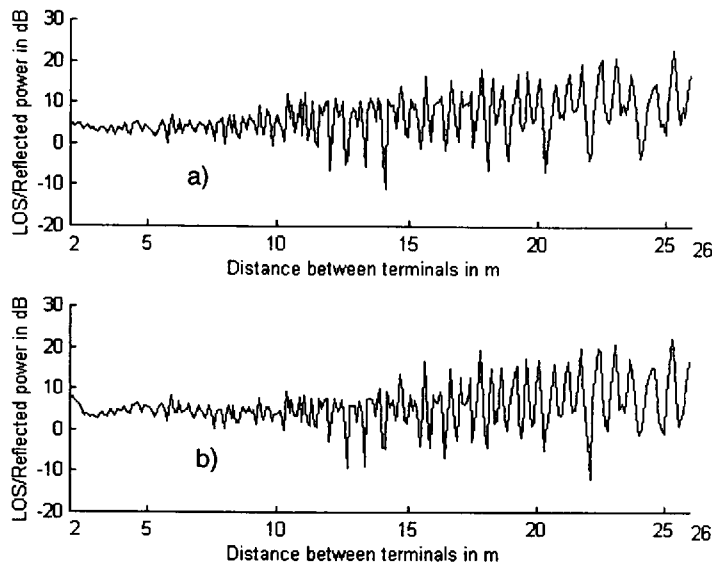
Figure 4-33: Power ratio between LOS and total reflected power computed as a function of distance using a) Fresnel reflection coefficient and using b) general reflection coefficient

The CDF of the received signal has been computed over a window length of 40λ and moved every 20λ. The value of K obtained by finding the best fit is then plotted against the distance between terminals and results are given in Figure 4-33.

It is evident that the power ratio, K, varies in both cases with the average power ratios of 10.085 dB (Fresnel coefficient) and 8.7 dB (general coefficient). This shows that the total reflected power is stronger when the general reflection coefficient is considered.

The moving average of the computed signal envelopes obtained by considering the Fresnel and general reflection coefficients have also been calculated and fitted to a distance power law of the form $k_p d^{-n}$, where k_p is a constant, d is the distance from the base station in metres and n is the propagation exponent. The computed mean signal variation and those calculated assuming both reflection mechanisms are given in Figure 4-34 a) and b) respectively. The exponent computed assuming the Fresnel reflection coefficient is found to be 1.32. This is larger than that computed when the thickness of walls has been considered. The smaller propagation exponent is due to the stronger reflections of the side-walls.
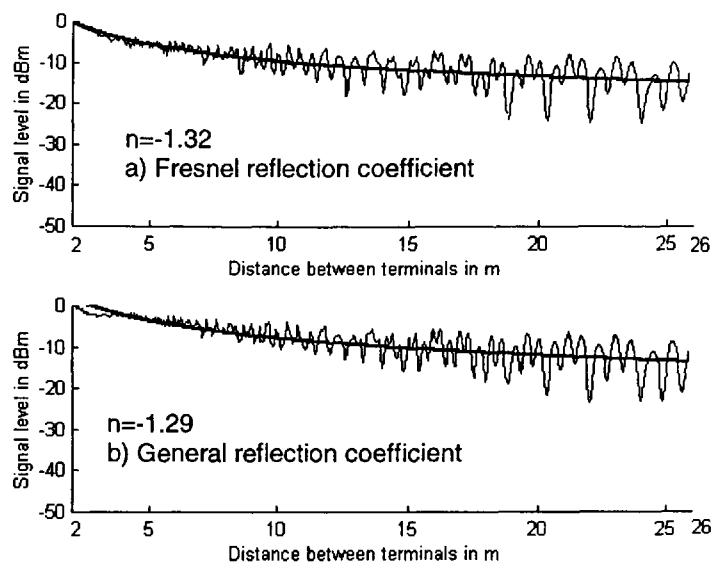
Figure 4-34: Mean signal variation versus distance with $k_p\, d^{-n}$ best fit calculated when a) Fresnel reflection coefficient and b) general reflection coefficient with a thickness of 9 mm were accounted for

4.5 Interim conclusion

Reflectivity and transmissivity measurements have been performed on various building materials using vertical and horizontal polarisations. The reflection and transmission coefficients taking into account the thickness of the material have been developed to help at the interpretation of the measurements. The dielectric parameters of each material have then been estimated by employing the RMS and Bootstrap techniques on the measured and predicted results. A list of the dielectric parameters have been obtained for both polarisations and have been compared to those reported in the literature. It has been established that the two techniques lose their sensitivity for the horizontal polarisation due to the flat reflectivity and transmissivity functions of the materials. Those estimates have therefore been concluded not to be as accurate as those obtained from the vertical polarisation. Estimates obtained from the vertical polarisation have given good qualitative and quantitative agreements with those reported in literature.

The general reflection model has been introduced in a 2D ray-tracing tool accounting for up to second order reflection. Changes in the received signal power have then been observed when the walls of the environement are used to have a specific thickness. It can be concluded that taking into account the thickness of the material in the ray-tracing may increase the total reflected power in the received signal.

5 Measurements and Predictions of Scatter Functions and Depolarisation from Rough Building Surfaces

5.1 Introduction

In the ideal case, reflections off smooth walls are calculated by the Fresnel or general coefficients as described in Chapter 4. However most flat surfaces present irregularities which scatter the electromagnetic waves in all directions. The scattered field is specular, semi-specular or diffuse in nature depending on the degree of surface roughness compared to a wavelength.

This chapter presents measurements and modelling of the scattered field from various rough surfaces at 62.4 GHz. For each material the scatter coefficient is expressed as a function of incident and observation angles. Theoretical modelling based on the Kirchhoff approximation [Beckmann, 1987] is employed to represent the measured functions. Theoretical and experimental results are given here for different polarisations.

5.2 Theoretical Modelling of a Rough Surface

The surface of a material is said to be rough when "the surface will scatter energy of an incident plane wave into various directions, whereas a surface that reflects specularly will be called smooth" [Beckmann, 1987]. The same surface may be considered either rough or smooth depending on the wavelength used. At a given wavelength a surface may be either smooth or rough depending on the angle of incidence.

The study of rough surfaces is classified into two cases. The first is when the roughness is caused by periodical irregularities, whereas the other assumes a random distributed roughness. The latter one is the most typically encountered and is studied in this Chapter.

5.2.1   Scatter from Random Rough Surfaces

The Kirchhoff approximation [Beckmann, 1987] may be used to represent the scattered wave from a random rough surface in terms of the roughness and, incident and observation angles. Hence by representing statistically a random rough surface, a scattering factor of this surface can be deduced. This solution is given here for a two-dimensional rough surface expressed as $\xi(x,y)$ where the incident and scattered electromagnetic waves stay on the same plane, as shown in Figure 5-1.
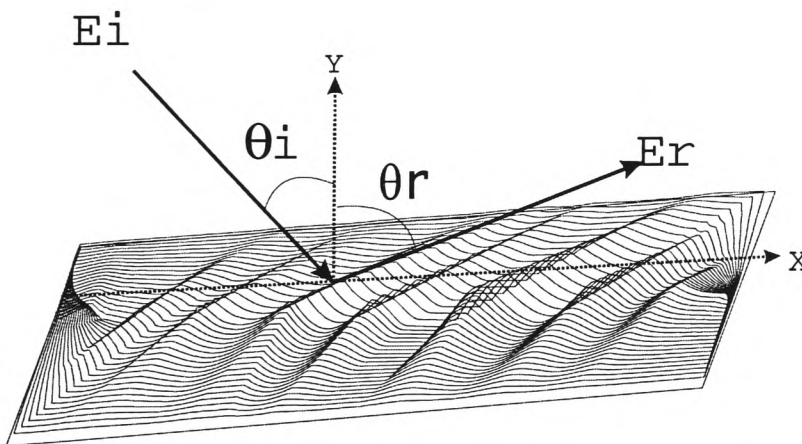
Figure 5-1: Incident electromagnetic wave impinging on a random rough surface $\xi(x,y)$

Random rough surfaces are best described by the statistical distribution of their deviation from a certain mean level. This does not, however, describe the surface completely; this distribution does not indicate whether the peaks and troughs of the surface roughness are crowded close together or whether they are far apart. A second function, the correlation function or autocorrelation coefficient describes this aspect of the surface.

The roughness degree of a surface determines the orientation of the scattered power concentration. Indeed scattered signals may be specular, semi-specular or diffuse

in their nature according to the roughness of a surface as shown in Figure 5-2 a) b) c) respectively. [Beckmann, 1987] states that: *"The total scattered power (scattered into all directions) must be constant and varying T_d (or any other quantity) may redistribute the power scattered into various directions, but must not alter the total power scattered into all directions".*
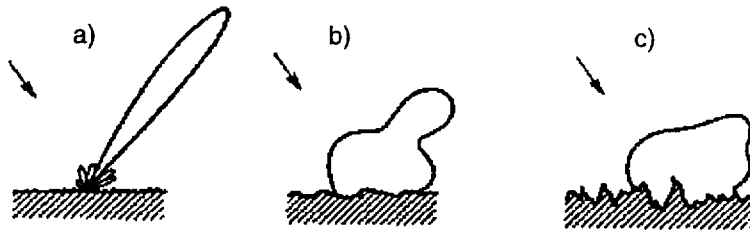
Figure 5-2: Variations of the scattered power according to the roughness directing the scattered field to be either a) specular or b) semi-specular or c) diffuse

A factor g_1 is introduced to help in defining the type of the scattered field and is given by: -

$$g_1 = \left(\frac{2 \cdot \pi \cdot \sigma_h \cdot (\cos\theta_i + \cos\theta_r)}{\lambda} \right)^2 \qquad (5\text{-}1)$$

Where: σ_h is the standard deviation of random surface distribution, in m;

θ_i and θ_r are the incident and observation angles respectively, in rad.

When $g_1 \ll 1$ the scattered field is considered to be specular, and its valu is determined by the general reflection coefficient (4-15). On the other hand when $g_1 \geq 1$, the scatter coefficient is semi-specular. In this case the scatter coefficient is determined from (2-3) and the expression for g_1 reduces to that given in (2-4). The case of $g_1 \gg 1$ as shown in Figure 5-2 c) is treated here.

Here the random rough surface, ζ, is treated to be normally distributed as it is the most important and typical distribution with the mean value equal to zero as in (5-2).

$$\bar{\zeta} = 0 \qquad (5\text{-}2)$$

The standard deviation function, σ_h, can be expressed as: -

$$\sigma_h = \sqrt{\overline{D(\xi)}} \quad \text{(metre)} \qquad (5\text{-}3)$$

With: $\quad D(\xi) = \left(\xi - \overline{\xi}\right)^2 \qquad (5\text{-}4)$

Where: $\overline{D}(\xi)$ is the variance of the random variable.

The autocorrelation function, $C(\tau_d)$, is found to be: -

$$C(\tau_d) = \frac{\overline{\Xi}}{\overline{Y}} = e^{-\frac{\tau_d^2}{T_d^2}} \qquad (5\text{-}5)$$

With: -

$$\Xi = \xi_1 \cdot \xi_2 \qquad (5\text{-}6)$$

$$Y = \xi_1^2 \qquad (5\text{-}7)$$

Where: $\xi_1 = \xi(x_1, y_1)$;

$\xi_2 = \xi(x_2, y_2)$;

(x_1, y_1) and (x_2, y_2) are 2 different points on the surface, ξ, spaced by a distance τ_d;

T_d is the correlation distance, in metres.

σ_h represents then the degree of roughness of a surface while T_d expresses the density of irregularities on the surface. When $T_d = 0$ means that the surface is discontinuous all over its area. When T_d tends towards 0 it means that the surface is very densely packed of irregularities. Large T_d means that the surface is made of gently rolling irregularities.

The Kirchhoff approximation has been derived assuming certain hypothesis and its accuracy depends on the following conditions: -

$$T_d \gg \lambda \qquad (5\text{-}8)$$

$$T_d \ll L \qquad (5\text{-}9)$$

$$T_d^2 << A \tag{5-10}$$

Where: λ is the wavelength, in metres;

L represents the length of the random rough surface, in metres;

A expresses the cross illumination area between the transmitter and the receiver, in square metres.

The condition (5-7) means that the Kirchhoff approximation will be accurate if the radii of curvature of the irregularities are large compared to the wavelength considered, therefore in this study T_d must be much larger than 4.808 mm. Furthermore Kirchhoff approximation will break down totally for T_d tending towards 0.

For a very rough surface the scattering factor, ρ_s, obtained using the Kirchhoff approximation is given by: -

$$|\rho_s| = \sqrt{\frac{\pi \cdot F^2 \cdot T_d^2}{A \cdot V_z^2 \cdot \sigma_h^2} \cdot e^{\left(-\frac{V_x^2 \cdot T_d^2}{4 \cdot V_z^2 \cdot \sigma_h^2}\right)}} \tag{5-11}$$

With: -

$$V_x = \frac{2 \cdot \pi}{\lambda} \cdot \left(\cos\theta_i - \cos\theta_r\right) \tag{5-12}$$

$$V_z = \frac{2 \cdot \pi}{\lambda} \cdot \left(\cos\theta_i + \cos\theta_r\right) \tag{5-13}$$

$$F = \frac{1 + \cos\left(\theta_i + \theta_r\right)}{\cos\theta_i \cdot \left(\cos\theta_i + \cos\theta_r\right)} \tag{5-14}$$

Where: T_d is the correlation distance, in metres;

σ_h is the standard deviation of the roughness, in metres;

A is the area of intersection, in square metres;

θ_i is the incident angle, in radians;

θ_r the observation angle, in radians.

The scattered power, P_s, is thus defined by: -

$$P_s = \left\| \rho_s \right| \cdot \Gamma_g \right|^2 \cdot P_i \quad \text{(Watt)} \tag{5-15}$$

Where: ρ_s is the scattering factor;

Γ_g is the general reflection coefficient;

P_i is the incident power, in Watts.

5.3 Random Rough Surfaces

Three types of concrete slabs (90 cm long by 70 cm wide) with different random rough surfaces have been manufactured in the School of Built Environment at the University of Glamorgan. This was achieved by impregnating the concrete slabs with either 10, 20 or 40 mm angular stones as shown in Figure 5-3, Figure 5-4 and Figure 5-5 respectively. Five slabs have been manufactured for each roughness.
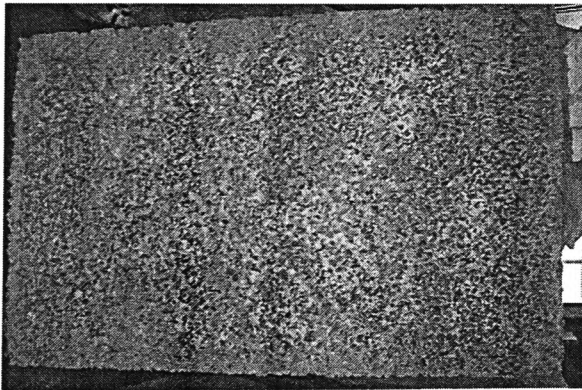
Figure 5-3: Concrete slab impregnated with 10 mm angular stones
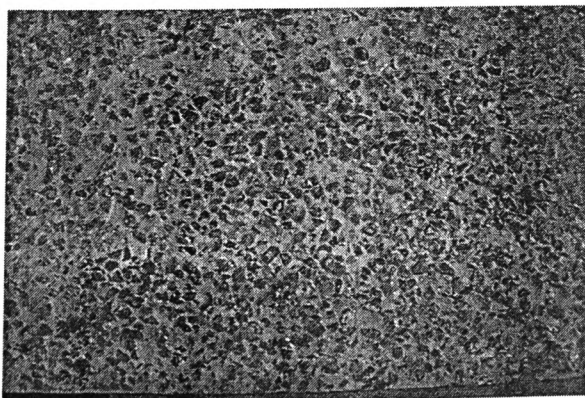
Figure 5-4: Concrete slab impregnated with 20 mm angular stones
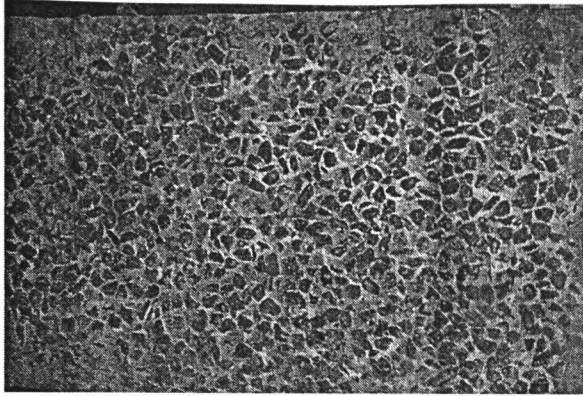
Figure 5-5: Concrete slab impregnated with 40 mm angular stones

In addition outdoor measurements have been made on two building façades. One surface is made of big stones while the other is pebble-dash as is given in Figure 3-17 and Figure 3-18 respectively.

5.4 Parameters Characterisation of Rough Surfaces

The values of the standard deviation of the randomly distributed rough surfaces used in this study, and their correlation distances have been established to use in the theoretical model. A photographic technique was devised and used by colleagues in the School of Built Environment. The method is based on photographing the cross section of each concrete slab, whereas for the façades photographs on their corner-line were made.

The photographs taken show the cut surface, with an identifying ruler, a shadow-cast upper surface, and the scribed reference bar as shown in Figure 5-6. The latter is made of horizontal and vertical lines, accurately marked, providing a rectangular grid, measuring 20 mm and 10 mm respectively. Numerous 50 mm long sections of the slices were photographed and then measured. Afterwards photographs were placed onto a X-Y sliding bed of a Nikon V-16c profile projector. In this manner, photographs have been magnified so that accuracy up to 1 micron (10^{-6} metre) has been reached.

The data for each set of concrete slabs has been processed to calculate the standard deviation, σ_h, and the correlation distance, T_d, of the randomly distributed rough surface. Those factors defining the roughness are listed in Table 5-1.
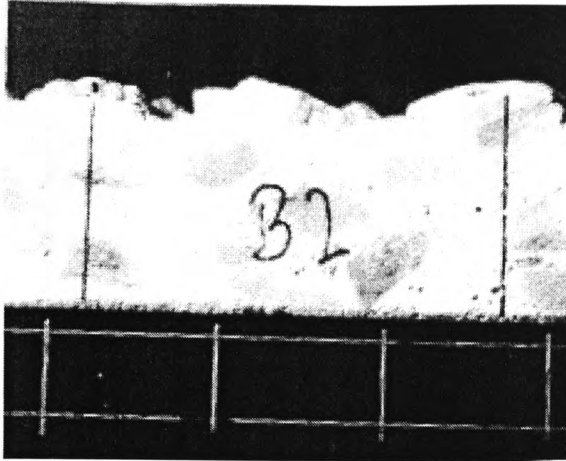
Figure 5-6: Photograph of the material cross section together with the reference scale

Figure 5-7 shows, for instance, the cumulative distribution function for the roughness values measured for the 10 mm concrete slab together with the theoretical normal distribution function. It can be clearly seen that the roughness is normally distributed. This has been repeated for all the different surfaces considered and similar conclusions have been reached.

Table 5-1: Measured parameters according to various random rough surfaces

Rough Surfaces	10 mm	20 mm	40 mm	Pebble-dash	Stone
$\overline{T}_d$ in mm	3.628	4.544	5.251	2.58	11.67
$\overline{\sigma}_h$ in mm	1.586	1.709	2.846	0.45	1.44
Average of $\left(\dfrac{T_d}{\sigma_h}\right)$	2.301±0.48	2.713±1.05	2.264±1.35	6.47±2.24	8.66±3.4

It can be noted from Table 5-1 that even though the stone size of the concrete slabs varies from 10 to 40 mm the measured standard deviation values do not vary accordingly and remain well below the stone size. In addition the $\dfrac{T_d}{\sigma_h}$ ratio used in equation (5-10) to calculate the predicted scatter coefficient does not uniquely describe each type of roughness due to the large possible variation in its value.
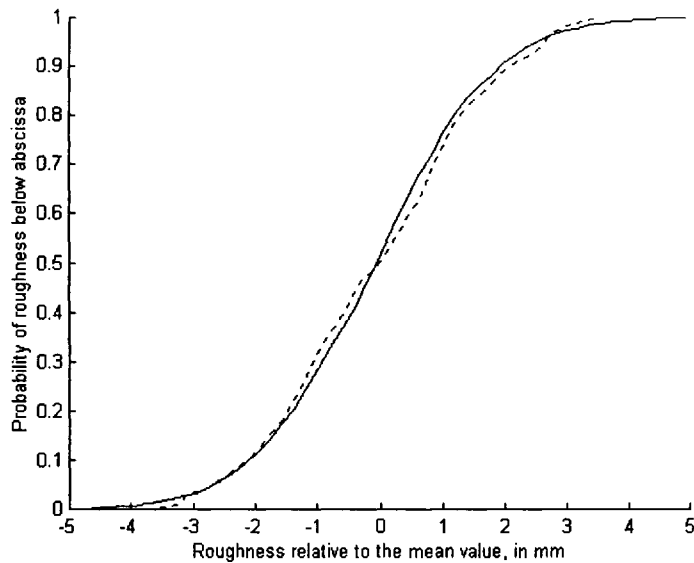
Figure 5-7: Cumulative distribution function measured for the 10 mm concrete slab together with the theoretical normal distribution

5.5 Measurements and Predictions of scatter coefficients

This section presents experimental results using various rough surfaces and different polarisations together with theoretical predictions obtained using the Kirchhoff approximation. Depolarisation due to random roughness has also been investigated Furthermore the dependence of the signal level on the surface roughness is also examined.

5.5.1 Vertical Polarisation Scatter Results

The scatter coefficient from the concrete slabs has been measured inside the anechoic chamber as described in Chapter 3. Because the scatter field is random ten measurements were made for each type of roughness. The scatter coefficient has been computed by normalising the scatter field to the level reflected from a metal sheet obtained under identical conditions. Results presented here are the average of ten measurements and expressed as a function of incident and observation angles.

Outdoor measurements were conducted as described in Chapter 3 and the scatter coefficient was measured by normalising the scatter field with respect to the free space

loss. A free space loss calibrated curve was measured inside the anechoic chamber as described in Chapter 3.

Figure 5-8, Figure 5-9 and Figure 5-10 show the theoretical and experimental results for the 10, 20 and 40 mm angular stones concrete slabs respectively. It is noted from those figures that no specular components are visible and therefore the scattered field is of diffused nature. Large variations between measurements and simulations can be observed. This may be explained by the fact that the condition (5-7), required for the Kirchhoff approximation accuracy, is not met, and the Kirchhoff approximation breaks down completely.
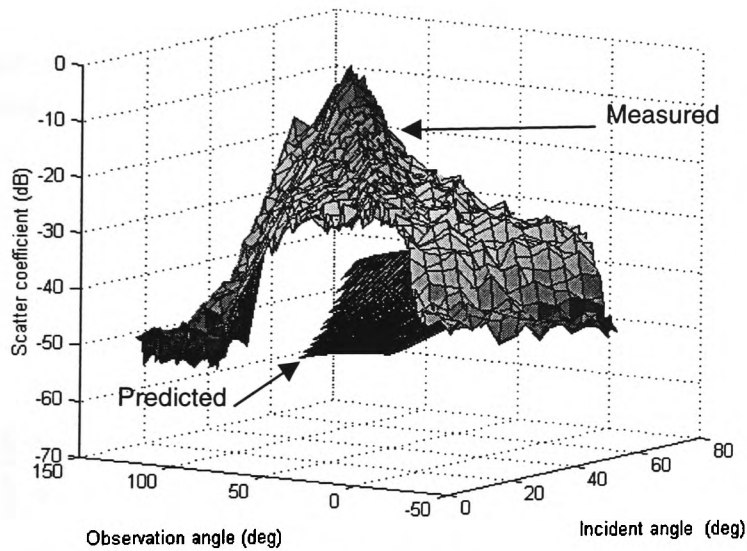
Figure 5-8: Measured and predicted scatter coefficients for the concrete slab with 10 mm stones
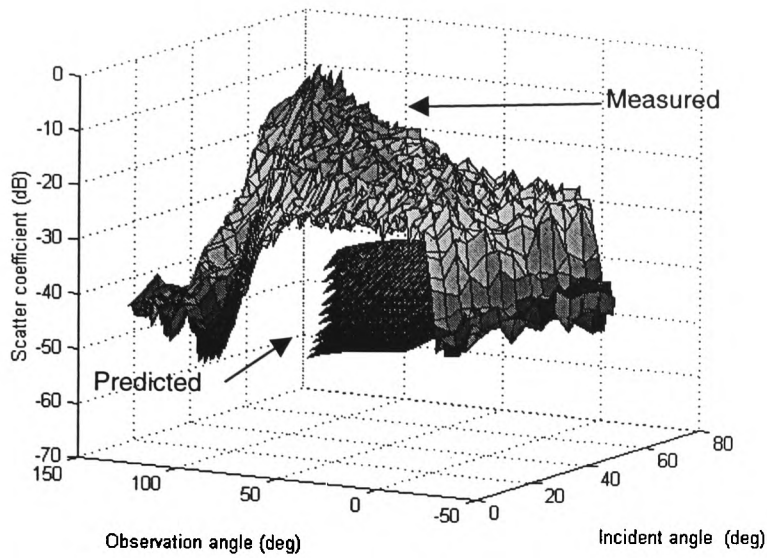
Figure 5-9: Measured and predicted scatter coefficients for the concrete slab with 20 mm stones
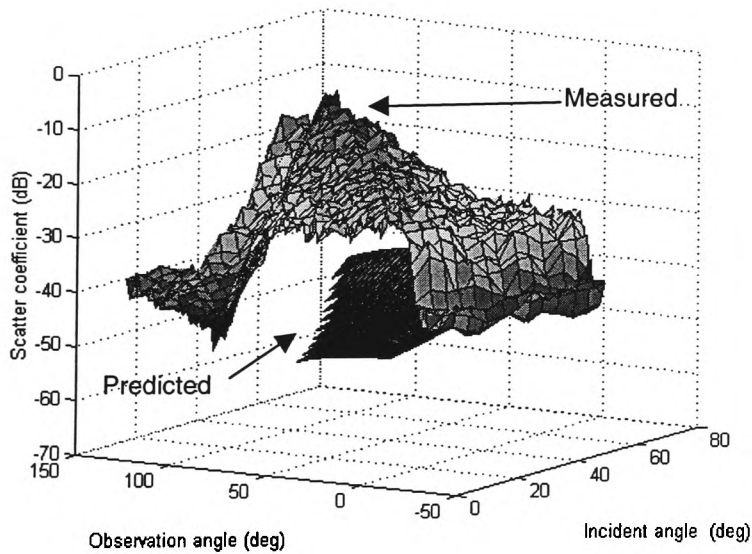
Figure 5-10: Measured and predicted scatter coefficients for the concrete slab with 40 mm stones

The scatter coefficient measured for both building façades are given in Figure 5-11 and Figure 5-12. Even though T_d is greater than twice the wavelength for the big stone façade, the model still fails to represent the measured signal level.
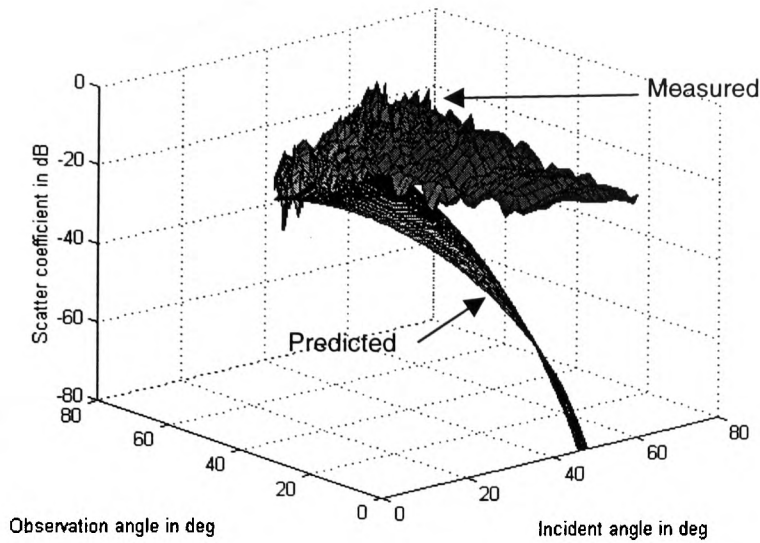
Figure 5-11: Measured and predicted scatter coefficients for the façade with big stones
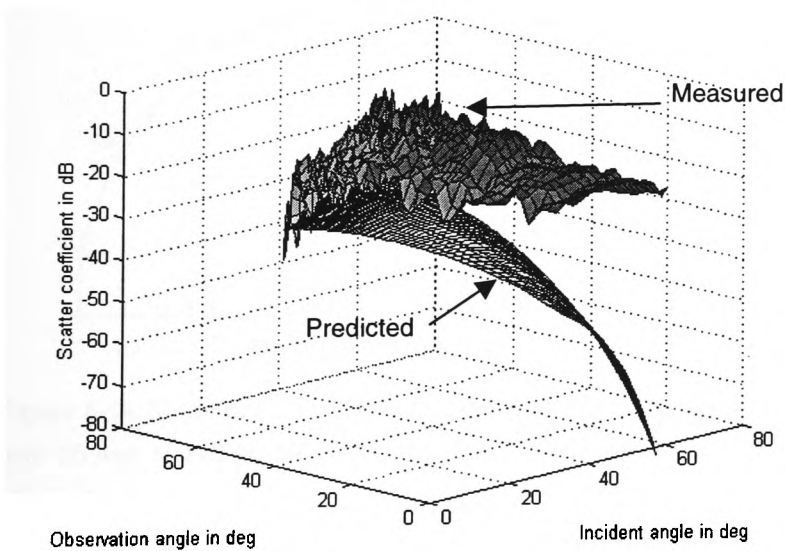
Figure 5-12: Measured and predicted scatter coefficients for the pebble-dash surface

The discrepancies between the measured and predicted levels for the concrete slabs have been investigated further as shown in Figure 5-13, Figure 5-14 and Figure 5-15. For each slab predictions were made using the mean, maximum, and minimum possible values for the $\frac{T_d}{\sigma_h}$ ratio as given in Table 5-1.
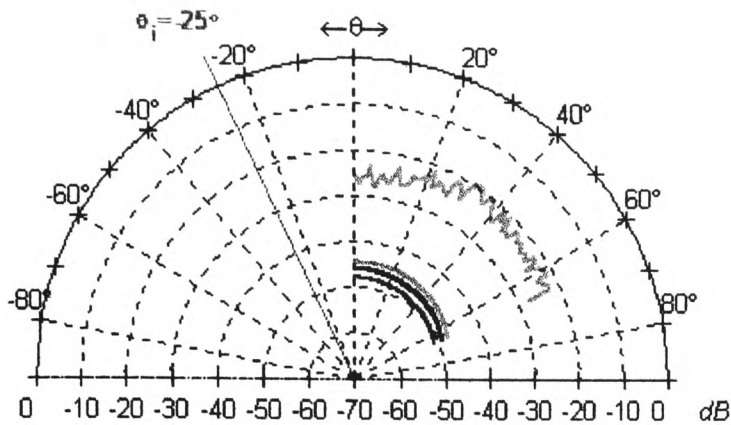
Figure 5-13: Measured, in green, and predicted scatter coefficients for the concrete slab with 10 mm stones at 25° incident angle. Color code used for the prediction: red - $\frac{T_d}{\sigma_h} = 1.821$, magenta - $\frac{T_d}{\sigma_h} = 2.781$ and black - $\frac{T_d}{\sigma_h} = 2.301$.
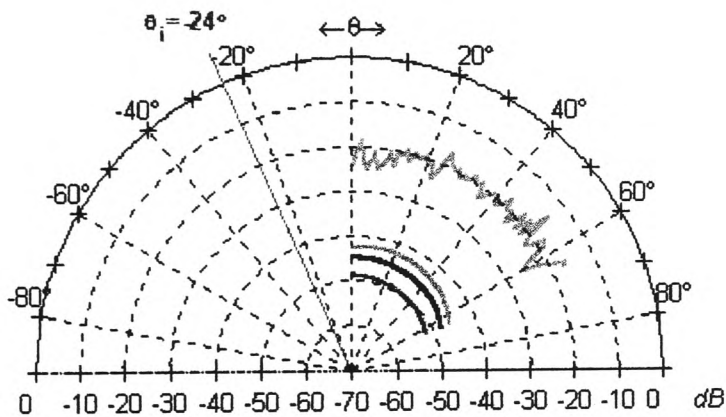
Figure 5-14: Measured, in green, and predicted scatter coefficients for the concrete slab with 20 mm stones at 24° incident angle. . Color code used for the prediction: red - $\frac{T_d}{\sigma_h} = 1.663$, magenta - $\frac{T_d}{\sigma_h} = 3.763$ and black - $\frac{T_d}{\sigma_h} = 2.713$.

It can be observed that the theoretical scatter coefficients are about 20 dB below measured level.
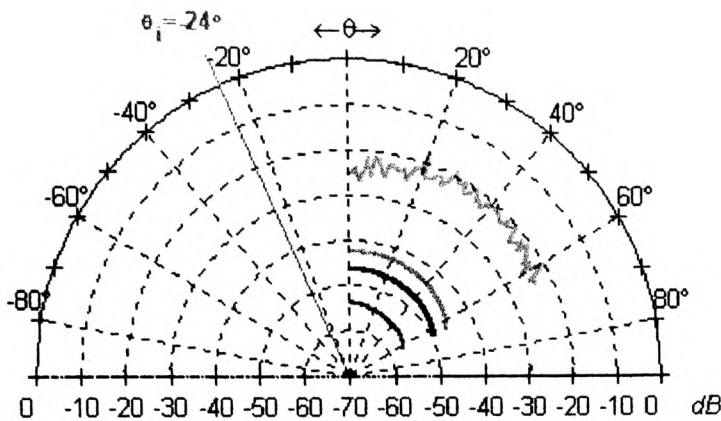
Figure 5-15: Measured, in green, and predicted scatter coefficients for the concrete slab with 40 mm stones at 24° incident angle. Color code used for the prediction: red - $\frac{T_d}{\sigma_h} = 0.914$, magenta - $\frac{T_d}{\sigma_h} = 3.614$ and black - $\frac{T_d}{\sigma_h} = 2.264$.

5.5.2 Horizontal Polarisation Scatter Results

Measurements on the concrete slabs have been repeated under identical conditions inside the anechoic chamber but for horizontal polarisation. Results presented here are the average over two measurements.

Figure 5-16 shows theoretical and experimental scatter coefficients of the 40 mm rough slab. It is clearly seen that the model coefficient level is lower than the measured results. This is better shown in Figure 5-17 where the scatter coefficients have been plotted for 25° incident angle taking into account the maximum and minimum possible values of $\frac{T_d}{\sigma_h}$. Despite of that, large discrepancies between computed and measured results still exist.

It can be concluded that the model fails to represent the measurements even when the correlation distance is larger than the wavelength.
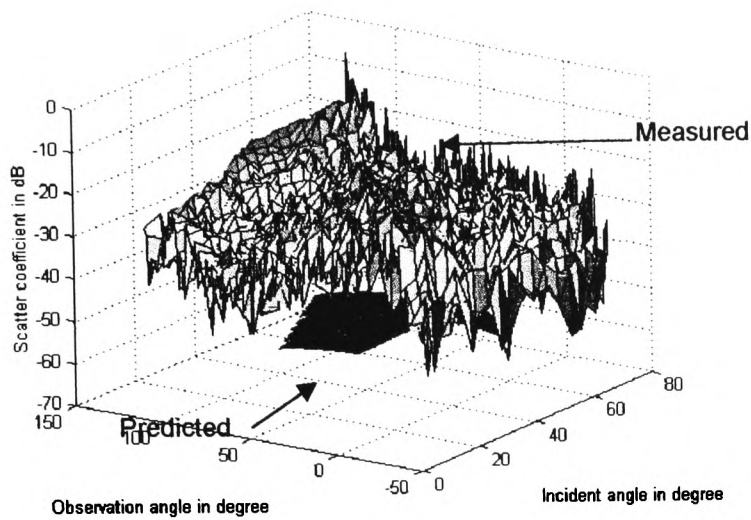
Figure 5-16: Measured and predicted scatter coefficients for the concrete slab with 40 mm stones
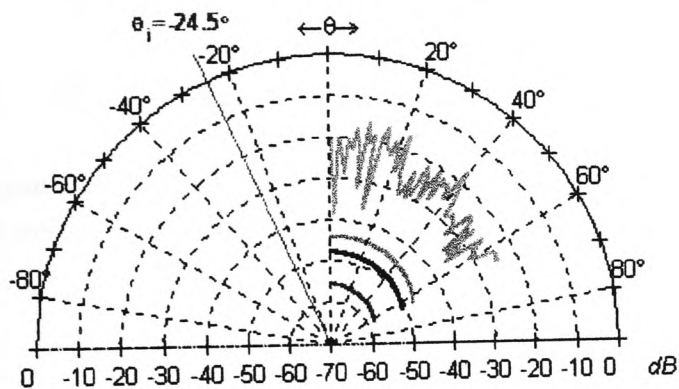
Figure 5-17: Measured, in green, and predicted scatter coefficients for the concrete slab with 40 mm stones at 24.5° incident angle. Color code used for the prediction: red - $\frac{T_d}{\sigma_h} = 0.914$, magenta - $\frac{T_d}{\sigma_h} = 3.614$ and black - $\frac{T_d}{\sigma_h} = 2.264$.

5.5.3 Dependence of the Scatter Coefficient on the Roughness

The dependence of the scattered signal level on the surface roughness has been examined by plotting the measured scatter coefficient as a function of the observation angle at a given angle of incidence.

Figure 5-18 and Figure 5-19 show the mean scattered coefficients for the concrete slabs with 10, 20 and 40 mm stones at two different angles of incidence. These results show that the mean scatter coefficients do not exhibit a peak at and around the incident angle.
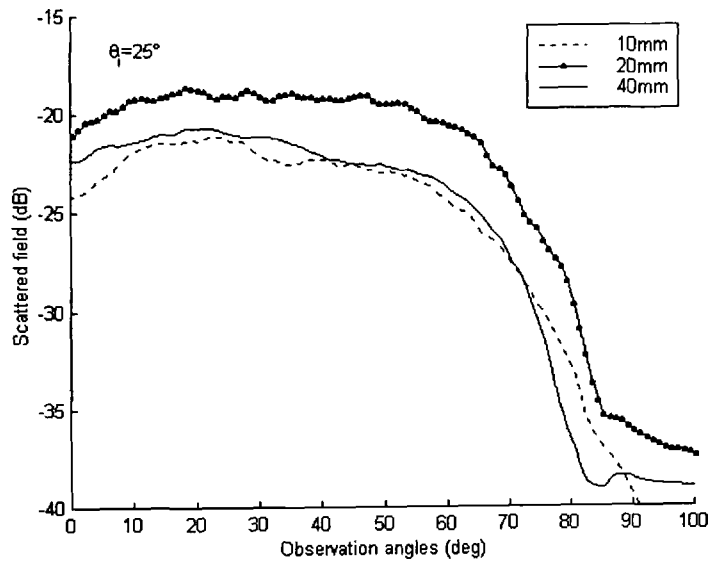
Figure 5-18: Measured mean scatter coefficients for the concrete slabs with 10, 20 and 40 mm stones at 25° incident angle
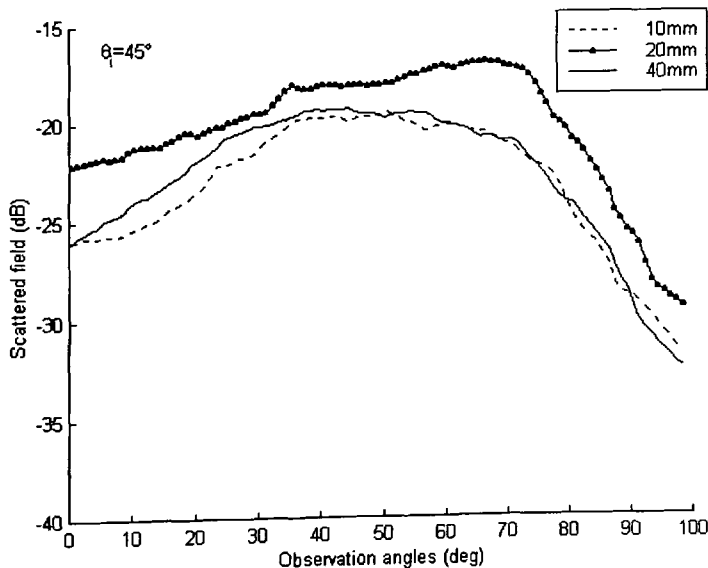
Figure 5-19: Measured mean scatter coefficients for the concrete slabs with 10, 20 and 40 mm stones at 45° incident angle

The levels of the scatter coefficients appear to follow the values obtained from the ratio $\dfrac{T_d}{\sigma_h}$ with the highest scatter level measured for the 20 mm slab which found to be

have the largest $\dfrac{T_d}{\sigma_h}$ ratio. It can be noted that the scatter levels obtained from both the

10 and 40 mm slabs are almost similar although the value of σ_h measured for the 40 mm slab is 2.85 mm compared to σ_h=1.59 mm for the 10 mm slab.

It has also been found that the dependence of the scatter level on the surface roughness of the concrete slabs using HH polarisation exhibit similar behaviours. Results obtained at 25° incident angle are shown in figure 5-20.
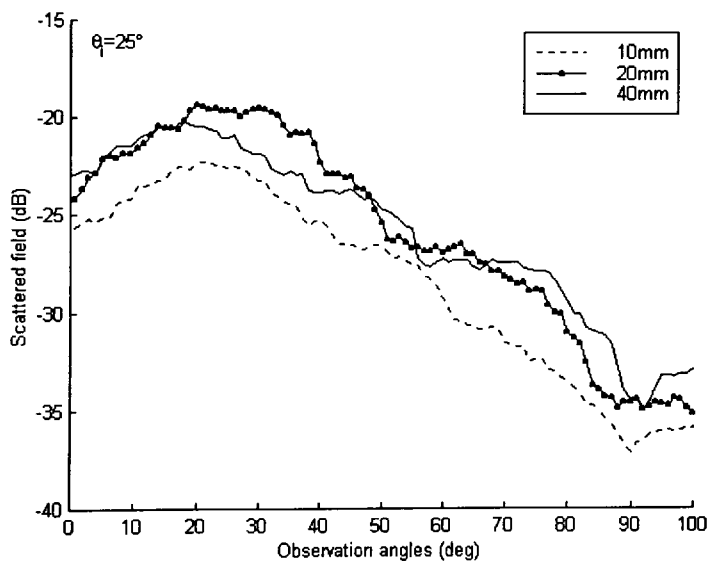
Figure 5-20: Measured mean scatter coefficients for the concrete slabs with 10, 20 and 40 mm stones at 25° incident angle

Outside the specular range, the scatter level does not exhibit any clear correlation with the parameters describing the rough surface. This general behaviour may be due to the fact that these parameters are not adequate to uniquely describe the types of roughness constructed.

As has been described the Kirchhoff approximation fails to represent the scatter field. It has to be pointed that this theoretical model does not take into account depolarisation. It has therefore been decided to conduct depolarisation measurements as outlined in the next section.

5.5.4 Cross-Polarisations Measurements on the Concrete Slabs

Cross-polarisation measurements have been made on the concrete slabs to quantify the amount of depolarisation due to rough surfaces. The changes in the received signal polarisation could only be visible when 90° depolarisation is made, i.e. a vertically polarised incident wave becoming horizontally polarised after reflection or vice-versa. In free space, the cross-polarisation discrimination averaged over the 3 dB beamwidth is 28 dB as shown in Figure 5-21. The free space level was obtained by measuring the reflected signal from a flat metal sheet placed on the top of the rough surface.
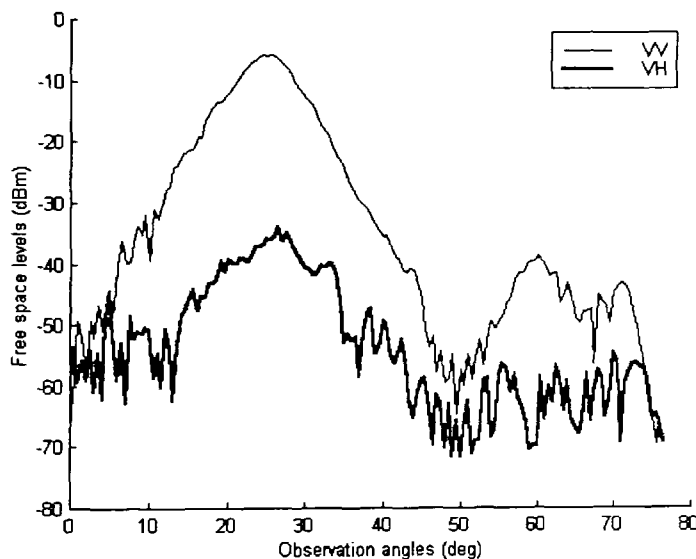
Figure 5-21: Free space measurements for VV and VH polarisations at 25° angle of incidence

The cross-polarisation discrimination has been calculated for various incident angles and compared to the one obtained from free space measurements. Comparisons between the two cross-polarisation discriminations give then the amount of signal depolarised due to the rough surface. The cross-polarisation discrimination has been calculated such that for each angle of incidence, values inside the 3 dB beamwidth have been averaged.

Figure 5-22, Figure 5-23 and Figure 5-24 show the vertical-vertical (VV) and the vertical-horizontal (VH) polarised scattered fields at 25° angle of incidence for the concrete slabs with 10, 20 and 40 mm stones respectively. The cross-polarisation

discrimination values have been measured from these graphs and compared with results obtained from free space measurements.
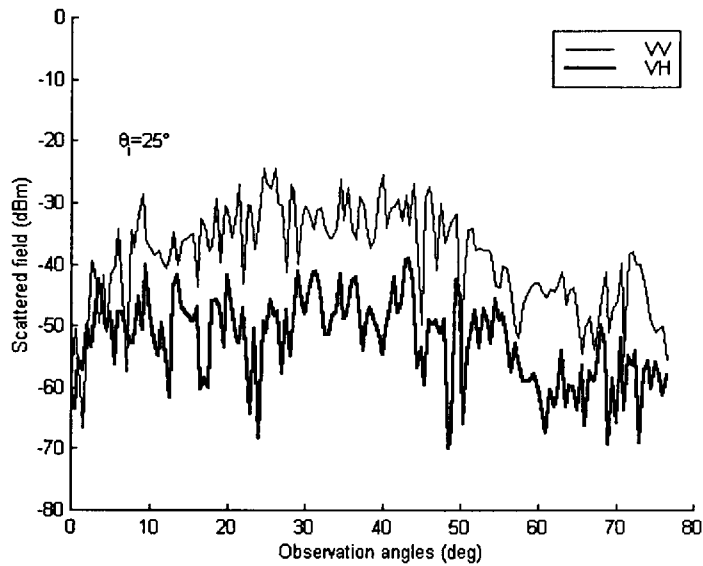
Figure 5-22: Measured scattered field for the concrete slab with 10 mm stones for both VV and VH polarisations
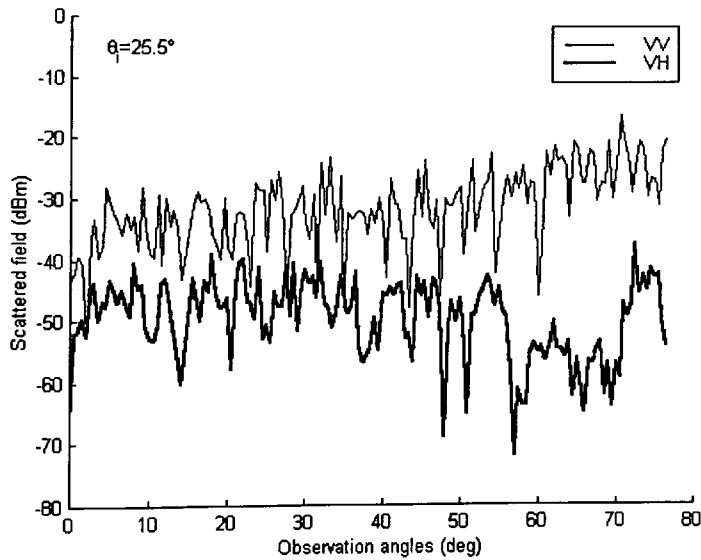
Figure 5-23: Measured scattered fields for the concrete slab with 20 mm stones for both VV and VH polarisations
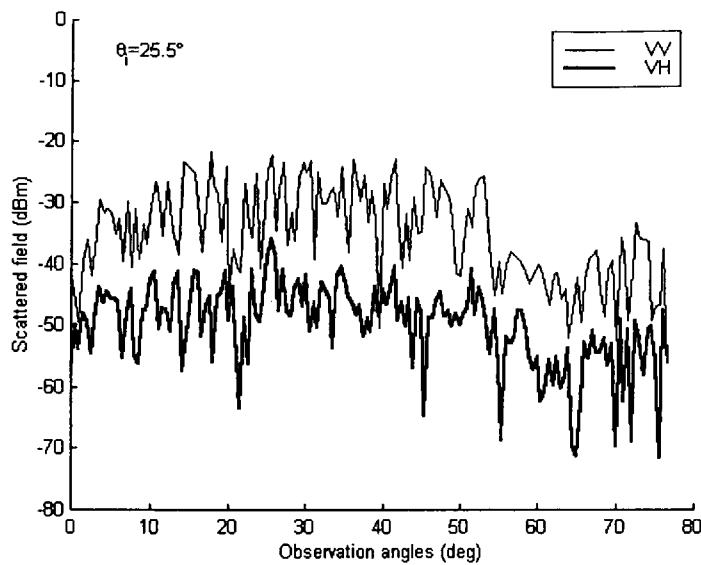
Figure 5-24: Measured scattered field for the concrete slab with 40 mm stones for both VV and VH polarisations

Table 5-2, Table 5-3 and Table 5-4 show the results obtained for the various angles of incidence. Those results clearly show that the surface roughness caused the cross-polarisation signal level to increase on average by about 11.5, 13.7 and 13.7 dB for the concrete slabs with 10, 20 and 40 mm stones respectively. There is no clear correlation between these values and parameters characterising the concrete slabs. Both slabs with 20 and 40 mm stones have shown almost similar depolarisation level although of their roughness is 1.709 and 2.846 mm respectively. These results are in line with those discussed in section 5.5.3 where no relationship between roughness and the scattered level is evident.

Table 5-2: VV and VH cross-polarisation discrimination obtained for the concrete slab with 10 mm stones

	Angle of incidence in degree			
	$\theta_i=18.5°$	$\theta_i=25°$	$\theta_i=33°$	$\theta_i=45°$
Cross-polarisation discrimination for free space measurements	28.87dB	29.80dB	29.21dB	29.05dB
Cross-polarisation discrimination for scattered field measurements	17.32dB	19.24dB	17.38dB	17.08dB
Amount depolarised	11.55dB	10.56dB	11.83dB	11.97dB

Table 5-3: VV and VH cross-polarisation discrimination obtained for the concrete slab with 20 mm stones

	Angle of incidence in degree			
	θ_i=18.5°	θ_i=25°	θ_i=33°	θ_i=45°
Cross-polarisation discrimination for free space measurements	28.27dB	28.88dB	28.92dB	28.61dB
Cross-polarisation discrimination for scattered field measurements	14.88dB	14.51dB	15.23dB	15.29dB
Amount depolarised	13.40dB	14.37dB	13.69dB	13.32dB

Table 5-4: VV and VH cross-polarisation discrimination obtained for the concrete slab with 40 mm stones

	Angle of incidence in degree			
	θ_i=18.5°	θ_i=25°	θ_i=33°	θ_i=45°
Cross-polarisation discrimination for free space measurements	28.27dB	28.88dB	28.92dB	28.61dB
Cross-polarisation discrimination for scattered field measurements	15.27dB	14.55dB	13.37dB	16.64dB
Amount depolarised	13.00dB	14.33dB	15.55dB	11.97dB

In a same way depolarisation of a horizontally polarised incident wave into vertical polarisation has been investigated. Figure 5-25 shows horizontal-horizontal (HH) and horizontal-vertical (HV) polarised scattered fields measured at 25° angle of incidence for the concrete slab with 10 mm stones. Cross-polarisation discrimination values are given in Table 5-5, Table 5-6 and Table 5-7 for the three rough slabs.

These HH and HV results show no clear dependence between the amount of depolarisation and the parameters characterising the concrete slabs. On average the concrete slabs with 10, 20 and 40 mm stones produce a cross-polarisation scatter level of 13.8, 14.6 and 12.7 dB above that obtained in free space. It is also worth noting that although the VH cross-polarisation discrimination level measured for the slabs with 10 mm stones is higher than that obtained for the HV polarisation, the cross-polarisation discrimination values for others slabs vary in a non deterministic manner.
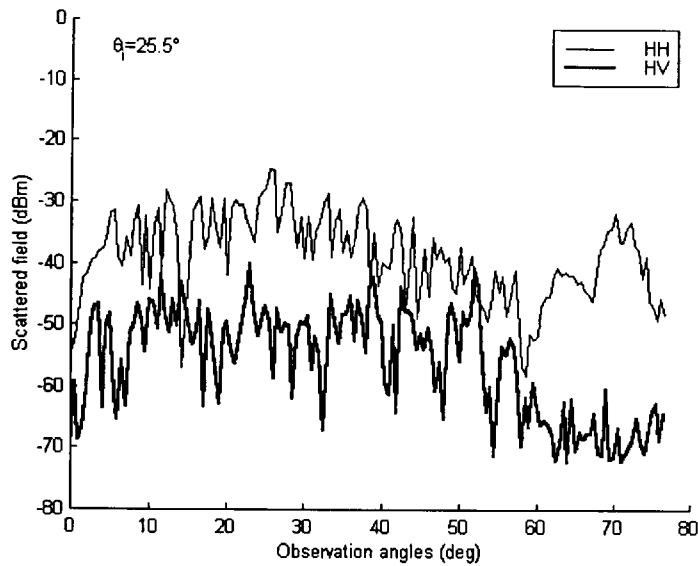
Figure 5-25: Measured scattered field for the concrete slab with 10 mm stones for both HH and HV polarisations

Table 5-5: HH and HV cross-polarisation discrimination obtained for the concrete slab with 10mm stones

	Angle of incidence in degree			
	θ_i=18.5°	θ_i=25°	θ_i=33°	θ_i=45°
Cross-polarisation discrimination for free space measurements	30.32dB	30.44dB	29.27dB	29.50dB
Cross-polarisation discrimination for scattered field measurements	19.69dB	17.93dB	14.05dB	12.63dB
Amount depolarised	10.64dB	12.51dB	15.22dB	16.87dB

Table 5-6: HH and HV cross-polarisation discrimination obtained for the concrete slab with 20 mm stones

	Angle of incidence in degree			
	θ_i=18.5°	θ_i=25°	θ_i=33°	θ_i=45°
Cross-polarisation discrimination for free space measurements	30.32dB	30.44dB	29.27dB	29.50dB
Cross-polarisation discrimination for scattered field measurements	17.31dB	15.38dB	14.61dB	14.02dB
Amount depolarised	13.01dB	15.06dB	14.66dB	15.48dB

Table 5-7: HH and HV cross-polarisation discrimination obtained for the concrete slab with 40 mm stones

	Angle of incidence in degree			
	θ_i=18.5°	θ_i=25°	θ_i=33°	θ_i=45°
Cross-polarisation discrimination for free space measurements	27.14dB	27.49dB	27.99dB	26.64dB
Cross-polarisation discrimination for scattered field measurements	13.24dB	16.55dB	15.55dB	12.97dB
Amount depolarised	13.90dB	10.94dB	12.44dB	13.67dB

5.6 Characterisation of the Semi-Specular Reflection

The surfaces of the concrete slabs with 10 and 40 mm stones have been modified by introducing a 10 cm wide smooth concrete surface in the centre of the concrete slabs as shown in Figure 5-26 and Figure 5-27. Measurements on these surfaces have been made inside the anechoic chamber under identical conditions to these for the rough slabs.

The intersection of the illuminated areas made by the transmit and the receive antennas is dependent on the incident angle. At each incident angle the intersection area has been computed and the percentage of the surface roughness within this area is obtained. The larger the angle of incidence, the larger the percentage of roughness within the intersection area. In this way the dependence of the signal level on the percentage of roughness relative to the total area can be observed.
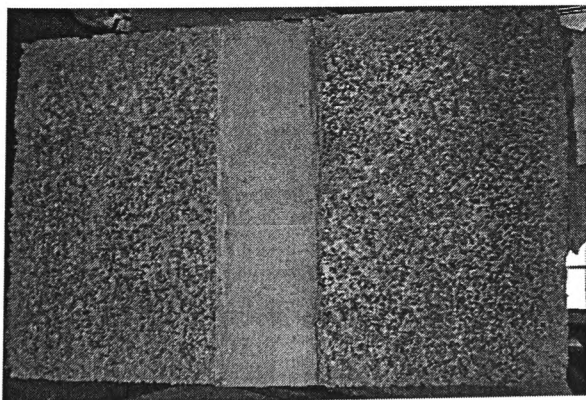
Figure 5-26: 10 mm concrete slab with 10 cm wide concrete stripe
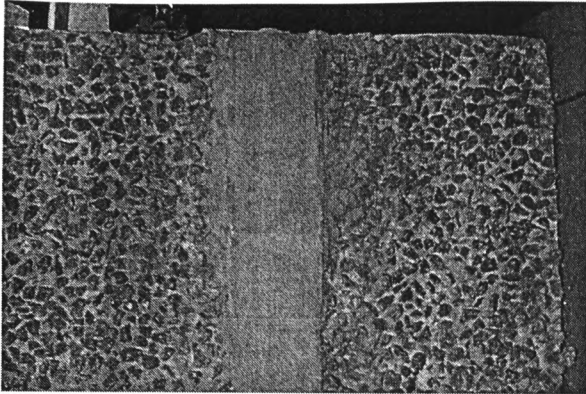
Figure 5-27: 40 mm concrete slab with 10 cm wide concrete stripe

5.6.1 Co-Polarisations Reflection Measurements

Figure 5-28 and Figure 5-29 show the vertical polarisation measured scatter coefficients as a function of the incident and observation angles for the concrete slabs with 10 and 40 mm stones and smooth stripe respectively.
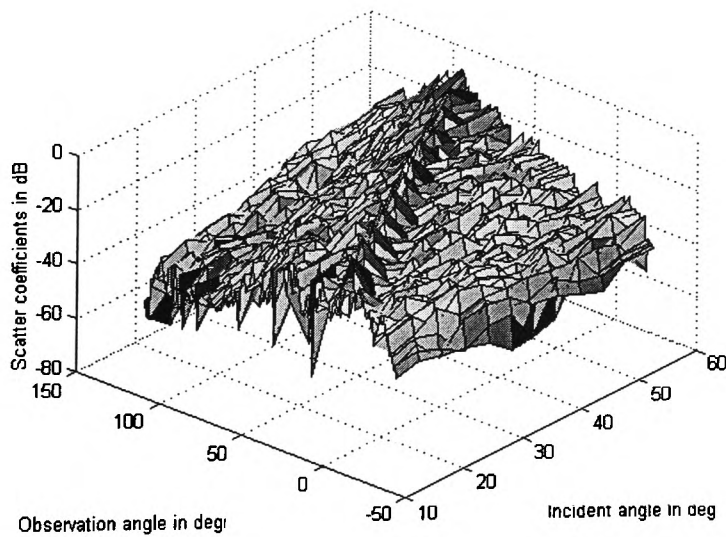
Figure 5-28: Measured scatter coefficient for the concrete slab with 10 mm stones and smooth stripe as function of incident and observation angles
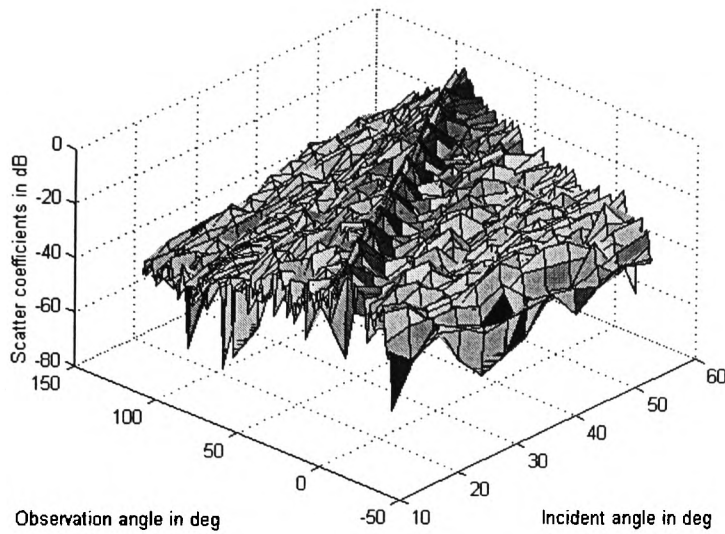
Figure 5-29: Measured scatter coefficient for the concrete slab with 40 mm stones and smooth stripe as function of incident and observation angles

The percentage of roughness computed within the intersection area of the two antennas is given in Figure 5-30. The percentage of roughness increases with the angle of incidence to a maximum value occurring at 60°. It is therefore expected that the peak values, occurring in the specular direction, as shown in Figure 5-28 and Figure 5-29, decrease in amplitude as the angle of incidence increases.
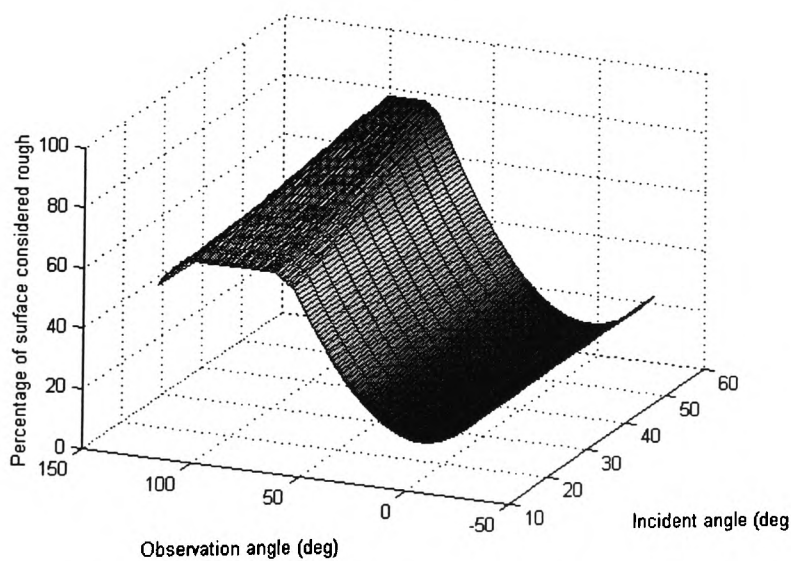
Figure 5-30: Percentage of surface roughness within the intersection area as a function of incident and observation angles

Figure 5-31 and Figure 5-32 show the maximum measured values in the specular region as a function of the incident angle, together with theoretical predictions obtained using the general reflection coefficient, Γ_g.

Figure 5-31: Measured scatter coefficients for the concrete slab with 10 mm stones and smooth stripe together with predictions from the general reflection coefficient
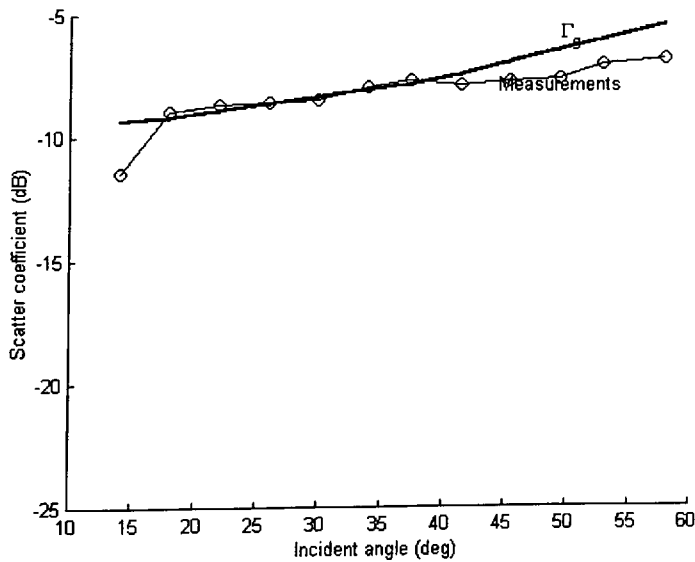
Figure 5-32: Measured scatter coefficients for the concrete slab with 40 mm stones and smooth stripe together with predictions from the general reflection coefficient

The dielectric parameters estimated for the smooth concrete slab (ε_r=4 and σ=0.92) have been used to calculate the reflection coefficient.

It can be observed from Figure 5-31 and Figure 5-32 that the differences between the amplitudes of measured and predicted values give good agreements. This is because, at such angles, the percentage of surface roughness increases, and hence the contribution to the scatter field in the non-specular region increases and become significant.

The scatter coefficients have also been plotted as a function of the observation angle for given angles of incidence. Measured results have been then compared with combined results obtained using plain rough slabs and plain smooth slabs as follows: -

$$\Gamma_{rs}\left(\theta_i,\theta_r\right) = P_{rough}\left(\theta_i,\theta_r\right) \cdot \Gamma_s\left(\theta_i,\theta_r\right) + P_{smooth}\left(\theta_i,\theta_r\right) \cdot \Gamma_g\left(\theta_i,\theta_r\right) \quad (5\text{-}16)$$

Where: P_{rough} is the percentage of rough area within the intersection area of transmit and receive antennas;

P_{smooth} is the percentage of smooth area within the intersection area of transmit and receive antennas;

Γ_s is the scatter coefficient measured from a rough concrete slab;

Γ_g is the reflection coefficient measured from a smooth concrete slab.

Equation (5-16) has also been evaluated theoretically. In this way $\Gamma_s(\theta_i,\theta_r)$ is calculated using the Kirchhoff approximation, with $\Gamma_g(\theta_i,\theta_r)$ being the general reflection coefficient.

Figure 5-33, Figure 5-34, Figure 5-35 and Figure 5-36 show scatter coefficients obtained from measurements, theoretical coefficients and from combination of measurements of smooth and rough surfaces. Measured and theoretical results show good qualitative and quantitative agreements particularly in the specular region. It is clearly seen that the prediction obtained from the combination of Kirchhoff approximation and the general reflection coefficient fail totally to represent the measurements outside the specular region.
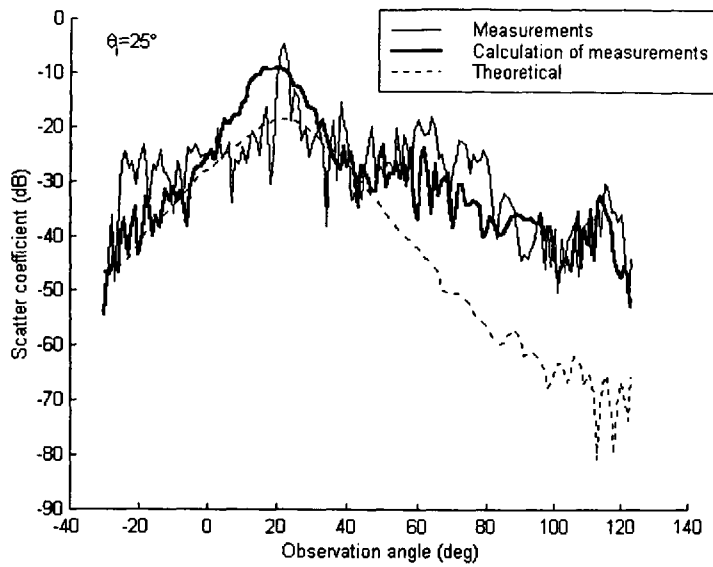
Figure 5-33: VV polarisation measured scatter coefficient of the concrete slab with 10 mm stones and smooth stripe compared with results using equation (5-16)
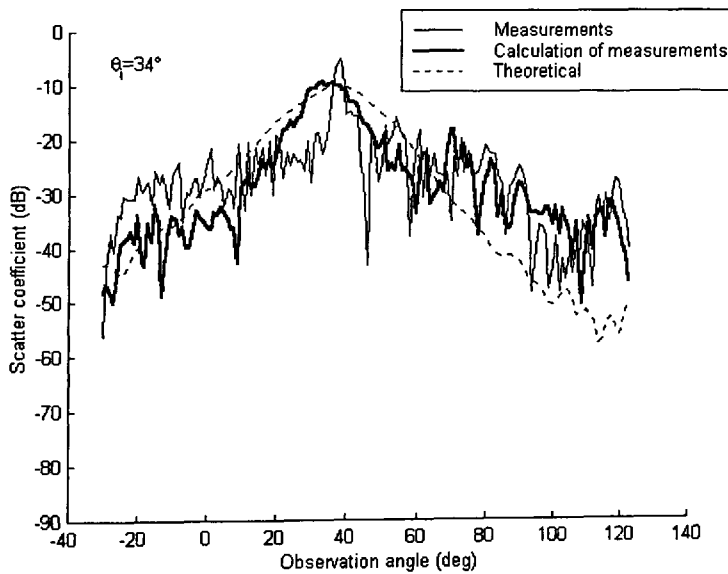
Figure 5-34: VV polarisation measured scatter coefficient of the concrete slab with 10 mm stones and smooth stripe compared with results using equation (5-16)
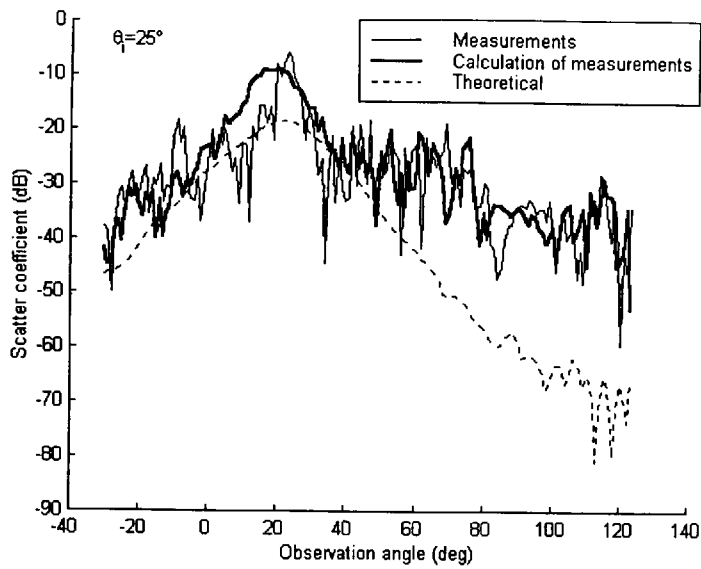
Figure 5-35: VV polarisation measured scatter coefficient of the concrete slab with 40 mm stones and smooth stripe compared with results using equation (5-16)
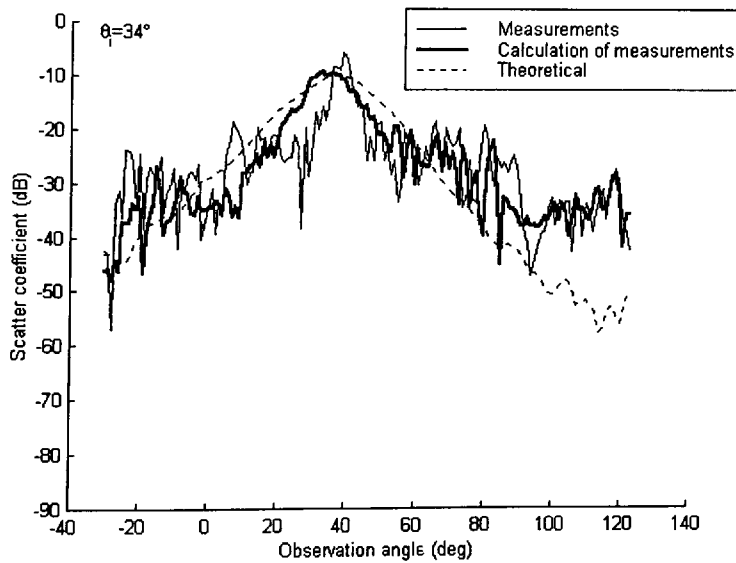
Figure 5-36: VV polarisation measured scatter coefficient of the concrete slab with 40 mm stones and smooth stripe compared with results using equation (5-16)

Measurements and analysis have been made under identical conditions but for horizontal polarisation. Figure 5-37 illustrates the measured scatter coefficient of the concrete slab with 10 mm stones and smooth stripe as a function of incident and observation angles.
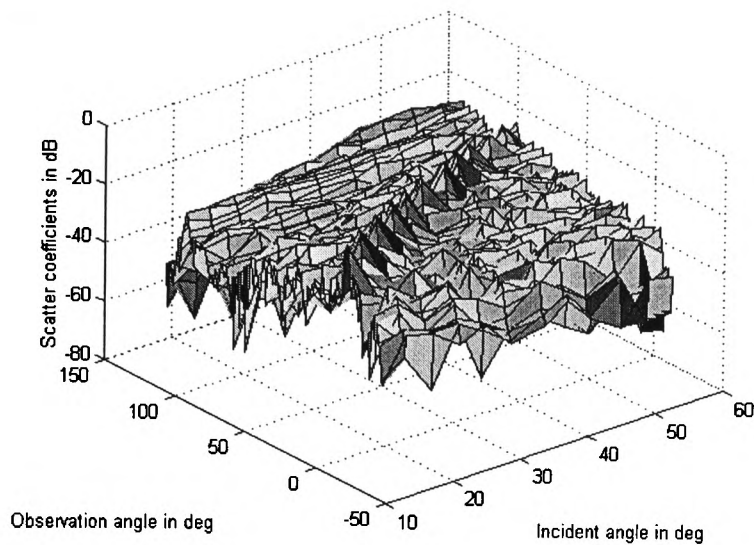
Figure 5-37: HH polarisation measured scatter coefficient as function of observation and incident angles obtained for the concrete slab with 10 mm stones and a 10 cm wide smooth stripe

Figure 5-38 shows the measured maximum values together with predictions obtained from Γ_g where a good agreement is evident. However, differences between measured and computed values would increase for angle of incidence greater than 60°.

Measurements and analysis on the 40 mm concrete slab have demonstrated similar behaviour as those performed on the 10 mm rough concrete slab.

Figure 5-39 and Figure 5-40 show the measured scatter coefficient as a function of observation angle together with theoretical calculations obtained from equation (5-16). The coefficient obtained by a combination of smooth and rough results are also shown. It can be noted that a better agreement with measured values has been reached for the case when experimental results from plain rough and smooth surfaces are combined by the percentage of their illuminated area.
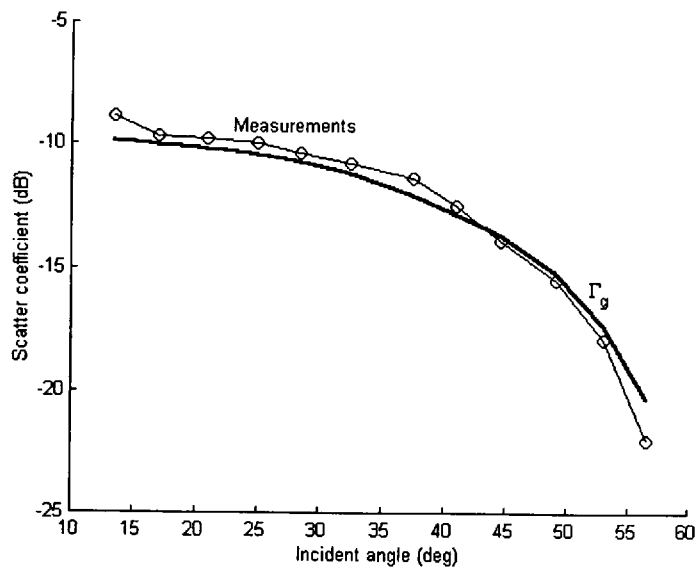
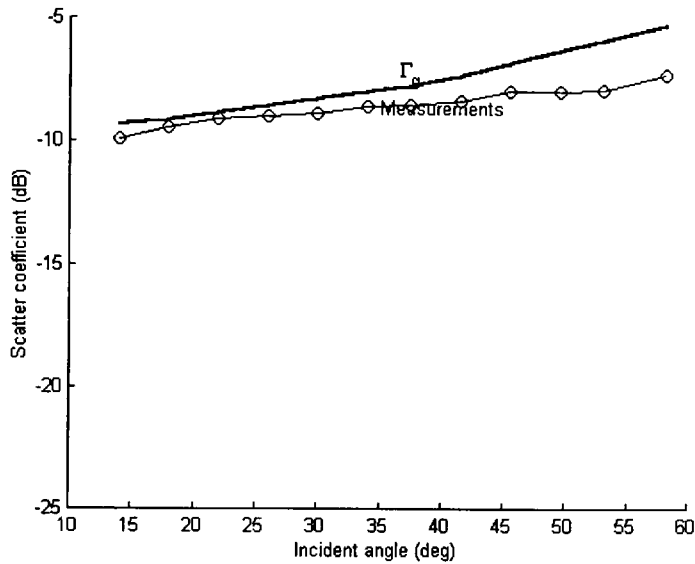Figure 5-38: Measured scatter coefficient for the concrete slab with 10 mm stones and smooth stripe together with predictions from the general reflection coefficient with $\varepsilon_r=4$ and $\sigma=0.92$
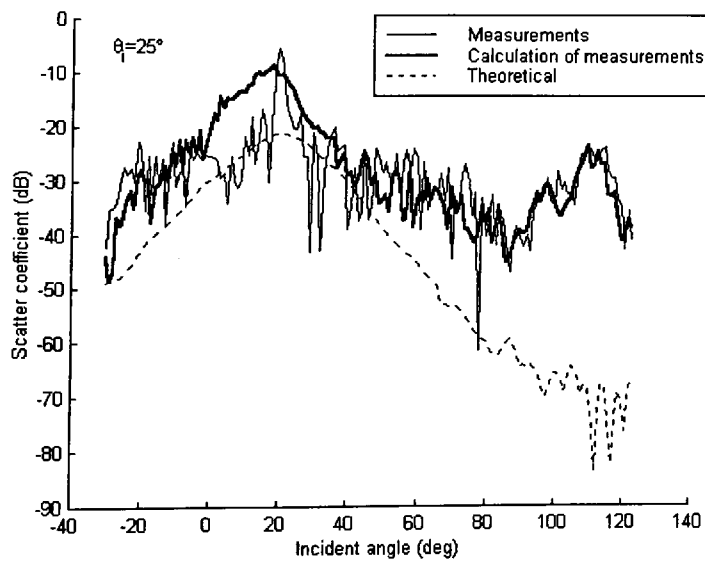

Figure 5-39: HH polarisation measured scatter coefficient of the concrete slab with 10 mm stones and smooth stripe compared with theoretical results and combination of measured values obtained from plain smooth and rough concrete slabs
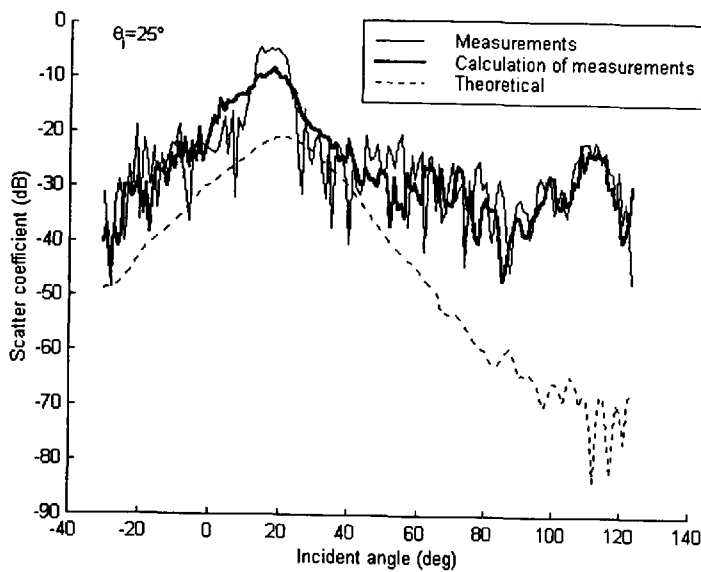
Figure 5-40: HH polarisation measured scatter coefficient of the concrete slab with 40 mm stones and smooth stripe compared with theoretical results and combination of measured values obtained from plain smooth and rough concrete slabs

5.6.2 Cross-Polarisations Reflection Measurements

Effects of depolarisation have also been investigated when the surface consists of rough and smooth areas. The cross-polarisation discrimination has been calculated for various angles of incidence and compared to that obtained in free space. Table 5-8 and Table 5-9 list results obtained for the concrete slabs with 10 and 40 mm stones and smooth stripe respectively using VV and VH polarisations and, Table 5-10 and table 5-11 for the HH and HV polarisations.

Table 5-8: VH cross-polarisation discrimination obtained for the concrete slab with 10 mm stones and smooth stripe

	Percentage of area considered rough			
	63.39% θ_i=18°	65.33% θ_i=25°	67.97% θ_i=33°	73.01% θ_i=45°
Cross-polarisation discrimination for free space measurements	27.17dB	26.08dB	26.07dB	25.76dB
Cross-polarisation discrimination for scattered field measurements	25.60dB	24.21dB	22.74dB	24.79dB
Amount depolarised	1.57dB	1.87dB	3.32dB	0.97dB

Table 5-9: VH cross-polarisation discrimination obtained for the concrete slab with 40 mm stones and smooth stripe

	Percentage of area considered rough			
	63.39% θ_i=18°	65.33% θ_i=25°	67.97% θ_i=33°	73.01% θ_i=45°
Cross-polarisation discrimination for free space measurements	27.48dB	26.16dB	26.49dB	27.50dB
Cross-polarisation discrimination for scattered field measurements	20.31dB	21.63dB	21.60dB	20.79dB
Amount depolarised	7.17dB	4.53dB	4.89dB	6.70dB

VV and VH measurements on the concrete slabs with 10 and 40 mm stones and smooth stripe show that the amount of depolarisation increase on average from 1.9 to 5.8 dB above that of free space respectively. The values are much lower than those obtained for all rough surfaces. It is also evident that the amount of depolarisation is not correlated with the increase in the percentage of the surface roughness that is automatically achieved with the increase of the incident angle.

Results obtained using HH and HV however show a larger gap between the values of the cross-polarisation discrimination measured for the two types of concrete slabs. The cross-polarisation discrimination value obtained here is much larger than that for VV and VH.

Table 5-10: HV cross-polarisation discrimination obtained for the concrete slab with 10 mm stones and smooth stripe

	Percentage of area considered rough			
	63.39% θ_i=18°	65.33% θ_i=25°	67.97% θ_i=33°	73.01% θ_i=45°
Cross-polarisation discrimination for free space measurements	33.27dB	33.61dB	33.30dB	33.19dB
Cross-polarisation discrimination for scattered field measurements	30.97dB	32.66dB	30.64dB	25.45dB
Amount depolarised	2.30dB	0.95dB	2.66dB	7.74dB

Table 5-11: HV cross-polarisation discrimination obtained for the concrete slab with 40 mm stones and smooth stripe

	Percentage of area considered rough			
	63.39% $\theta_i=18°$	65.33% $\theta_i=25°$	67.97% $\theta_i=33°$	73.01% $\theta_i=45°$
Cross-polarisation discrimination for free space measurements	34.65dB	34.95dB	35.04dB	31.61dB
Cross-polarisation discrimination for scattered field measurements	26.39dB	25.78dB	17.63dB	13.66dB
Amount depolarised	8.26dB	9.17dB	17.41dB	17.95dB

It can be noted from those tables that the amount of depolarisation is more significant when the incident wave is horizontally polarised.

5.7 Interim Conclusion

The scatter coefficient from random rough concrete slabs has been measured at 62.4 GHz inside an anechoic chamber, and presented as a function of observation and incident angles. Random rough surfaces have been constructed by impregnating the concrete slabs with either 10, 20 or 40 mm angular stones. The set of parameters that describe each type of roughness has been measured and used in the model. Further measurements were also made on two façades with stones and pebble-dash.

A model based on the Kirchhoff approximation has been developed and used to compare experimental and theoretical results. It has been shown that the scattered field is random, and theoretical results are much lower than measured values. No correlation between the scattered signal level and the parameters describing the concrete slabs is evident.

Cross-polarisation measurements have been made on the concrete slabs and the amount of cross-polarisation discrimination has been quantified. It was not possible to detect any trend between the cross-polarisation discrimination values and σ_h.

Further work has also been presented on surfaces that contain a smooth and rough parts in order to examine the scatter functions and quantify the amount of depolarisation. It was found that the scattered field exhibit a clear specular component,

the level of which varies with the percentage of the surface roughness within the total area formed by the intersection of the transmit and receive antennas. It has also been noted that the amount of depolarisation measured for the slabs with the 40 mm stones is larger than that for the 10 mm stones particularly when HH polarisation is used. The specular level has been successfully predicted by combining experimental results obtained from smooth concrete slabs and rough ones by the percentage value that the surface makes within the total intersection area.

6 Conclusion

6.1 Summary and Conclusion

This thesis reports measurements and modelling of reflection, scatter and transmission mechanisms for various smooth and rough building materials at 62.4 GHz. Reflection, scatter and transmission coefficients are presented as functions of incidence and observation angles. Theoretical modelling based on multiple successive internal reflection for smooth surfaces and the Kirchhoff approximation for random rough surfaces have been developed, and used to interpret experimental results.

Two different measuring set-ups have been devised and developed in order to carry out experiments. The first one consists of an automated bi-static measuring set-up to obtain the reflectivity and the transmissivity of a material at various incident angles inside an anechoic chamber. The second set-up is a controlled mobile radio measuring system for outdoor environments. The transmitter was motor driven along a track bench at a constant speed.

6.1.1 Characterisation of Smooth Building Materials

A bi-static set-up has been developed to measure both reflectivity and transmissivity functions of eight different types of materials using vertical and horizontal polarisations. It has been demonstrated that the reflection and transmission coefficients as a function of the incident angle do not follow those predicted using the well-known Fresnel coefficients. A theoretical model using the Geometrical Optics has been developed in order to account for the thickness of the materials. The dielectric parameters of each building material were then estimated by finding the best fit of the predicted values to both reflectivity and transmissivity measurements. For this purpose two different techniques, the RMS error and Bootstrap, were employed to process the measured and the computed values in order to provide estimates of the dielectric parameters. It has been demonstrated that inaccurate estimates of the dielectric parameters may be obtained if only reflectivity or transmissivity measurement is used.

Variations in the estimates of the dielectric parameters between vertical and horizontal polarisations have been noted. Similar observations were reported by [Correia, Sept. 1994], [Lähteenmäki, August 1996]. It has been demonstrated that due to the flat reflectivity and transmissivity functions of the materials measured using horizontal polarisation, the two techniques loose their sensitivity to detect and extract the best value of the dielectric parameters.

The sensitivity was mainly demonstrated by the values of the dielectric parameters obtained for the glass, $\varepsilon_r=8.9$ $\sigma=0.44$ when compared with those reported $\varepsilon_r=5.29$ $\sigma=0.85$ [Correia, Sept. 1994], $\varepsilon_r=7.51$ $\sigma=0.62$ [Sato, Dec. 1997] and $\varepsilon_r=6.81$ $\sigma=0.57$ [Manabe, July 1992]. The values of the estimated parameters obtained using vertical polarisation have been compared with those reported in literature and found to be in a reasonably good agreement.

The behaviour of millimetre wave wireless indoor mobile radio channel has been characterised in the literature using ray-tracing techniques. Such methods depend on the reflection and transmission characteristics of the internal partitions of the indoor environment, and mainly use the well-known Fresnel coefficients. The change in the indoor channel characteristics (such as the propagation distance exponent and line-of-sight to the total reflection power ratio) when reflections are computed using the multiple successive reflection model developed here has been evaluated and presented in this thesis. It has been shown that the total reflected power is more significant when the thickness of the materials is taken into account. It has been shown that the propagation distance exponent in a long narrow corridor with 9 mm thick plasterboard side-walls is 1.29 compared to 1.32 when Fresnel coefficients are used. The line-of-sight to the total reflection power ratio (K factor in the Rice distribution) is found on average to decrease from 10.09 to 8.7 dB.

6.1.2   Characterisation of Rough Surfaces

The scatter coefficient as a function of incident and observation angles has been measured for seven different types of surfaces using co and cross-polarisations. A campaign of measurements has been carried out on rough surfaces inside the anechoic chamber, and on outdoor building façades. The surfaces investigated were two building façades and five concrete slabs manufactured in the School of the Built Environment. Random rough surfaces of the concrete slabs were made by impregnating the concrete

slabs (90 x70 cm^2) with 10, 20 and 40 mm angular stones. A total of 15 slabs were made, five for each type of roughness.

A photographic technique measuring the surface irregularities of the rough surface has been used to determine the parameters that describe the surface. The parameters that are used in this thesis to describe the surface are the standard deviation of random rough surface distribution and the correlation distance.

A theoretical model based on the Kirchhoff approximation has been developed and used to assist in the interpretation of experimental results. Theoretical predictions obtained from this model were found to under-estimate the level of scattering for vertical and horizontal polarisations. This was explained by the fact that the values of the correlation distance were found to be not too much larger than the wavelength. Even when the correlation distance is about three wavelengths (as for the outdoor façade made of big stones) theoretical solutions were still below the measurements. The amount of depolarisation due to surface irregularities has also been investigated for different angles of incidence. It was not possible to correlate the amount of depolarisation with the parameters characterising the surface. Results presented here have shown that cross-polarisation levels from (VV-VH) are on average 11.5, 13.7 and 13.7 dB for the concrete slabs with 10, 20 and 40 mm stones respectively. Whereas depolarisation from HH to HV those levels become 13.8, 14.6 and 12.7 dB.

The dependence of the scatter level on the surface roughness has also been investigated using vertical and horizontal polarisations. The scatter coefficients vary in amplitude for the 10, 20 and 40 mm concrete slabs in a random manner, and no correlation could be found with the parameters characterising the surface. This may be explained by the fact that these parameters do not uniquely describe the roughness of the concrete slabs and that roughness nature of the scattered field.

6.1.2.1   Characterisation of Semi-Specular Behaviour

Two rough surfaces have been made to have, at their centre, a 10 cm wide smooth concrete stripe. This was made so that measurements on a surface that contains smooth and rough parts are possible. The scatter coefficients presented as functions of the observation angles exhibit a specular component, the level of which varies with the angle of incidence. The variation in its level is due to the changes in the percentage of rough area to the total area of the intersection of both antennas with the angle of incidence. The level of the specular component has been compared with values obtained from a simplified formulation (2-3) proposed by [Beckmann, 1987] for a Gaussian

distributed surface roughness with standard deviation σ_h. The predicted results are found to under-estimate the scatter level significantly and hence such formulation may not be accurate to use in deterministic modelling of the channel. These results are in line with those obtained in an outdoor mobile radio environment at 62 GHz.

Measurements have also been compared to values obtained by combining the measured/computed reflection coefficient for the smooth slabs, and that measured/obtained from the Kirchhoff approximation for the rough area, by the percentage of their surface area relative to the total area. Results obtained using this approach have shown good qualitative agreements with the measurements. It has been found that combining both theoretical smooth and rough scatter coefficients yields to lower level than the measurements.

Depolarisation into the horizontal direction in the specular region was found to increase with the size of the stone on average from 1.9 to 5.8 dB above the free space for the slabs with the 10 and 40 mm stones respectively. Whereas depolarisation from horizontal into vertical was found to be 4.28 and 15.20 dB.

6.2   Further work

- To estimate the complex permittivity using a vector network analyser (VNA)
- To model the random rough surfaces with different techniques such as radiosity, integral equations method (IEM), perturbation method, etc.
- To include the surface roughness in a ray-tracing algorithm

6.3   Contribution to Published Literature

During the course of the research, the author has made the following contributions to published material: -

> *1999   Conference* at York.
>
> *Name*: CAP (Conference of Antennas and Propagation), on Antennas and Propagation.
>
> *Title*: "**Comparison of Reflection Mechanisms from Smooth and Rough Surfaces at 62 GHz**"
>
> *Authors*: A. Hammoudeh, JP Pugliese, M. Sanchez and E. Grindrod.

> *1997:* **Conference** at Heriot-Watt University, Edinburg.

Name: 10th International conference, ICAP (International Conference of Antennas and Propagation), on Antennas and Propagation.

Title: **"Estimation of dielectric parameters from reflection and transmission coefficients of building materials at 62 GHz"**

Authors: JP Pugliese, A. Hammoudeh and M. Al-Nuaimi.

> *1996:* **Colloquium** at Savoy Place, London.

Name: Colloquium IEE (Institute of Electrical Engineering) on Radio communications at microwave and millimetre wave frequencies (16th December 1996).

Title: **"Reflection and transmission characteristics of building materials at 62 GHz"**

Authors: JP Pugliese, A. Hammoudeh and M. Al-Nuaimi.

A   Appendix 1
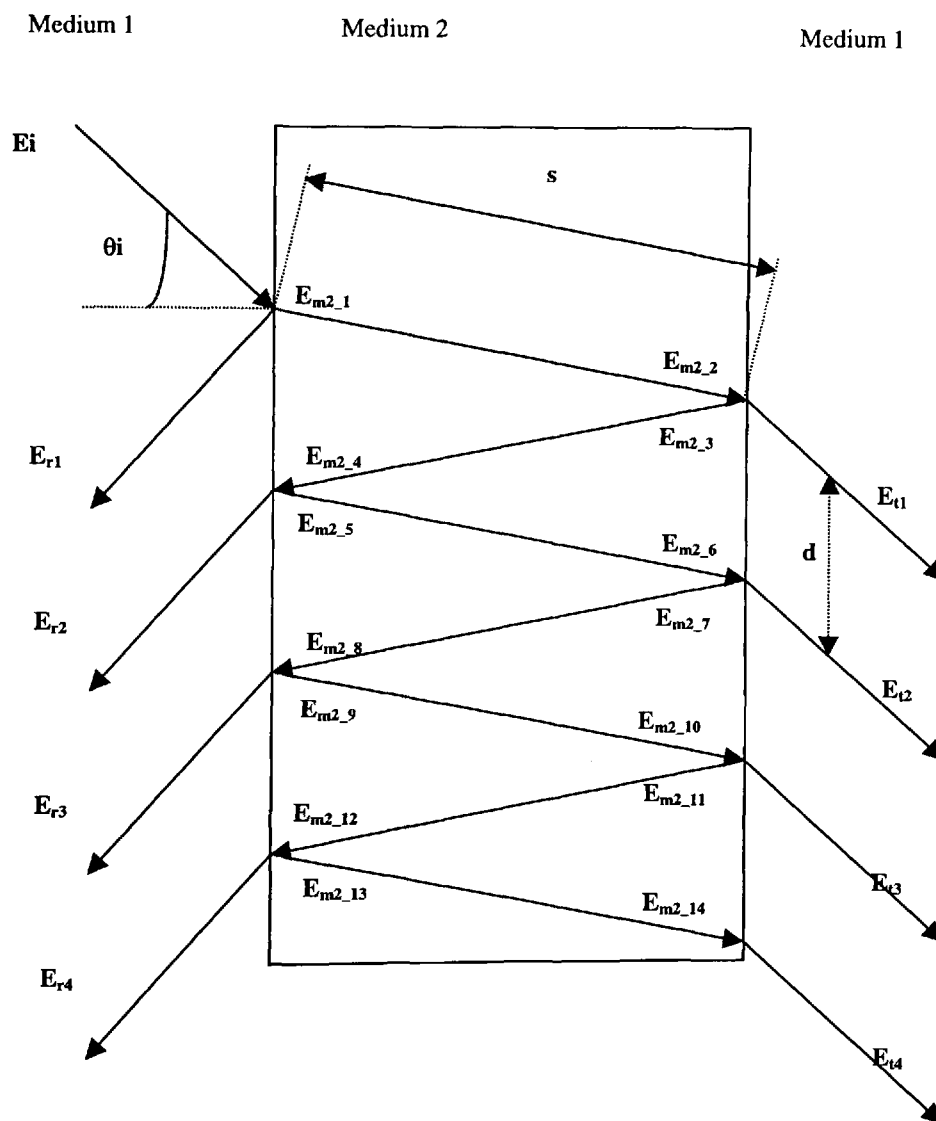
Figure A-1: Successive reflection inside a material represented by GO

All values have already been referenced to the incident field, Ei. Therefore

$E_{r1} = \rho_{21}$

The subscripts express the direction of the ray from one medium to another, where 1 defines the medium air and 2 the material.

$E_{m2\_1} = \tau_{12}$

$E_{m2\_2} = \tau_{12} \cdot e^{(A')}$ $\qquad E_{t1} = \tau_{12} \cdot e^{(A')} \cdot \tau_{21}$

$E_{m2\_3} = \tau_{12} \cdot \rho_{12} \cdot e^{(A')}$

$E_{m2\_4} = \tau_{12} \cdot \rho_{12} \cdot e^{(2A')}$ $\qquad E_{r2} = \tau_{21} \cdot \tau_{12} \cdot \rho_{12} \cdot e^{(2A')} \cdot e^{(j \cdot d \cdot k0 \cdot \sin\theta i)}$

$E_{m2\_5} = \tau_{12} \cdot (\rho_{12})^2 \cdot e^{(2A')}$

$E_{m2\_6} = \tau_{12} \cdot (\rho_{12})^2 \cdot e^{(3A')}$ $\qquad E_{t2} = \tau_{12} \cdot (\rho_{12})^2 \cdot e^{(3A')} \cdot \tau_{21} \cdot e^{(j \cdot d \cdot k0 \cdot \sin\theta i)}$

$E_{m2\_7} = \tau_{12} \cdot (\rho_{12})^3 \cdot e^{(3A')}$

$E_{m2\_8} = \tau_{12} \cdot (\rho_{12})^3 \cdot e^{(4A')}$ $\qquad E_{r3} = \tau_{12} \cdot (\rho_{12})^3 \cdot e^{(4A')} \cdot \tau_{21} \cdot e^{(j \cdot 2 \cdot d \cdot k0 \cdot \sin\theta i)}$

$E_{m2\_9} = \tau_{12} \cdot (\rho_{12})^4 \cdot e^{(4A')}$

$E_{m2\_10} = \tau_{12} \cdot (\rho_{12})^4 \cdot e^{(5A')}$ $\qquad E_{t3} = \tau_{12} \cdot (\rho_{12})^4 \cdot e^{(5A')} \cdot \tau_{21} \cdot e^{(j \cdot 2 \cdot d \cdot k0 \cdot \sin\theta i)}$

$E_{m2\_11} = \tau_{12} \cdot (\rho_{12})^5 \cdot e^{(5A')}$

$E_{m2\_12} = \tau_{12} \cdot (\rho_{12})^5 \cdot e^{(6A')}$ $\qquad E_{r4} = \tau_{12} \cdot (\rho_{12})^5 \cdot e^{(6A')} \cdot \tau_{21} \cdot e^{(j \cdot 3 \cdot d \cdot k0 \cdot \sin\theta i)}$

$E_{m2\_13} = \tau_{12} \cdot (\rho_{12})^6 \cdot e^{(6A')}$

$E_{m2\_14} = \tau_{12} \cdot (\rho_{12})^6 \cdot e^{(7A')}$ $\qquad E_{t4} = \tau_{12} \cdot (\rho_{12})^6 \cdot e^{(7A')} \cdot \tau_{21} \cdot e^{(j \cdot 3 \cdot d \cdot k0 \cdot \sin\theta i)}$

With: $A' = -\alpha \cdot s - j \cdot k \cdot s$

Where: α is tha attenuation inside the material (Np/m);

k is the propagation constant inside the material (rad/m);

k_0 is the propagation in free space (rad/m).

The expression $d \cdot k_0 \cdot \sin(\theta_i)$ is the phase term separating each ray when projected to infinity.

The summation of each reflected and refracted ray from the material provided the overall reflectivity and transmissivity of the material respectively.

The reflected field is given by: -

$E_r = E_{r1} + E_{r2} + E_{r3} + E_{r4} + \ldots$

The refracted field is given by: -

$E_t = E_{t1} + E_{t2} + E_{t3} + E_{t4} + \ldots$

The reflected and refracted fields progress geometrically to a certain limit. The ratio and the convergence of the geometrical series for both reflected and refracted fields are calculated underneath

A.1 Geometrical series

Reflection

The ratio of the geometrical serie is given below: -

$$q_r = \frac{E_{r3}}{E_{r2}} = \frac{\tau_{12} \cdot \rho_{12}^3 \cdot e^{4 \cdot (\alpha \cdot s - j \cdot k \cdot s)} \cdot \tau_{21} \cdot e^{j \cdot 2 \cdot d \cdot k_0 \cdot \sin\theta_i}}{\tau_{12} \cdot \rho_{12} \cdot e^{2 \cdot (\alpha \cdot s - j \cdot k \cdot s)} \cdot \tau_{21} \cdot e^{j \cdot d \cdot k_0 \cdot \sin\theta_i}}$$

$$q_r = \rho_{12}^2 \cdot e^{2 \cdot (\alpha \cdot s - j \cdot k \cdot s)} \cdot e^{j \cdot d \cdot k_0 \cdot \sin\theta_i}$$

From this the convergence of the serie can be calculated giving the expression below: -

$$E_r' = \frac{E_{r2}}{1 - q_r} \qquad \text{with} \qquad E_r = E_{r1} + E_r'$$

$$E_r' = \frac{\tau_{12} \cdot \rho_{12} \cdot e^{2 \cdot (\alpha \cdot s - j \cdot k \cdot s)} \cdot \tau_{21} \cdot e^{j \cdot d \cdot k_0 \cdot \sin\theta_i}}{1 - \rho_{12}^2 \cdot e^{2 \cdot (\alpha \cdot s - j \cdot k \cdot s)} \cdot e^{j \cdot d \cdot k_0 \cdot \sin\theta_i}}$$

Transmission

The ratio of the geometrical serie is given below: -

$$q_t = \frac{E_{t3}}{E_{t2}} = \frac{\tau_{12} \cdot \rho_{12}^4 \cdot e^{5 \cdot (\alpha \cdot s - j \cdot k \cdot s)} \cdot \tau_{21} \cdot e^{j \cdot 2 \cdot d \cdot k_0 \cdot \sin\theta_i}}{\tau_{12} \cdot \rho_{12}^2 \cdot e^{3 \cdot (\alpha \cdot s - j \cdot k \cdot s)} \cdot \tau_{21} \cdot e^{j \cdot d \cdot k_0 \cdot \sin\theta_i}}$$

$$q_t = \rho_{12}^2 \cdot e^{2 \cdot (\alpha \cdot s - j \cdot k \cdot s)} \cdot e^{j \cdot d \cdot k_0 \cdot \sin\theta_i}$$

From this the convergence of the serie can be calculated giving the expression below: -

$$E_t' = \frac{E_{t1}}{1 - q_t} \qquad \text{with} \qquad E_t = E_t'$$

$$E_t' = \frac{\tau_{12} \cdot e^{(\alpha \cdot s - j \cdot k \cdot s)} \cdot \tau_{21}}{1 - \rho_{12}^2 \cdot e^{3 \cdot (\alpha \cdot s - j \cdot k \cdot s)} \cdot e^{j \cdot d \cdot k_0 \cdot \sin\theta_i}}$$

Well, it can be easily demonstrated that $\rho_{21} = -\rho_{12}$

So $\tau_{21} = 1 + \rho_{21}$

$\tau_{12} = 1 + \rho_{12} = 1 - \rho_{21}$

This yields: -

$$\Gamma_g = E_r = \rho_{21} - \frac{(1 - \rho_{21}^2) \cdot \rho_{21} \cdot e^{2 \cdot (\alpha \cdot s - j \cdot k \cdot s)} \cdot e^{j \cdot d \cdot k_0 \cdot \sin\theta_i}}{1 - \rho_{21}^2 \cdot e^{2 \cdot (\alpha \cdot s - j \cdot k \cdot s)} \cdot e^{j \cdot d \cdot k_0 \cdot \sin\theta_i}}$$

$$T_g = E_t = \frac{(1 - \rho_{21}^2) \cdot e^{(\alpha \cdot s - j \cdot k \cdot s)}}{1 - \rho_{21}^2 \cdot e^{2 \cdot (\alpha \cdot s - j \cdot k \cdot s)} \cdot e^{j \cdot d \cdot k_0 \cdot \sin\theta_i}}$$

References

Alison, J.M. and Sheppard, R.J., "A precision wave-guide system for the measurement of complex permittivity of lossy liquids and solid tissues in the frequency-range 29-GHz to 90-GHz-III. The liquid-system for 57 to 82-GHz: An investigation into water and formamide", Meas. Sci. and technol., Vol. 2, No. 10, pp. 975-979, 1991.

Allen, G. and Hammoudeh, A., "60GHz propagation measurements within a building", 20th European Microwave Conf. EMC20, September 1990.

Amitay, N., "Modeling and computer simulation of wave propagation in linear line-of-sight microcells", IEEE Trans. on Veh. Tech., Vol. 41, pp. 337-342, November 1992.

Andersen, J.B., Rappaport, T.S. and Yoshida, S., "Propagation measurements and models for wireless communications channels", IEEE Communications Magazine, Vol. 33, pp. 42-49, January 1995.

Ashdown, I., "Radiosity: a programmer's perspective", John Wiley & Sons, 1994.

Bahar, E., "Full wave analysis for rough surface. Diffuse, incoherent radar sections with height-slope correlations included", IEEE Trans. on Antennas and Propagation, Vol. 39, No. 9, September 1991.

Bailey, A.L., "A ray-tracing model for indoor propagation characteristics at millimetre frequencies", PhD. Thesis, Bath University, U.K., 1994.

Balanis, C., "Advanced engineering electromagnetics", John Wiley&Sons, 1989.

Bass, F.G. and Fuks, I.M., "Wave scattering from statistically rough surfaces", Pergamon Press Ltd., 1979.

Beckmann, P. and Spizzichino, A., "The scattering of electromagnetic waves from rough surfaces", Artech House Inc., 1987.

Bello, P.A., "Characterization of randomly time-variant linear channels", IEEE Trans. on Comm. Systems, pp. 360-393, December 1963.

Birch, J.R., Simonis, G.J., Asfar, M.N.m Clarke, R.N., Dutta, J.M., Frost, H.M, Gerbaux, X., "An intercomparison of measurement technologies for the determination of the dielectric properties of solids at near millimeter wavelengths", IEEE Trans. Microwave Theory Tech., Vol. 42, No. 6, pp. 956-965, June 1994.

Blackham, D., "Free space characterization of materials", in Proc. 1993 Antenna Meas. Tech. Assoc. Mtg. And Symp., October 1993.

Burnside, W. and Burgener, K.W., "High frequency scattering by a thin lossless dielectric slab", IEEE Trans. On Antennas and Propa., Vol. AP-31, No. 1, pp. 104-110, January 1993.

Cole, R., Thomas, H. and Siqueria, G., "Two frequency coherence measurements on a 55GHz mobile radio link", Journal IERE, Vol. 58, No. 6, pp. 140-144, 1988.

Collaro, A., Franceschetti, G., Migliaccio, M. and Riccio, D., "Gaussian rough surfaces and Kirchhoff approximation", IEEE Trans. on Antennas and Propagation, Vol. 47, No. 2, February 1999.

Correia, L. and Francês, P., "Transmission and isolation of signals in buildings at 60 GHz", Personal Indoor and Mobile Radio Communications (PIMRC'95), Toronto (Canada), 27-29 September 1995.

Correia, L. and Francês, P., "Estimation of materials characteristics from power measurements at 60 GHz", PIMRC'94, Personal Indoor and Mobile Radio Communications, The Hague, Netherlands, Sept. 19-23 1994.

Correia, L. and Francês, P., "First results on the estimation of materials characteristics from measurements t 60 GHz", COST 231 TD(94), Lisbon (Portugal), 18-21 January 1994.

COST 231, "Digital mobile radio: COST 231 view on the evolution towards 3rd generation systems".

Daniels, D.J., "Surface-penetrating radar", Electronics and Comm. Eng. Journal, pp. 165-182, August 1996.

Dersch, U., Troger, J. and Zollinger, E., "Multiple reflections of radio waves in a corridor", IEEE Trans. on Antennas and Propagation, Vol. 42, pp. 1571-1574, September 1994.

Ding, M.S., "Modelling and measurement of the scatter of microwaves by building", Ph.D. Thesis, University of Glamorgan, Wales (U.K.), July 1994.

Duffy, T., "Eliminating multipath fading in digital radios", Microwaves and RF, Vol. 27, Part 6, pp. 127-134, 1988.

Efron, B. and Tibshirani, R., "An introduction to the bootstrap", Chapman&Hall, 1993.

Efron,B., "The Jacknife, the Bootstrap, and other resampling plans", (CBMS-NSF Reg. Conf. Series Appl. Math.), Philadelphia (USA), PA: Soc. Ind. App. Math., Vol. 38, 1982.

Evans, D.L., "Applications of imaging radar data in earth science investigations", Electronics and Communication Engineering Journal, Vol. 11, No. 5, October 1999.

Ghodaonkar, D.K., Varadan V.V. and Varadan, V.K., "A free-space method for measurement of dielectric constants and loss tangents at microwave frequencies", IEEE Trans. Instrum. Meas., Vol. 37, No. 3, pp. 789-793, June 1989.

Ghodaonkar, D.K., Varadan V.V. and Varadan, V.K., "Free-space measurement of complex permittivity and complex permeability of magnetic materials at microwave frequencies", IEEE Trans. Instrum. Meas., Vol. 39, No. 2, pp. 387-394, April 1990.

Hammoudeh, A., Sánchez, M.G. and Grindrod, E., "Experimental analysis of propagation at 62GHz in sub-urban mobile radio microcells", IEEE Transactions on Vehicular Technology, Vol. 48, No. 2, pp 576-588, March 1999.

Hammoudeh, A. and Haslett, C., "Characterisation and modelling of obstructed line-of-sight millimetre wave mobile radio signals", ICAP'95, 9th International Conference on Antennas and Propagation, Eindhoven, The Netherlands, Vol. 2, pp. 283-287, April 1995.

Hammoudeh, A. and Allen, G., "Millimetric wavelengths radiowave propagation for line-of-sight indoor microcellular mobile communications", IEEE Transactions on Vehicular Technology, Vol. 44, No. 3, August 1995.

Hata, M., "Empirical formula for propagation loss in land mobile radio services", IEEE Trans. on Vehicular Technology, Vol. VT 29, No. 3, pp. 317-325, August 1980.

Heavens, O., "Optical properties of thin solid films", Butterworths Scientific Publications ltd., 1955.

Howard, S.J. and Pahlavan, K., "Doppler spread measurements of indoor radio channel", Electronics Letters, Vol. 26, pp. 107-108, January 1990.

Hviid, J.T., Bach Anderson, J., Toftgärd, J. and Bøjer, J., "Terrain based propagation model – an integral approach", IEEE Trans. on Antennas and Propagation, Vol. 43, No. 1, pp. 41-46, January 1995.

Knott, E., Shaeffer, J. and Tuley, M., "Radar cross section", 2nd ed. Norwood, MA: Artech House, 1993.

Kermoal, J.P., "Coherence bandwidth characterisation for indoor mobile radio microcells at microwave and millimetre wave frequencies", M.Phil. Thesis, University of Glamorgan, Wales (U.K.), April 1998.

Kloch, C., "Influence of surface irregularities on propagation prediction models used in mobile communications", Ph.D. Thesis, Aalborg University, Denmark, March 1998.

Kloch, C. and Andersen, J.B., "Radiosity – An approach to determine the effect of rough scattering in mobile scenarios", IEEE Antennas and Propagation Society International Symposium, Montreal (Canada), 13-18th July 1997.

Kraus, J.D., "Electromagnetics", McGraw-Hill International Editions, 1991.

Lähteenmäki, J. and Karttaavi, T., "Measurement of dielectric parameters of wall materials at 60 GHz band", Electronic Letters, Vol. 32, No. 16, 1st August 1996.

Landron, O., Feuerstein, M.J. and Rappaport, T.S., "A comparison of theoretical and empirical reflection coefficients for typical exterior wall surfaces in a mobile radio environment", IEEE Transaction on Antennas and Propagation, Vol. 44, No. 3, pp 341-251, March 1996.

Langen, B., Lober, G. and Herzig, W., "Reflection and transmission behaviour of building materials at 60 GHz", PIMRC'94, Personal Indoor and Mobile Radio Communications, The Hague, Netherlands, Sept. 19-23 1994.

Linnartz, JP, "Narrow land-mobile radio networks, Artech House, 1993."

References

Manabe, T., Sato, K. and Ihara, T., "Measurement of complex refractive index of soda-lime glass at 60 GHz by vector-network-analyser-based scatterometer", Electronic Letters, Vol. 28, No. 14, pp. 1354-1355, 2nd July 1992.

McKnown, J.W. and Hamilton, J.R.L., "Ray tracing as a design tool for radio networks", IEEE Network Mag., Vol. 5, pp. 27-30, November 1991.

Medwin, H. and Clay, C.S., "Fundamentals of acoustical oceanography", Academic Press, 1997.

Molkdar, D., "Review on radio propagation into and within buildings", IEE Proceeding, Vol. 138, pp. 61-73, February 1991.

Ogilvy, J.A., "Theory of wave scattering from random surfaces", Adam Hilger, 1991.

Parsons, J.D., "The mobile radio propagation channel", Pentech Press, Publishers – London, 1992.

Pope, K.O., Rey-Benayas, J.M., Filoso, S. and Wang, Y., "Delineation of inundated area and vegetation along the Amazon floodplain with the SIR-C synthetic aperture radar", Rem. Sens. Environ., Vol. 48, pp. 205-219, 1994.

Rappaport, T.S., Seidel, S.Y. and Singh, R., "900 MHz multipath propagation measurements for US digital cellular radio telephone", IEEE Trans. Vehicular Technol., Vol. VT-39, Part 2, pp. 132-139, May 1990.

Rice, S.O., "Reflection of electromagnetic waves from slightly rough surfaces", Commun. Pure Appl. Math., Vol. 4, pp 351-378, 1951.

Richards, M.G. and Sheppard, R.J., "A precision wave-guide system for measurement of complex permittivity of lossy liquids and solid tissues in the frequency-range 29-GHz to 90-GHz-II. The liquid-system for 90-GHz, high-frequency cell design", Meas. Sci. and Technol., Vol.2, No. 7, pp. 663-667, 1991.

Richter, J., "Resolution of signal components of a resultant electromagnetic wave received in a multipath field of microwave frequencies", Ph.D. Thesis, University of Glamorgan, Wales (U.K.), May 1998.

Sánchez, M.G., de Haro, L., Pino, A.G. and Calvo, M., "Exhaustive ray tracing algorithm for microcellular propagation prediction models", Electronics Letters, Vol. 32, No. 7, pp. 624-625, 28th March 1996.

Sato K., Manabe T., Ihara T., Saito H., Ito S., Tanaka T., Sugai K., Ohmi N., Murakami Y., Shibayama M., Konishi Y. and Kimura T., "Measurements of reflection and transmission characteristics of interior structures of office building in the 60-GHz band", IEEE Transactions on Antennas and Propagation, Vol. 45, No. 12, December 1997.

Sato, K., Manabe, T., Polivka, J., Ihara, T., Kasashima, Y. and Yamaki, K., "Measurement of complex refractive index of concrete at 57.5GHz", IEEE Trans. On Antennas and Prop., Vol. 44, No. 1, pp. 35-40, January 1996.

Seidel, S.Y. and Rappaport, T.S., "Site specific propagation prediction for wireless in building personal communication system design", IEEE Trans. Veh. Technol., Vol. VT-43, No. 4, pp. 879-891, 1994.

Shimabukuro, F., Lazar S., Chernick M. and Dyson H., "A quasi-optical method for measuring the complex permittivity of materials", IEEE Transactions on Microwave Theory and Techniques, Vol. MTT-32, No. 7, July 1984.

Smith, F.C., Chambers, B. and Bennett, J.C., "Calibration techniques for free space reflection coefficient measurements", IEE Proceediings-A, Vol. 139, No. 5, pp. 247-253, September 1992.

Steel, M.C., Sheppard, R.J. and Collins, R., "Precision waveguide cells for the measurement of complex permittivity of lossy liquids and biological tissue at 35GHz", J. Phys. E: Sci. Instrum., Vol. 20, pp. 872-877, 1987.

Steele, R. and Parbhu, V., "Mobile radio cellular structures for high user density and large data rates", Proc. IEE, pt. F, Vol. 132, pp. 396-404, 1985.

Stephens, R.B.L., "A study and modelling of the propagation effects of vegetation on radio waves at centimetre-wavelength frequencies", Ph.D. Thesis, University of Glamorgan, Wales (U.K.), 1998.

Suzuki, H. and Mohan, A.S., "Ray tube tracing method for predicting indoor channel characteristics map", Electronics Letters, Vol. 33, pp. 1495-1496, August 1997.

Tan, S.Y. and Tan, H.S., "Improved three-dimensional ray tracing technique for microcellular propagation models", Electronics Letters, Vol. 31, pp. 1503-1505, August 1995.

Tan, S.Y. and Tan, H.S., "Basic optimisation methods", Edward Arnold Published, London, 1994.

Tarek, A. and McGeehan, J., "Propagation and bit error rate measurements within buildings in the millimetre wave band about 60GHz", IEEE Int. Conf. Communication, ICC88, pp. 318-321, 1988.

Turin, G.L., "Communication through noisy, random-multipath channels, IRE Convention Record, Part 4, pp. 154-166, 1956."

Ulaby, F.T., Haddock, T.F. and Whitt, M.W., "A millimeterwave network analyser based scatterometer", IEEE Trans. on Geo. and Remote Sensing, Vol. 26, No. 1, January 1988.

Varadan, V.V., Hollinger, R.D. and Ghodgaonkar, D.K., "Free-space, broadband measurements of high-temperature, complex dielectric properties at microwave frequencies", IEEE Trans. Instrum. Meas., Vol. 40, No. 5, pp. 842-846, October 1991.

Wu, W. and Smith, C.E., "Dielectric measurements using the HP 8510 probe", in Proc. IEEE Reg. III Southeast Conf. '92, pp.83-86, April 12-15 1992.